Università degli Studi di Napoli "Federico II"

Facoltà di Ingegneria
Dipartimento di Progettazione Aeronautica (DPA)

Doctoral Thesis in Aerospace Engineering

AIRCRAFT ENDURANCE IMPROVEMENT THROUGH TURBULENT SEPARATION CONTROL

Ernani Fulvio Bellobuono

Tutor   Coordinator
Prof. Domenico P. Coiro   Prof. Antonio Moccia

December 2006

Acknowledgments

My sincere thanks go to all the persons who have contributed to this thesis with their support and advice.

First of all, I am especially grateful to Prof. Domenico Coiro, my tutor, who has constantly supported my work and has guided me with his competence and enthusiasm.

I would also like to thank all the personnel of the ADAG group, in particular Ing. Ferdinando Scherillo, Ing. Umberto Maisto, Ing. Fabrizio Nicolosi and Ing. Agostino De Marco for the fundamental and stimulating collaboration throughout these years.

Thanks also to the DPA laboratory team, represented by Mr. Crispino, for their important help with my "lab" work.

Finally particular thanks are to CIRA research center, that has given me the opportunity to work on one of their research projects.

Abstract

Boundary layer unsteady blowing is one of the most advanced solution to reduce aircraft parasite drag and flow separation at high angles of attack. In this way high lift can be achieved along with low-drag and since endurance is one of the most important performance parameter for some types of aircraft, such as an UAV, it is clear that the ratio $CL^{3/2}/CD$ has to be maximized.

Main goal of the present investigation is the exploration of the possible ways for obtaining efficient turbulent boundary layer control, keeping in mind, at the same time, the practical problems connected to the installation of the device in a real wing. Furthermore a global balance of needed power is necessary to prove that the net power balance is in favour of the case in which the control is applied. The work has been mainly addressed to the verification of active control through steady suction and pulsed blowing as an effective tool to delay boundary layer separation. In the first part preliminary theoretical consideration and numerical simulation are presented for steady suction as well as for steady and unsteady blowing. In the second part of the work, experimental investigations on a model wing opportunely instrumented and set in the wind tunnel are presented followed by the discussion of results.

Contents

List of Symbols

Latin

A	tube section area [m^2]
a_s	slot cut area [m^2]
B	wall law intercept
c	airfoil chord [m]
$\underline{c}$	speed of sound [m\s]
C_D	dissipation coefficient
C_f	skin friction coefficient
Cl,Cd	2d lift and drag coefficient
CL,CD	3D lift and drag coefficient
Cp	pressure coefficient
Cq	suction coefficient (V_0\V_∞)
$C_{t,c}$	acoustic compliance (with subscript t for tube and c for chamber) [m^{3}s^2\kg]
C_μ	total momentum coefficient of pulsed blowing jet
$<c_\mu>$	mean part of momentum coefficient of pulsed blowing jet
c_{μ_rms}	root mean square of momentum coefficient
c_μ'	fluctuating part of momentum coefficient of pulsed blowing jet
d	diameter of connection tube in the pulsed blowing system
End	endurance (lift$^{3\backslash 2}$\drag)
E	efficiency (lift/drag)
F^+	reduced frequency
f	frequency of pulsed blowing jet [Hz], ratio of transpiration velocity and the boundary layer-edge velocity
f_{sep}	characteristic frequency of the separation region [Hz]
f_{SL}	shear layer frequency [Hz]
f^0_{SL}, f^r_{SL}	natural and forced shear layer frequency [Hz]
f_w	wake function
f_{wake}	characteristic frequency of the wake shedding [Hz]
G	inner variable integral for boundary layer calculation
G_t	tube conductance

H	inner variable integral for boundary layer calculation
h	slot height [m]
H_{12}	shape factor: ratio of displacement δ^* to momentum thickness θ
H_{32}	shape factor: ratio of energy thickness θ^* and momentum thickness θ
J_0	Bessel function of zero order
j	imaginary part
ln	actual thickness of the plate [m]
$L_{t,c}$	acoustic inertance (with subscript t for tube and c for chamber) [kg\m^4], L_t is the length of connection tube in the pulsed blowing system
p,p'	mean and fluctuating pressure [Pa]
P_{abs}	absolute pressure [Pa]
q,q'	mean and fluctuating flow rate [lt\min]
Re_θ	local momentum thickness Reynolds number
Re_∞	free stream Reynolds number
$R_{t,c}$	resistance (with subscript t for tube and c for chamber)
St	Strouhal number
St_v	viscous Stokes number
t	time [s]
t^+	non dimensional time
T_{mod}	modelled time scales
T_{res}	resolved time scales
u,v,w,u',v',w'	cartesian velocity component and fluctuations[m\s], except in the boundary layer equations where u is taken to be parallel to the body surface
u_e	outer velocity in the boundary layer [m\s]
u^+	boundary layer velocity in the law of the wall variables
u^+_t	Coles modified tangential component of velocity in the boundary layer
u^*	friction velocity
V, V_{mean}, V'	total, mean and fluctuating velocity of pulsed blowing jet [m\s]
V_c	volume of actuator chamber [m^3]
$\overline{V}$	mean of velocities at the shear layer edge
V_n	transpiration term imposed as wall boundary condition for the Equivalent Inviscid Flow (EIF) [m\s]

V_0	wall transpiration velocity [m\s]
V_0^+	ratio between wall transpiration and friction velocity
V_{rms}	root mean square of velocity [m\s]
V_∞	free stream velocity [m\s]
W_{wake}	wake thickness at trailing edge [m]
x,y,z	cartesian coordinates [m], except in the boundary layer equations where x and y are taken to be parallel and normal to the body surface
X_{act}	distance between slot cut and trailing edge [m]
X_{sep}	distance between separation point and trailing edge [m]
Y_t	acoustic admittance (with subscript *t* for tube) [m^{4}s\kg]
y^+	spatial coordinate in the law of the wall variables
Z	acoustic impedance (with subscript *t* for tube ,tt for transmission tube, *cc* for compliance, *s* for slot and *act* for actuator) [kg\m^{4}s]

Greek

$\underline{\alpha}$	parameter in the wake function
α	angle of attack [°]
β	coefficient for evaluation of modelled and resolved time scales, Clauser parameter
γ	ratio of specific heats
$\Delta X_{suction}$	extension of transpiration area [m]
δ^*	boundary layer displacement thickness
δ^+	boundary layer thickness in inner variables formulation
ε	turbulent dissipation rate [m^2\s^3]
ζ	wake parameter, used in the definition of wake function
θ	boundary layer momentum thickness
θ^*	boundary layer energy thickness
θ_{inj}	angle of flow injection [°]
ϕ	generic variable used to define time and ensemble averaging
κ	turbulent kinetic energy [m^2\s^2], Karman constant
λ	square root of inverse of friction velocity, wavelength of sound
μ	dynamic viscosity [kg/m*s]
ν	kinematic viscosity [m^2/s]

π	3.1415...
Π	Coles wake parameter
ρ	air density [kg\m^3]
σ	Prandtl number
τ_w	wall shear stress in the definition of friction velocity
ψ	incompressible stream function
ω	specific dissipation rate [1\s]
$\underline{\omega}$	jet pulsation ($2\pi f$)
ω_v	characteristic frequency

Subscripts

e	boundary layer-edge, "exit"
i	inlet
L.E., T.E.	leading edge and trailing edge
v	viscous
w	wall
∞	infinity or free stream

Chapter 1

Introduction

1.1 General

In the recent years active flow control has again become a research area in the aerospace community. Active flow control differs from passive flow control in the sense that auxiliary power is required. All these techniques can be applied for the improvement of many aircraft performances, depending on the desired result. For example delaying of the separation enhancing aerodynamic performance will improve the landing characteristics and acoustic noise, and reducing or eliminating the required moving surfaces could lead to higher airframe simplicity. The endurance of High Altitude & Long Endurance (HALE) UAV can also be greatly increased since the aircraft can fly with high lift coefficient in cruise with low drag rising in this way the $C_L^{3/2}/C_D$ parameter. The suction side of this type of wings is dominated by massive separation that comprises of large and small vortices with a wide spectrum of length scales and frequencies. Recent experimental and numerical evidence shows that at high angles of attack, it is indeed possible to increase lift by controlling the vortex forming the process of separated flows. Many researchers have studied the effectiveness of such techniques (Eppler [1] for suction, Seifert & Wygnanski [2],[3], Tinapp [4] Kim-Williams [5], Gad-el-Hak [6] and Wu [7] for unsteady blowing and synthetic jet), with the current challenge being twofold: on one hand to improve the application on a real flying wing and on the other hand to acquire more physical understanding.

The final goal of this research project is to highlight the practical feasibility, advantages and limits of some of the active flow control techniques such as turbulent steady suction and unsteady blowing. The investigation will also cover aspects connected to the practical implementation of these techniques on a real flying UAV wing pointing out all technical problems related to its applications. We

will show that such technique, already proven to be applicable to multi-component airfoil, in particular for post-stall of flap, can be also extended to wing surface with single component airfoil.

1.2 Review and General Concepts on Flow Control

Separation is the detachment of the boundary layer from a surface, often to form a free shear layer associated with an adverse pressure gradient. Near wall flow is at the same time decelerated by adverse pressure gradient and accelerated by shear stress due to faster flow above. Separation point is identified by a stationary point within the boundary layer. The principal effects of separation on aerodynamic characteristics are following summarized:

- Increased drag (wide wake)
- Increased instability (formation of free shear layer)
- Loss of lift
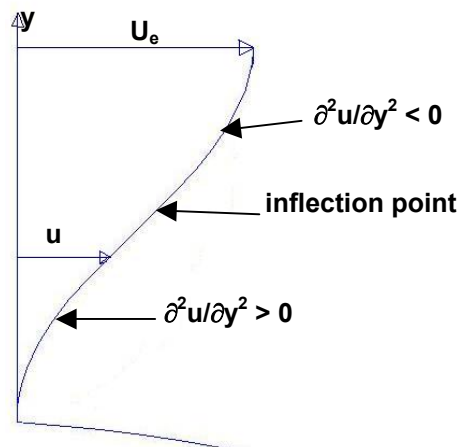
Figure 1.1: Definition of separation

With reference to the figure 1.1 it is possible to observe that when separation occur the wall shear vanish and the streamwise velocity becomes null. This condition is expressed as:

$$\left(\frac{\partial u}{\partial y}\right)_{y=0} \leq 0 \tag{1.1}$$

Observing that in the outer layer the velocity is greater than zero, the necessary condition to have separation is that

$$\left(\frac{\partial^2 u}{\partial y^2}\right)_{y=0} > 0 \tag{1.2}$$

As the second derivative of velocity profile is linked to the pressure gradient, the (1.2) can be expressed as:

$$\left(\frac{\partial p}{\partial y}\right)_{y=0} > 0 \quad \text{(necessary condition for separation)} \tag{1.3}$$

Principal aim of control methods is to modify velocity profile curvature in order to delay or eliminate separation. Separation can be weak or strong, and the classification depends on the position of separation point. When it is variable (ex: flow over wing at low angles of attack) the separation is classified as weak, while if the separation point is fixed (ex: bluff bodies or wing at high angles of attack) separation is classified as strong. In both cases the dynamics of free shear layer that detach from the surface can be influenced by a perturbation introduced into it.

Possible control strategies are mainly divided in active and passive (see figure 1.2 from Gad-el-Hak [6]), where active means that flow field is perturbed with an injection or a removal of fluid, with zero (synthetic jet) or non-zero net mass flow rate (suction and blowing). Main active control techniques are boundary layer suction to remove the low momentum fluid, wall heat transfer to control and modify the viscosity of the fluid and momentum addition to the boundary layer by steady and unsteady blowing. Nowadays, the development of "Synthetic Jet Actuators"(SJA) ("zero mass flow rate") devices has also received a great amount of interest, due to the absence of air-supply and distribution system. In steady suction or blowing the goal is to remove (suction) or add (blowing) momentum to low energy flow field, without produce excitation to the turbulent structure, while SJA and unsteady blowing promotes mixing by excitation between the higher

momentum fluid above the separated region and the lower momentum fluid near the surface.
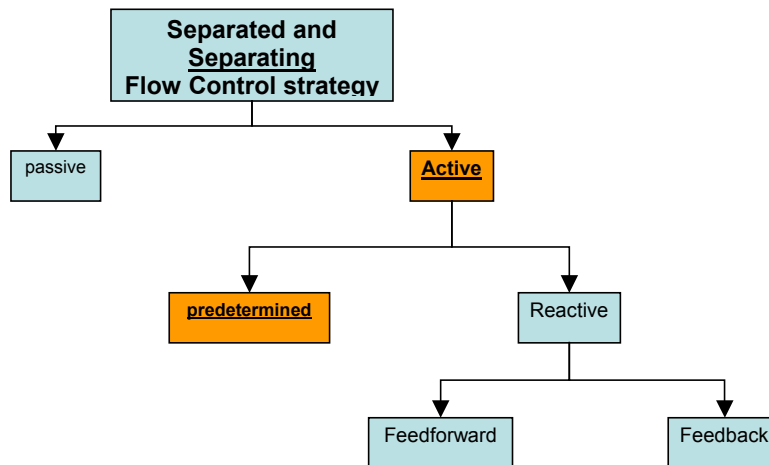
Figure 1.2: Classification of flow control strategies (from Gad-el-Hak [6])

It is important to distinguish between "separating" and "separated" flow control. The predetermined strategy in fact is more suitable for situations which tends to optimize one specified flow condition. There are many references in literature showing that a partially separated flow can become an almost fully attached flow by unsteady forcing, so that the stall can be delayed. In this category, unsteady controls are much more effective than steady ones and can be realized at lower power-input level (Wu [7],Vakili & Wu [8]; Miranda [9], Seifert & Wygnanski [2]). The category of the separated-flow control is related to the flow that has fully separated (as angle of attack increases beyond stall, fully separated flow develops and becomes a bluff -body type flow).

The active control of reactive type is that where a control signal that apply the control law is taken from measurements of the flow, whereas in the predetermined case, the control is not dependent on the flow condition. Reactive flow itself divides in feed forward, where the measured variable and the controlled variable differ

(applying a control law) and feedback. The control techniques that will be investigated in this work are classified as active and predetermined, the position of actuator that apply the control is fixed and the disturbance to the flow field are predetermined and do not change with flow conditions.

Before further proceeding is described shortly the main concepts of flow control through steady and unsteady suction or blowing.

Suction

Suction changes the velocity profile and this guarantees $\left. \partial^2 u / \partial y^2 \right|_{y=0} < 0$ which is a sufficient condition to avoid separation (figure 1.3).

An alternative, but equivalent argument, is that suction removes the slow (low momentum) fluid near the wall and replaces it with faster (high momentum) fluid. Hence is similar to steady momentum injection.
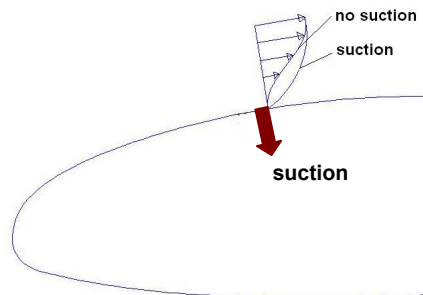
Figure 1.3: Suction concept

the key parameter that identify the suction is the ratio between transpiration velocity (V_0) and free stream velocity (V_∞), often indicated as C_q (1.4)

$$C_q = \frac{V_0}{V_\infty} \quad \text{suction coefficient} \tag{1.4}$$

suction can be applied through a porous area (distributed suction) or through a slot cut (concentrated suction).

Blowing

Blowing can be steady or unsteady. For the steady blowing the concept is similar to that ones exposed for steady suction, as the aim is to change the velocity curvature at wall modifying the boundary layer locally in the point where the control is applied (in this case through momentum injection).

With regards to the unsteady excitation an excellent review on the physics is given by [6], [7], [8], [9]. One key mechanism that has been identified in the pulsed separation control is the formation of large-scale vortical structures in the separated shear layer due to oscillatory forcing, which entrains outer high-momentum fluid into the boundary layer, delaying separation or reattaching a separated flow. The mechanism that takes place in the flow field needs to be understood in order to devise an effective method to control the flow. It is necessary to investigate how certain modes of the flow field are excited (receptivity) and amplified (resonance) by injected flow for different frequencies and strengths.

The key control parameters are the frequency (1.5) and the strength (1.6) of the disturbance, usually defined through the following dimensionless coefficient:

$$F^+ = \frac{f * X_{act}}{V_\infty} \qquad \text{reduced frequency} \tag{1.5}$$

$$C_\mu = <c_\mu> + c'_\mu = \frac{2h}{X_{act}}\left(\frac{V_{mean}}{V_\infty}\right)^2 + \frac{2h}{X_{act}}\left(\frac{V'}{V_\infty}\right)^2 \quad \text{momentum coefficient} \tag{1.6}$$

where X_{act} is the distance between the injection point and the model trailing edge, h is the slot exit extension, and f is frequency of injection.

As expected, control effectiveness varies with ratio V_{mean}/V_∞ (mean momentum added to flow field) (Seifert et al [2],[3]) up to a level where a further increase would perhaps disrupt the boundary layer. On the other hand, control effectiveness has a highly non-monotonic and non-linear variation with reduced frequency F^+ (Seifert and Pack [10]; Greenblatt and Wygnanski [11],[12]) and this not only suggests the presence of rich and multiple flow mechanisms but also suggests the possibility of

identify an "optimal" combination of this two parameters once the flow condition has been fixed.

The dynamics of a separated flow over an airfoil is dominated by the characteristic frequency of the separation region, f_{sep}, but as it has been fully explained in [13], in addition to this characteristic frequency, there are other naturally occurring frequencies that can play an important role in the dynamics of the flow. To examine this further, it is useful to classify the types of separation encountered for classical airfoils, and the subsequent discussion is drawn from classical work on stall classification by McCullogh and Gault [14], and more recent work on dynamics of stalled airfoil flows as Wu et al. [7]. Based on these previous studies, one can consider the following three situations with regards to separation control, see figure 1.4. *Case A* represents attached flow at low angle-of-attack (AOA) where the boundary layer on the suction side develops under an adverse pressure gradient but does not separate. Such a flow has one dominant time-scale characterized by the inverse of the wake shedding frequency f_{wake} which, according to Roshko [15] scales as $\sim f_{wake} \propto V_\infty / W_{wake}$ where W_{wake} is the wake thickness at trailing edge. In direct contrast to *case A* is the situation at high AOA, namely the post-stall *case C* where separation occurs near the leading-edge and the flow does not reattach to the airfoil surface. This flow behaves like that past a bluff body and is consequently subject to two frequency scales, f_{SL} (shear layer) and f_{wake} , where the former is the natural vortex rollup frequency of the shear layer and the latter is the frequency corresponding to vortex shedding in the wake. The question may be asked as to whether such a local, convective instability mechanism is important given the global, absolute instability of the wake. The answer to this question confirmed by the recent experiment, is affirmative as shown in a number of experimental investigations of bluff-body wakes. A survey of the literature in this area reveals studies (Wu et al. [7] and Miranda [9]) where both shear and wake frequencies has been considered, or in contrast, other studies of post-stall separation control where only wake frequency has been considered (Seifert [2],[3]). Finally, also many studies that have examined massively separated flow past airfoils/flaps (for

example Tinapp [4]) consider only a single frequency corresponding to the separation region, f_{sep} (which is $\propto V_\infty / X_{sep}$, with X_{sep} distance from separation point to trailing edge), which is not necessarily the same as f_{wake} or f_{SL}.
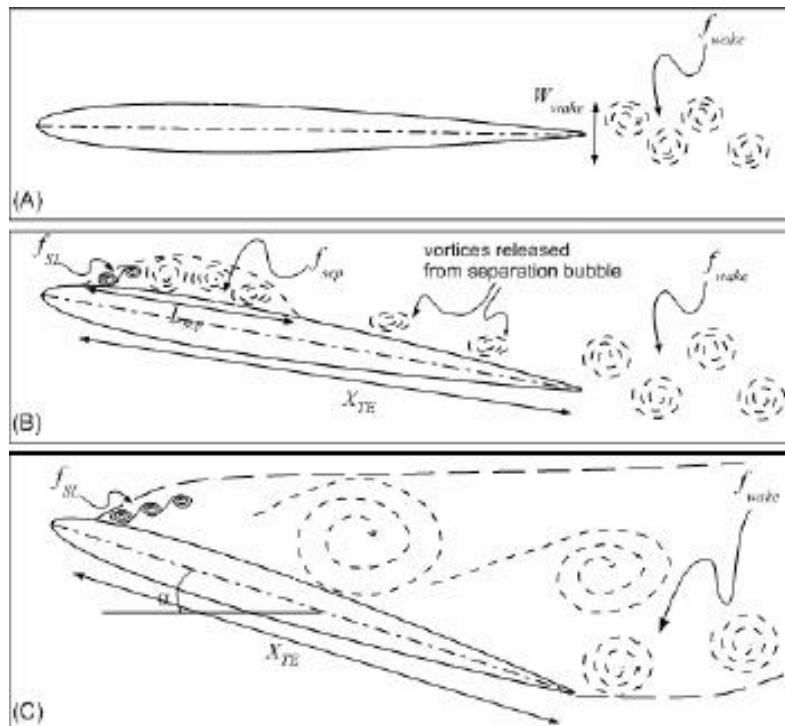
Figure 1.4: Separation and associated frequencies (McCullogh [14])

Finally Case B corresponds to the situation where separation occurs at some location downstream of the leading edge, and the separated shear layer may or may not reattach before the trailing edge. If the flow reattaches before the trailing edge, there are potentially three frequency-scales: f_{wake} , f_{SL}, and f_{sep} , the frequency scale corresponding to the separation "bubble." The resonant interaction between these processes is a strong function of the distance between the separation location and the trailing edge. In summary, f_{sep} is only one of three potentially naturally occurring frequencies in a separated airfoil flow. It is quite possible that nonlinear interactions determine the evolution of these disturbances

(Wu et al. [7],[8]). Depending on the flow condition, the optimal disturbance frequency f and injection strength could be found in order to produce positive results. However, the understanding of the dynamics of these processes is limited. In the paper of Wu [8] is summarized the fundamental physics of lift enhancement with the following chain of events:

vortex layer instability-receptivity-resonance-streaming

As Wu explains is his paper two principal typologies of instability play an important role in separated shear layers, local instability and global instability. Local instability is related to separated shear layers from leading and trailing edge, while global instability is responsible for the vortex shedding. The dimensionless parameter that identify the shear layer frequency is the Strohual number of shear layer:

$$St_{sl} = \frac{f_{SL}\theta}{\overline{V}} \tag{1.7}$$

where $\overline{V}$ is the mean of velocities at the shear layer edge, and θ is the momentum thickness. Ho&Huerre 1984 [16] remarks that for different values of $\overline{V}$ the most unstable mode for unforced shear layer is always close to $St_{SL} \cong 0.04$. This unstable frequency is referred to the natural frequency f^0_{SL} that is a decreasing function of streamwise distance from separation point (as the momentum thickness is an increasing function of streamwise distance from separation point).

The vortex shedding instead is the results of global instability, and two frequency related to the *shear* and the *shed* are present.

When the shear layer is forced the receptivity plays its role. As mentioned above the key parameter in forcing flow is the forcing frequency f, and the response of the shear layer f'_{SL} may be different from the f^0_{SL}. This depend on how the modes of shear layer are excited by external disturbance. If it is properly chosen this frequency can favourite the merging process of discrete vortices into larger ones that permit to enhance the entrainment. In this resonance condition (lock-in phenomena) the flow is more regularized. This condition is also known as "collective interaction" (Ho & Nosseir [17]). It is therefore desirable to find an

interval in the forcing frequencies that permit to modulate in a single forcing modulation the acting vortical structures.

Although momentum efficiency considerations indicate the superior efficiency of a zero- net-mass-flux disturbance, low Reynolds number studies have shown that it may be advantageous to add a small amount of steady blowing on the unsteady disturbance. This may help in controlling separation which occurs downstream of the actuator location. Frequency and strength of the disturbance are the key parameters to design an optimal active-predetermined flow control device, but also the influence of other variables can be studied in order to design an optimal control device, once the flow condition has been established. Figure 1.5 illustrates a global view of the parameters variation space. As indicated in the figure also the geometry and position of the actuator as well as the jet shape of excitation system influences the global control effectiveness.
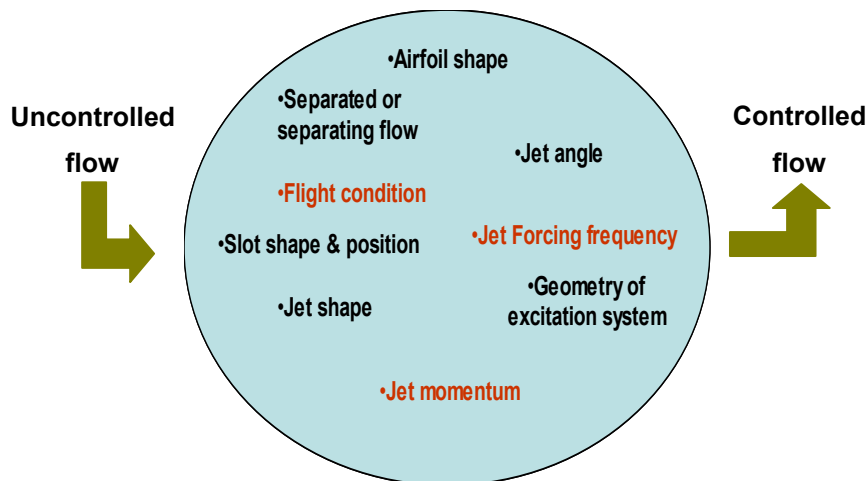
Figure 1.5: Global View of the Parameters Variation Space

In the present work the influence of some of these parameters have been studied (those red marked in the figure 1.5), the remaining studies are forwarded to future works.

1.3 Summary of Proposed Work

The investigations performed have been both numerical and experimental, and the experimental work has been divided in two part: the first on small scale model and the second on a full scale model. The work starts with numerical simulation on steady suction and unsteady blowing. To study the effectiveness of steady suction the integral methods have been used. This analysis has been performed to estimate the minimal (theoretical) amount of flow rate required to operate suction in order to estimate power required for the experimental facilities. Then it follows a note on integral methods proposing a possible extension of White&Das method based on inner variable to flow with transpiration. Then the numerical investigation of effectiveness of unsteady blowing on 2d single component airfoil has been performed using RANS approach (with FLUENT). The effect of steady and unsteady blowing on lift and drag has been evaluated varying frequencies and momentum of injected flow.

The blowing section continues with the preliminary considerations on pulsed blowing system and the design and building of an "ad hoc" rotating valve to correctly produce excitation. Then a theoretical model of pulsed blowing system has been studied using electro-acoustic analogy, pointing out all the dependences of resonance condition with geometrical parameters.

For the experimental part two tests have been performed (see figure 1.6): the first on a small scale model (21 cm in span and 40 cm in chord) and the second on a full span model (1.4 meter). Small scale model has been used with double aim, on one hand to make preliminary testing on the effectiveness of steady suction and characterization of pulsed blowing system (rotating valve-tube-actuator), On the other hand to understand the main technological problems to be faced and to quantify the benefits in order to design and build an *ad hoc* full span model (1.4 m span and 0.6 m in chord) without repeating eventual mistakes done with the small-scale model. The design and building of small scale model in presented with experimental results for steady suction varying angle of attack (extension of

separated area) mass flow rate and free stream Reynolds number. Following unsteady blowing has been investigated for small scale model, and experimental results are presented with varying angle of attack, frequencies and free stream Reynolds number. The second experimental part of the work in concentrated on design and testing of full scale model. The design and building of the model in presented with the setup of system in the wind tunnel, and primarily tests are presented on baseline configuration without control activated for both free and fixed transition. Following the results with application of control (steady and unsteady blowing) pointing out the dependencies on angle of attack, frequencies and Reynolds number on lift, drag and endurance characteristics.
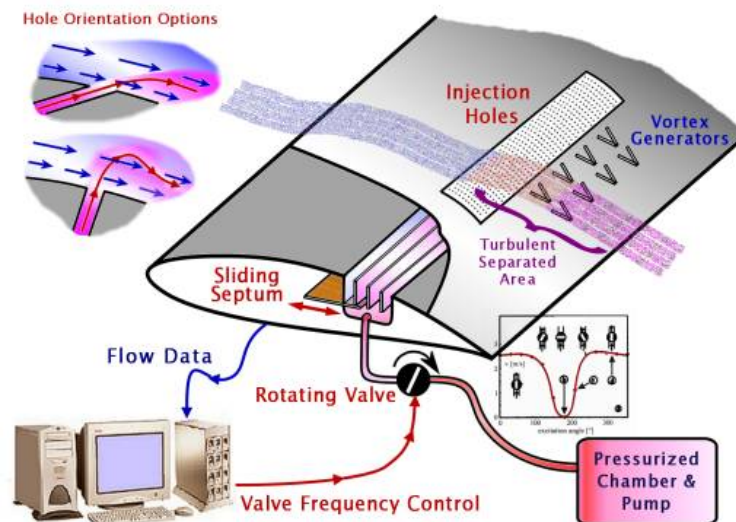
Figure 1.6: Schematic picture of proposed work

Chapter 2

Steady Suction: 2d Numerical Simulation

2.1 Numerical Model: TBVOR Code

The viscous flow filed around an airfoil has been computed using *TBVOR* code illustrated in [18,19] and developed at the Department of Aerospace Engineering of Naples; it is based on the integral momentum and energy boundary layer equations written in direct and inverse form coupled in a semi-inverse manner to the inviscid flow through normal velocity transpiration imposed at wall. The coupled method allows the treatment of "strong-interaction" areas such as laminar separation bubbles and turbulent separated flow in order to predict airfoils characteristics in stall and post-stall regimes. The inviscid flow field is solved with a panel method based on a distribution of constant sinks and linear vortices. The global scheme of method is illustrated in figure 2.1.

Strong Viscous/inviscid interaction method = potential flow field + boundary layer correction

Potential flow ⟶ **Aerodynamic singularity distribution**
(constant sink+linear vorticity)
+ closure condition

Integral boundary layer equation ⟶ • **Laminar: Direct**
• **Bubble+turbulent: Inverse – Drela**

modified   *modified*   *unchanged*

Traspiration velocity   boundary condition   closure correlation

$$V_n(s) = \frac{d\left(U_e \delta^*\right)}{ds} + V_0(s)$$

$y = 0 \rightarrow u = u(s),\ v = V_0(s)$ $H_{32} = H_{32}(H_{12}, Re_\theta)$

$y = \delta \rightarrow u = U_e(s),\ \frac{\partial u}{\partial y} = 0$ $C_D = C_D(H_{12}, Re_\theta)$

$C_f = C_f(H_{12}, Re_\theta)$
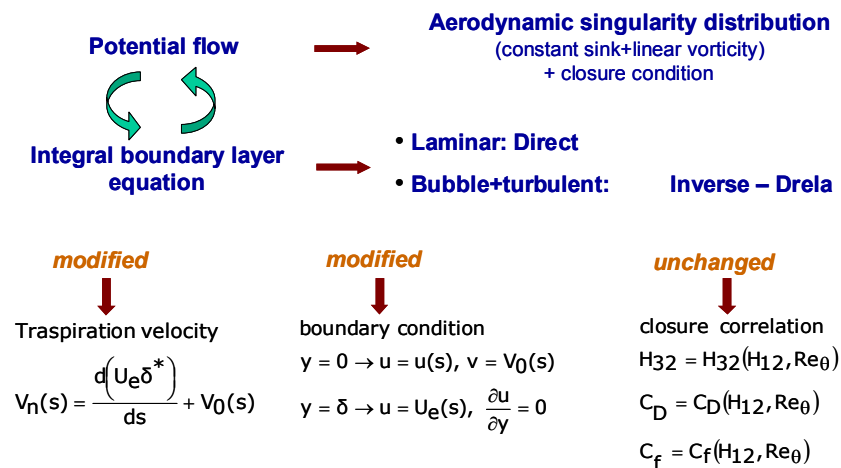
Figure 2.1: TBVOR panel method code

The results presented are evaluated for incompressible flow. The transpiration term imposed as wall boundary condition for the *Equivalent Inviscid Flow (EIF)*, has been modified to take in account the added velocity V_0: $V_n = \dfrac{d}{dx}\left(\delta^* U_e\right) + V_0$ and such term has been included in the von Karman's momentum integral equation.

2.1.1 Notes on Integral Methods with Transpiration

All the calculations presented in this part have been done without modifying the correlation functions between Cf (skin friction coefficient), H_{12} (shape parameter: ratio of displacement δ^* to momentum thicknessθ), H_{32} (ratio of energy thickness θ^* andθ), $R_{e\theta}$ (local Reynolds number based on θ), and C_D (dissipation coefficient) as indicated in figure 2.1. As proposed by Coles [20], the analytical expressions of closure correlations can be derived from integration of turbulent velocity profile as indicated in [21] and illustrated in appendix A. The idea is that for the inner variables u^+ and y^+ (2.1,.2), the velocity profile (2.3) is approximated by a logarithmic function of y^+ plus a wake function f_w which depends on the choice of wake parameter ζ and can be linear or not as showed in (2.4).

$$y^+ = \frac{u^* y}{\nu} \quad \text{where } u^* = \sqrt{\frac{\tau_w}{\rho}} \text{ (friction velocity)} \tag{2.1}$$

$$u^+ = \frac{u}{u^*} \tag{2.2}$$

$$u^+ \approx \frac{1}{\kappa}\ln y^+ + B + f\left[y^+, \zeta(x)\right] \text{ log law+law of the wake (Coles [20])} \tag{2.3}$$

the law of the wake can be expressed as:

$$\begin{cases} \text{linear}: \quad f_w(y^+,\underline{\alpha}) \approx 0.6\alpha y^+ \ \text{ with } \underline{\alpha} = \frac{\lambda^3}{Re_\infty}\frac{d}{dx^*}\left(\frac{1}{u_e}\right) \\[3mm] \text{law of the wake}: f_w(y^+,\Pi) \approx \frac{2\Pi}{\kappa}\sin^2\left(\frac{\pi}{2}\frac{y^+}{\delta^+}\right) \text{ with } \Pi = 0.5 + 0.6\frac{\alpha\delta^+}{\kappa\lambda} + \left(\frac{\alpha\delta^+}{\kappa\lambda}\right)^2 \end{cases} \tag{2.4}$$

δ^+ is y^+ evaluated at y=δ, λ is the square root of inverse of friction velocity while $\underline{\alpha}$ and Π are possible parameters to describe wake behaviour.

Together with observation that C_f is related implicitly to Re_θ and $\prod$ through u^+ calculated for y = δ, Coles propose the following curve-fit approximation (see appendix A for details)

$$C_f \cong \frac{0.3e^{-1.33H_{12}}}{\left(\log Re_\theta\right)^{1.74+0.31H_{12}}} \tag{2.5}$$

This approach is a good approximation when transpiration velocity is zero, in fact as Stevenson [22] and Sucec [23] illustrates, when transpiration is present, the overlap log-law should be modified as illustrated in (2.6) and following the same procedure followed by Coles, it results that H_{12} is a function not only of skin friction and wake parameter, but also of transpiration velocity, while C_f is implicitly related to Re_θ and $\prod$ as well as to V_0.

$$u_t^+ \cong \frac{1}{\kappa}\ln y^+ + B + \frac{V_0^+}{4}\left[\frac{1}{\kappa}\ln y^+ + B\right]^2 + 2\left[\frac{\Pi + V_0^+\,\overline{\Pi}}{\kappa}\right]\sin^2(\frac{\pi}{2}\frac{y^+}{\delta^+}) \tag{2.6}$$

Where $V_0^+ = \dfrac{V_0}{u^*}, \overline{\Pi} = -1.95\ln(\left|\dfrac{V_0}{U_e}\right|) - 3.1$ (see appendix A and [23])

In this case, it is more difficult to find a suitable curve-fit approximation, but iteration is necessary to compute the boundary layer parameters as the streamwise integration proceeds downstream.

A possible way to follow, in order to rapidly see how this modification influences friction calculation, is to try extending the integral boundary layer method proposed by White [21] based on inner variables.

In summary if is written the momentum equation in terms of inner variables and integrate with respect to y^+ from y^+=0 to y^+=δ^+, is possible to arrive at the following final equation:

$$G\frac{d\lambda}{dx^*} - \lambda H\frac{d\zeta}{dx^*} + \frac{1}{u_e}\frac{du_e}{dx^*}\left(\lambda^3\delta^+ - \lambda G\right) = Re_\infty\, u_e \tag{2.7}$$

Where G and H are inner-variable integrals (see [21] for details):

$$G(\lambda,\zeta) = \int_0^{\delta^+} u^{+2}dy^+ \qquad H(\lambda,\zeta) = \int_0^{\delta^+} \left(u^+ \frac{\partial u^+}{\partial \zeta} - \frac{1}{\nu}\frac{\partial \psi}{\partial \zeta}\frac{\partial u^+}{\partial y^+} \right) dy^+ \qquad (2.8)$$

(ψ is the incompressible stream function)

If is considered the wake function as linear, the parameter ζ is equal to $\underline{\alpha}$ (defined below), and the equation (2.7) is simplified as follows:

$$\frac{d\lambda}{dx^*}(G - 3\underline{\alpha}H) + \frac{u_e'}{u_e}\lambda\left(\lambda^2\delta^+ - G\right) - \frac{0.6\lambda^4 H}{Re_\infty}\left(\frac{1}{u_e}\right)'' = Re_\infty\, u_e \qquad (2.9)$$

This is an equation that can be integrated with a numerical integration method like Runge Kutta, once initial conditions are assumed, without any assumption on correlation between integral parameters.

The same procedure has been followed for transpired flow, with new calculation for integral G and H starting from velocity profile (2.6), and with the modification of boundary conditions that add a new term to the equation (2.9). Formally, the equation remains unchanged, but in the velocity profile used, the wake function is the law of the wake, and this would mean that in the derivative of ζ another unknown appears (derivative of Π) and, consequently, another equation should be added. The idea is to take into account the modified velocity profile in the boundary conditions and in the integrals calculation (G and H), while leaving the derivative of wake parameter unchanged, as summarized in (2.10). In this way, is possible to continue to integrate one equation once initial condition and transpiration velocity have been assigned. The final equation obtained is (2.11).

$$\frac{d\zeta}{dx^*} = \frac{d\underline{\alpha}}{dx^*} \quad \text{(instead of } \frac{d\Pi}{dx^*}) \qquad (2.10)$$

this approximation leads to:

$$\frac{d\lambda}{dx^*}(G - 3\underline{\alpha}H) + \frac{u_e'}{u_e}\lambda\left(\lambda^2\delta^+ - G\right) - \frac{0.6\lambda^4 H}{Re_\infty}\left(\frac{1}{u_e}\right)'' - Re_\infty\, V_0\, \lambda^2 = Re_\infty\, u_e \qquad (2.11)$$

Original equation (2.9) and modified equation (2.11) differ for the term that rises for the modified b.c. and from the calculation of integrals G and H.

In the figure 2.2a is showed the comparison between the solution of equation (2.11) in terms of skin friction C_f for assigned pressure gradient with only boundary conditions modified and without integrals modification and the solution of same equation but with integrals G and H changed. In both cases (zero pressure gradient and adverse pressure gradient $\propto x^{-0.15}$ for fixed rate of transpiration) it is evident how the equation (2.11)   together with approximation (2.10) is more suitable to resolve transpired flow, as the comparison with the experimental data shows (downloaded from web page of Stanford University, obtained from Andersen Kays & Moffat [24] for the case with zero pressure gradient with constant injection, and adverse pressure gradient with constant suction). In figure 2.2b the result show how different rate of transpiration produce sensible variation in the skin friction calculation for different values of suction\injection once pressure gradient is fixed. Actually, it has been considering this modification in the strong-interaction method for boundary layer calculation.
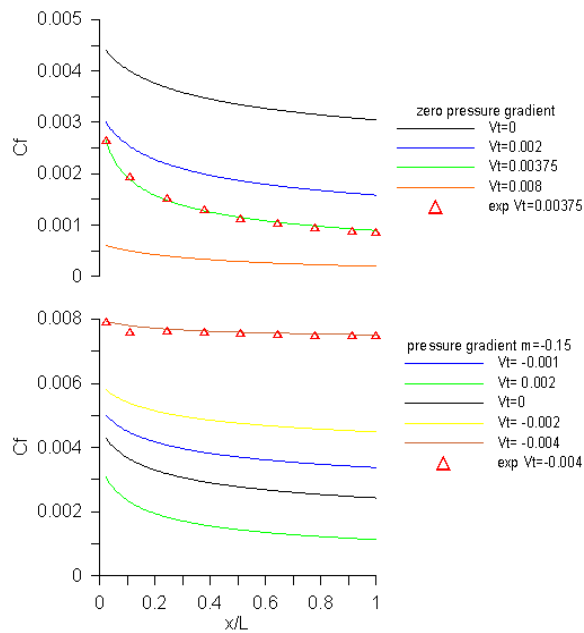
Figure 2.2a
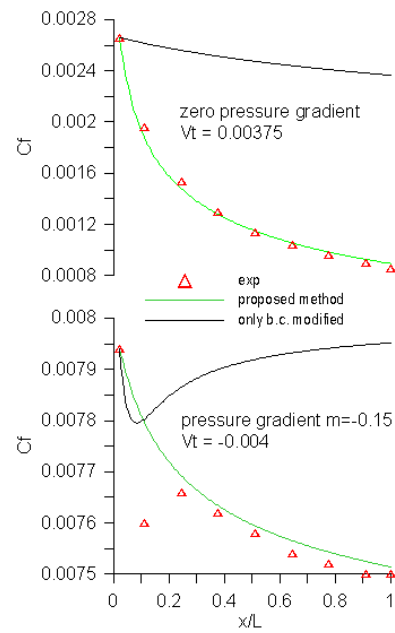
Figure 2.2b

2.1.2 Numerical Result: Best Suction Location

Incompressible aerodynamic studies have been performed to understand the more suitable location for the suction area. Three different suction area positions have been numerically tested with the same steady and uniform C_q equal to 0.006 (C_q is the suction rate defines as $V_0 \backslash V_\infty$). The CIRA airfoil considered has the maximum thickness of 20% located at 30% chord (see Figure 2.3) and it is set at an angle of attack of 9.6° with transition fixed to 40% chord and free stream Reynolds number equal to $8*10^5$. In these conditions the flow separates at about 70% of the chord as it can be clearly seen from the pressure coefficient Cp and shape parameter H_{12} distributions shown in Figure 2.4a,b,c,d. These pictures show that the best location for the suction is when it is applied upstream the separation point (from 40% to 70% chord) , while it becomes less effective when suction area is partially immersed in separated flow (from 60% to 90%) or far upstream separation point

(from 20% to 50%). Once the best suction location has been fixed, an investigation on the effect of the amount of suction to be applied has been performed and the Figure 2.5 shows these results. It can be clearly seen as the minimum rate of suction required to attach completely the flow grows as the separation point X_{sep} moves downstream ($X_{sep}\backslash c$ =1 mean separation point at trailing edge). For each C_q the corresponding flow rate for unit span has been evaluated using relation (2.12) assuming 28 m/s as free stream velocity leading to Re_∞=800000 referred to 0.4 m chord.

$$q\left[lt/min\right] = C_q * V_\infty\left[m/s\right] * \Delta X_{suction}\left[m\right] * 60000 \tag{2.12}$$

From the definition of parameter C_q, the product between free stream velocity and Cq gives the transpiration velocity that is considered constant along suction area ($\Delta X_{suction}$). The coefficient 60000 reports the result in lt/min. To obtain the total suppression of separated flow from initial condition described below (separation at 70%), a suction coefficient near 0.003 is necessary ($\approx$ 400 lt/min for 1 m span). These results have been used to localize the best position on the airfoil to set the porous plate on the surface of the wind tunnel model once the onset of separation has been established.
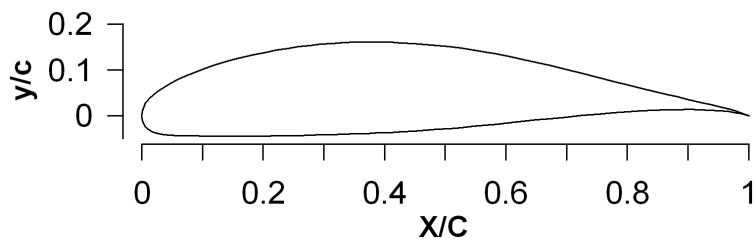
Figure 2.3: CIRA airfoil
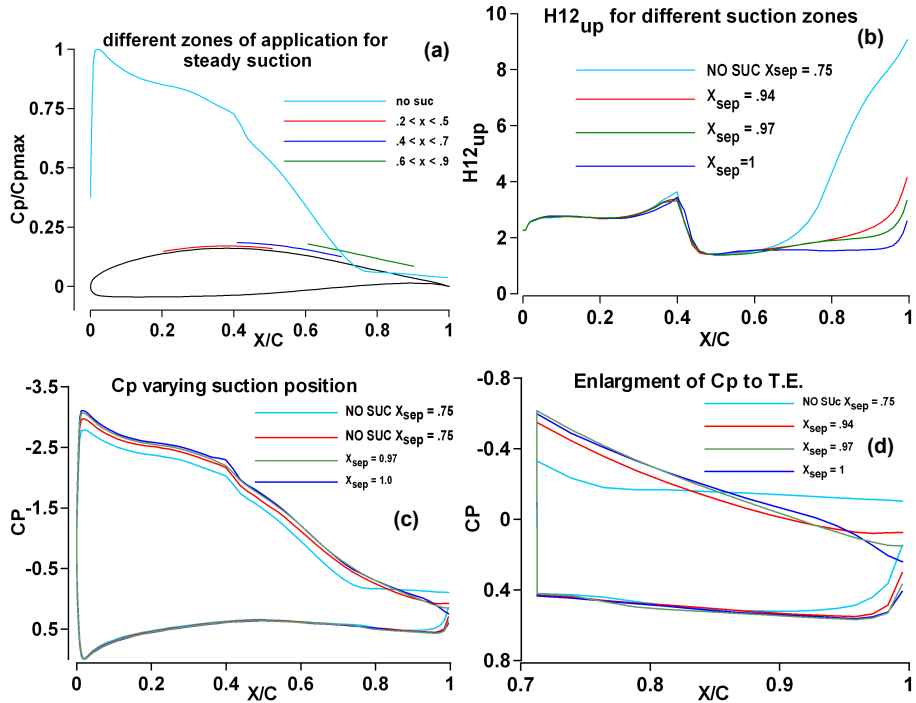
Figure 2.4a,b,c,d Numerical analysis for best suction location ($\alpha=9.6°$)
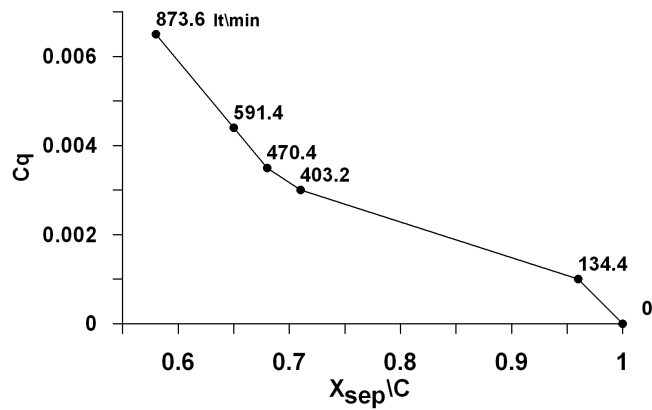
Figure 2.5: Minimum suction coefficient (and flow rate in lt\min) to reattach completely the flow from different starting condition (extension of separated area)

Chapter 3

Blowing: 2d Numerical Simulation

3.1 Introduction and Dimensionless Parameters

A numerical investigation of active flow control by steady and unsteady blowing, which can offer significant aerodynamic improvements to aircraft performance by suppressing or limiting detrimental effects of separated flow, is presented.

Many experimental work (Seifert and Wygnanski [2], Tinapp [4], WU [7],[8], Miranda [9]) and numerical investigation (Thiele [25], Ekaterinas [26], Liu & Sankar [27]) has treated the effectiveness of active flow control as tool to delay boundary layer separation with particular regards to leading edge separation for the flap in multi component airfoil. Most of the time in fact the principal goal applying this technique is the enhancement of take off and landing aircraft performance. Our scope is to verify numerically the effectiveness of such technique to delay or suppressing separation for single component airfoil in pre-stall area, with particular regard to cruising condition. As mentioned in the first chapter in fact, also the endurance of HALE UAV is the performance that would benefits from application of flow control.

The experimental work of Seifert, Tinapp and Wignanski has pointing out the strong dependency of effectiveness of active control from frequency and strength of actuation. Oscillatory blowing is about one order of magnitude more efficient than steady blowing especially if the process is actuated with frequencies that correspond to the most unstable frequency of free shear layer that detach from separation point. Reduced Frequency and momentum coefficient are indicated in (3.1a) and (3.2a) where X_{act} is the distance between actuation and trailing edge , h is the slot height and f is the frequency of disturb to the flow field. The reduced frequency is also defined as "scaled" Strouhal number (3.1a) where instead of airfoil chord as characteristic length is used X_{act}. In the (3.2b) is indicated

alternative definition of momentum coefficient through the Root Mean Square (mainly used for the experimental characterization).

$$F^+ = \frac{f * X_{act}}{V_\infty} \qquad (3.1a)$$

$$St = \frac{f * c}{V_\infty} \qquad (3.1b)$$

$$C_\mu = <c_\mu> + c'_\mu = \frac{2h}{X_{act}}\left(\frac{V_{mean}}{V_\infty}\right)^2 + \frac{2h}{X_{act}}\left(\frac{V'}{V_\infty}\right)^2 \qquad (3.2a)$$

$$C_{\mu\_rms} = \frac{2h}{X_{act}}\left(\frac{V_{rms}}{V_\infty}\right)^2 \qquad (3.2b)$$

Momentum coefficient is divided in mean and fluctuating part. If the mean part is higher than fluctuating part the flow injection is always higher than zero and a small amount of steady blowing is present (more real case). If mean and fluctuating part are equal the pulsating blowing is pure. This case is more "unrealistic" but is the ones that we are going to consider in order to isolate better the effect of unsteadiness respect the steady effect.

Seifert et al. has been observed that relatively large quantities of steady blowing (c_μ= 2-10%) near the point of separation can delay separation or reattach the flow and increase lift but the steady blowing may also cause a thickening of the boundary layer and the wake behind the airfoil which could leads to increased drag and globally detrimental in efficiency. In contrast the pulsed blowing takes advantage of inherent local instabilities in the near-wall shear layer that that detach from separation point and causes the selective amplification of the input oscillation frequency. Convective motion moved these disturbances downstream along the surface as coherent large structures that promote mixing between the boundary layer flow and gives contribute to delay separation. Pulsed blowing has proven to be a reliable technique for separation control with the most effective location for unsteady forcing near the point of separation and the optimum reduced frequency for the oscillations is about $F^+ \approx 1$. Sensitivity analysis with frequency, momentum and jet injection angle is presented.

3.2 2d RANS Simulation

The numerical simulation is based on Reynolds Averaged Navier-Stokes equations (RANS), Fluent Version 6.1.22 is a CFD computer code developed and marketed by Fluent Inc. The code solves the equations for conservation of mass, momentum, energy and other relevant fluid variables using a Finite Volume technique. First the fluid domain is divided into an appropriate number of discrete control volumes (cells) using a pre-processor code which creates a computational mesh on which the equations can be solved. The meshing software used and available with Fluent has been Gambit.

Nevertheless the many advances of Computational Fluid Dynamics in the past twenty years, the modeling of turbulence phenomena continues to be an important problem. The most common numerical approach used to treat turbulent flows is to devise a model able to take into account the global effect of turbulence on the mean flow quantities. This is the basic assumption behind the RANS approach. The RANS equations are derived from the Navier Stokes equations by using a time-average operator. This procedure introduces additional unknowns that have to be modeled in order to close the system of equations. The RANS methodology attempts to calculate a turbulent flow field without actually resolving the turbulent eddies, but using a model which depends to the mean flow only.

In RANS, we divide the flow variables into one mean (time-averaged) part and one turbulent part (see figure 3.1). The latter one is modelled with a turbulence model, converting turbulent fluctuations into Reynolds stresses to be modelled opportunely, while leaving the large scale, rotational motions to be resolved as unsteady phenomena. In summary RANS approach models the turbulence and resolves only unsteady, mean flow structures, primarily larger than the turbulent eddies. This is the focal point to be checked, in fact for many type of flows it is not adequate to use RANS, since the turbulent part can be very large and of the same order as the mean. Examples are wake flows or flows with large separation. More sophisticated   techniques   (but   that   contemporary   requires   much   more

computationally resources) attempt to resolve more in deep the turbulence structure modelling only the small eddies (Large Eddy Simulations), or resolving the Navier Stokes equation completely in the flow field from the large structure to the Kolmogorov scales (Direct Numerical Simulation). The using of RANS method to treat unsteady turbulent flow requires particular attention as indicated in [25]. The using of "average approach" implicitly imposes the assumption of using time-averaging (3.3a) instead of ensemble-averaging (3.3b). As the RANS method does not consider the back-scatter mechanism for the transfer energy from small scale turbulence to large scale turbulence, the applicability of this method requires the existence of spectral gap of one or two orders of magnitude between time resolved and time modelled scales.

$$\langle \phi \rangle = \langle \phi(x) \rangle = \lim_{T \to \infty} \frac{1}{T} \int_0^T \phi(x,t) dt \quad \textit{time averaging} \tag{3.3a}$$

$$\langle \phi \rangle = \langle \phi(x,t) \rangle = \lim_{N \to \infty} \frac{1}{N} \sum_{i=1}^{N} \phi_i(x,t) \quad \textit{ensemble mean} \tag{3.3b}$$

ϕ is the generic variable (for example velocity or pressure)

Problems occur if some of the resolved scales are modelled and "*vice-versa*". To check in advance the applicability of RANS Rung [28] suggest to evaluate the spectral gap evaluating the ratio between resolved and modelled time scale as indicated in (3.4), where St is the Strouhal number of the flow that depend on shedding frequencies and the coefficient β is included in the range [1,10] for the boundary layer flow and [0.1-1] for free shear layer.
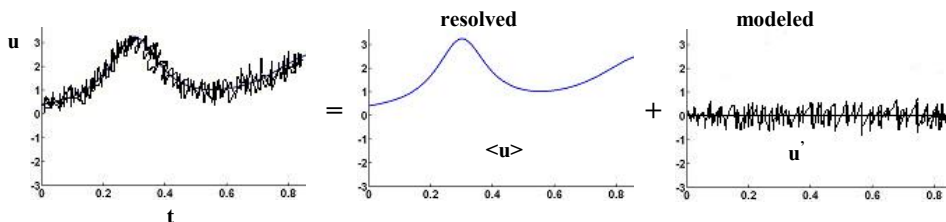
Figure 3.1: RANS approach

$$\frac{T_{mod}}{T_{res}} \cong \beta \frac{Re_{\infty}^{1/5}}{St} \tag{3.4}$$

The pulsating disturbance to the flow field is imposed as indicated in (3.5), where the fluctuating part as sinusoidal wave form is superimposed to the mean value of injection V_{mean}. The maximum fluctuation is equal to the mean value, the minimum velocity is zero. By changing frequency *f* it is possible to perform sensitivity analysis with frequency, and the steady blowing is obtained through the same formula by considering frequency equal to zero. Momentum coefficient effects can be studied by changing the amount of mean velocity V_{mean}.

$$V(t) = V_{mean} + V' = V_{mean} + V_{mean} * \sin(2\pi ft) \tag{3.5}$$

3.2.1 Computational Grid and Numerical Settings

The airfoil investigated is the same used for suction analysis (CIRA airfoil) but differently from the case treated for suction, in this case in order to simulate realistic "*construction*" situation a slot cut slightly modifies the geometry of the airfoil locally, in order to permit inlet for pulsating flow (see figure 3.2). The slot exit has dimension of 0.8 mm and can be modelled as wall boundary condition (no control applied) or inlet boundary condition (steady and unsteady blowing). As remarks it is possible to vary the inlet velocity orientation simple modifying the angle between the velocity and the normal to the slot without modify the geometry. The computational C-TYPE grid is illustrated in figure 3.3. It has been obtained with 2 blocks for a total of 31500 cells. First one with 340 points on airfoil (opportunely clustered in order to provide definition at leading edge, slot and trailing edge) and 60 normal to the wall. The second surrounding the first one with transition zone from 360 point to 120 and 35 points in the normal direction. Also others 2 grid with 22000 and 75000 cells has been tested without substantial modification in the results.
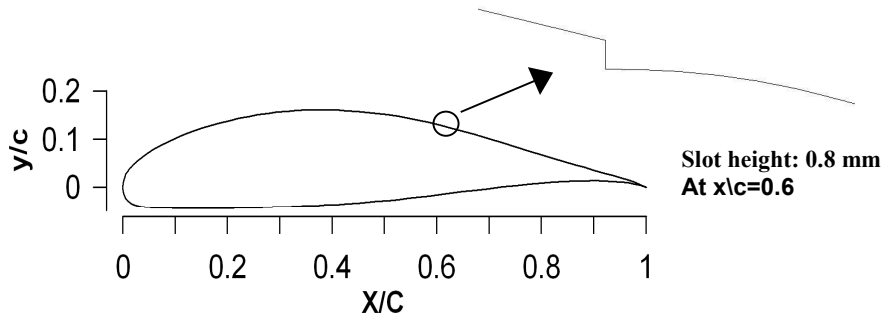
Figure 3.2: Airfoil and particular of slot

In the wake 60 points have been used and the grid is extended from 15 chord upstream the leading edge to 20 chord downstream the trailing edge. The number of points along streamwise airfoil direction is kept high for the reason that this airfoil has been designed using the "Stratford" philosophy, so the expectation suggests that it should be characterized by strong upside pressure recovery and skin friction close to zero for a big extension of airfoil. To correctly capture this behaviour the maximum aspect ratio of cells near the surface has been kept less than 100, and the first cell height has been fixed at $3*10^{-5}$ m ($Y^+ \approx 1$), as for this analysis the wall function approach has not been used.
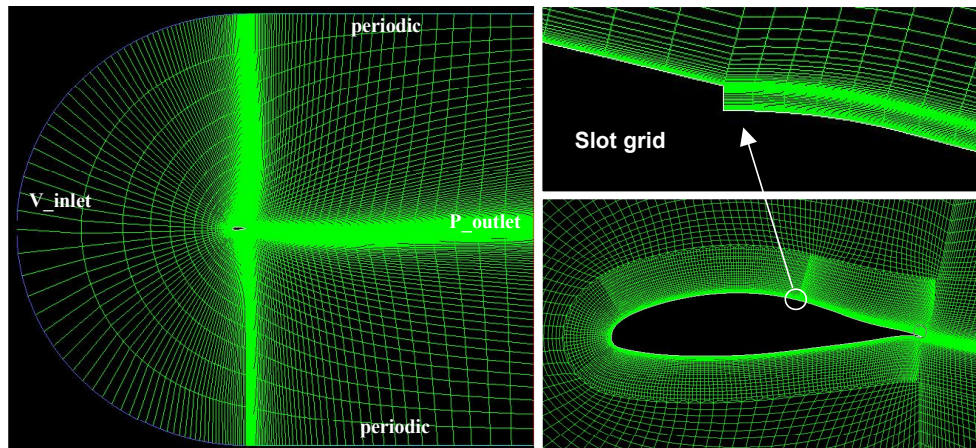
Figure 3.3: Computational grid and particulars

The solver settings are implicit and segregated (the equation set is solved sequentially) with second order in space and time. The pressure correction algorithm is SIMPLEC (Semi-Implicit Method for Pressure-Linked Equations-Consistent). Boundary condition are velocity inlet far upstream of airfoil (with velocity module of 18.7 m\s equivalent to Re_∞ of $8*10^5$) , periodic on the top and bottom of domain and pressure outlet far downstream. The surface of the profile is considered no slip walls except for slot that can be considered both wall (when actuation is not activated) and also velocity inlet when actuation is activated (through definition of User defined Function). Inlet turbulence is kept low with intensity less than 0.1% (DPA wind tunnel turbulence level).

The aerodynamic performance of this kind of airfoil (Stratford recovery) strongly depends on transition location, the pressure distribution change drastically when the position of transition moves a bit downstream or upstream. As we are interested to avoid effects non directly dependent on control in order to isolate evaluation of effectiveness of blowing (deleting others effects), transition point has been fixed to 4% in chord on the upside and 50% on the lower side. In this configuration the flow condition are close to the fully turbulent. As we will see in the future chapters this has been the same approach that we have used in the experimental part with full scale model.

Many turbulence model that are available in FLUENT, from which the three more used for airfoil aerodynamics are Spalart-Allmaras (SA), k-ϵ with option to model near wall region without wall function (case of our interest) and k-ω with correction for Shear Stress Transport (k-ω SST) that use damping function to change gradually from k-ω in the near wall region (where it works better than k-ϵ) to k-ϵ in far field region (where the k-ω falls). As Thiele [25] suggests the SA model is more robust respect k-ω or k-ϵ, but this model present a very low level of unsteadiness captured for oscillating flow respect experimental evidence. To correctly capture unsteadiness the two equation model are more indicated (they take into account the "story" of the upstream flow through the lag equation).

The standard k-ω model in FLUENT is based on the Wilcox k-ω model, which incorporates modifications for low-Reynolds-number effects, compressibility, and shear flow spreading. A variation of the standard k-ω model called the k-ω SST model was developed by Menter to effectively blend the robust and accurate formulation of the k-ω model in the near-wall region with the free-stream independence of the k-ε model in the far field. To achieve this aim, the standard k-ω model and the k-ε model are combined together by a blending function. The blending function is designed to be one in the near-wall region, which activates the standard k-ω model, and zero away from the surface, which activates the k-ε model.

These characteristics make the k-ω SST model more accurate and reliable for a wider class of flows, with particular regards for airfoils flows in comparison with the standard k-ε model. For the computation presented the k-ω SST model has been used.

For unsteady calculation an appropriate time stepping should be used. For situation where no control is applied, even though the simulation can be done in steady condition, at high angle of attach high separation occur, and the flow becomes intrinsically unsteady. For this reason also when control if "*off*" the unsteady simulation is performed and a non dimensional time stepping equal to 0.01 is used as indicated in (3.6). This is equivalent to choice a sampling rate of 3 kHz (more than enough to capture unsteadiness with frequency up to 100 Hz).

$$\Delta t_1^+ = \frac{\Delta t \, {}^* U_\infty}{c} \quad \text{non dimensional time stepping (c is the airfoil chord)} \qquad (3.6)$$

When actuation is applied the constraint for the time stepping is changed, is has been kept equal to the minimum value between the time stepping defined above in the (3.6) and the time stepping obtained from the consideration to have al least 100 time stepping to describe one pulsating cycle for oscillating injection, see following (3.7).

$$\Delta t_2^+ = \frac{1}{100 * f} \longrightarrow \Delta t^+ = \min\left[\Delta t_1^+; \; \Delta t_2^+\right]$$
(3.7)

3.3 Results

3.3.1 Control OFF

The baseline results (control not activated) are presented. Aerodynamic characteristics have been evaluated for CIRA airfoil with fixed transition and Re_∞ equal to $8*10^5$.

Due to the high level of separation that this profile has showed also at angle of attack much lower than the stall angle, the steady simulation has been performed as initial condition for the unsteady simulation, and once the oscillation reach convergence the mean values of variable has been evaluated (see figure 3.4 as example of convergence history for lift). In the figures 3.5 and 3.6 the lift and polar curves. From unsteady simulations have also been estimated the Strouhal number and reduced frequencies of the detached shear layer as function of angle of attack, and the correspondent lift oscillation as percentage of the mean value (see figure 3.7). As is possible to see the frequencies of lift oscillation reach a peak at angle of attack equal to 12° where the Strouhal number is equal to 1.8. In this condition the ratio between modelled and resolved time scales is higher than 10 (following the 3.4) and the validity of RANS can be assumed.

As it is possible to observe from lift and polar curves, while the airfoil stalls at very high angle of attack, with a maximum lift coefficient of 1.75 at α=25°, the maximum efficiency is obtained at lower angle of attack, α=4°. Figure 3.8 shows three examples of pressure distribution for three different flow condition: completely attached flow (6° black line), partially separated flow (12° red line) and pre-stall condition (25° blue line). From the figure 3.8 it is also possible to see the typical "Stratford" pressure recovery with a suction peak followed by long "*platoe*" (condition of attached flow 6 and, 12°). Another observation is relative to 12°, when even if the airfoil is sufficiently far from stall, it present an extension of separated

area near 40%. As the angle of attack increase, the separation moves in upward direction, but also the leading edge suction peak side continues to rise, and the global balance remain in favour of an increment of lift. Only when the flow detaches completely from the leading edge the stall occurs. In the pre-stall condition approximately the 70% of the airfoil flow is separated.
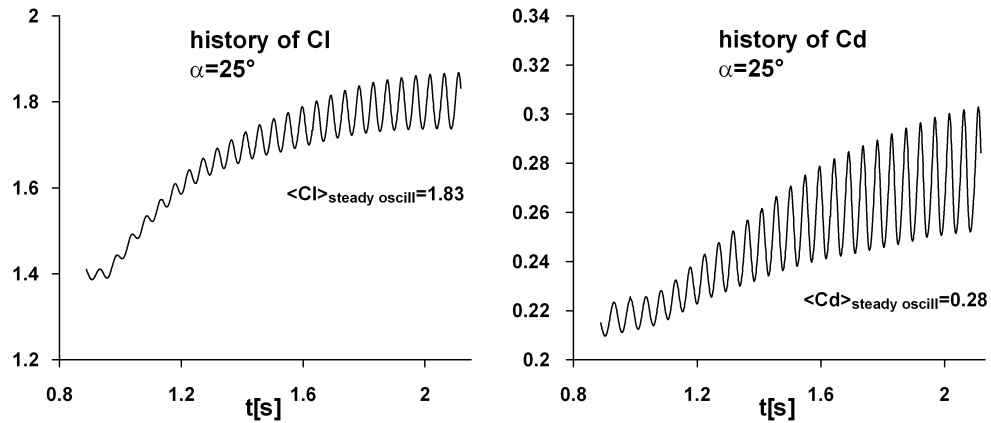
Figure 3.4: Example of convergence history for unsteady simulation (control OFF)

$Re_\infty = 8*10^5$
Baseline Results: Control OFF
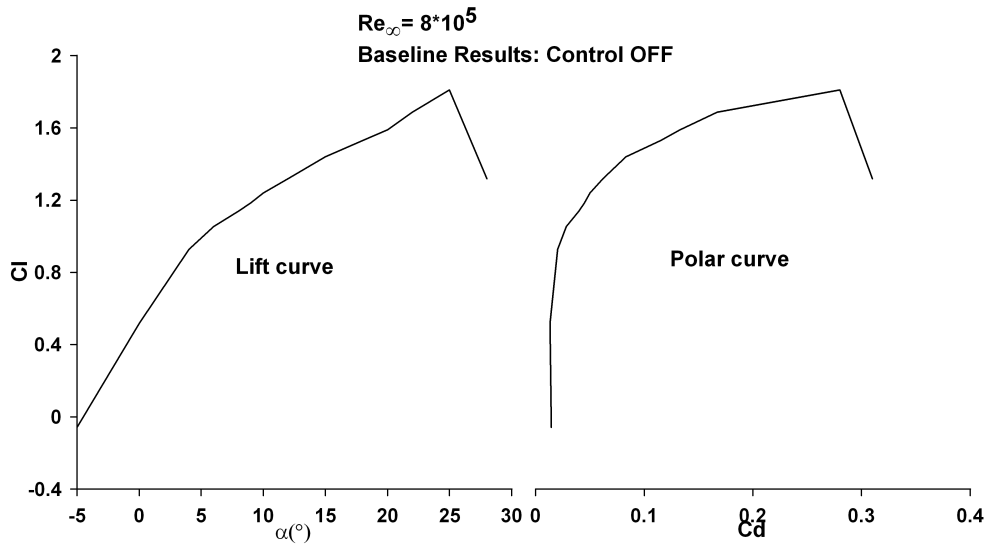
Figure 3.5 Lift coefficient curve   **Figure 3.6:** Polar curve
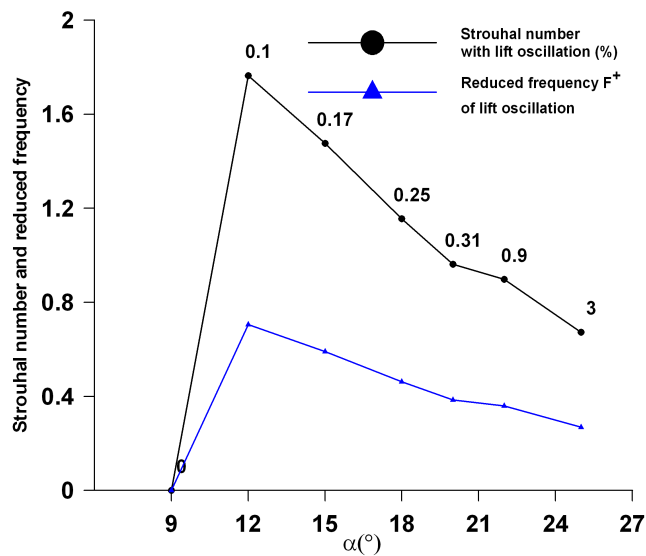
Figure 3.7: Strouhal number and reduced frequency variation with angle of attack. Frequency determined from the lift coefficient spectra. Labels show the lift coefficient oscillation in % of the mean value
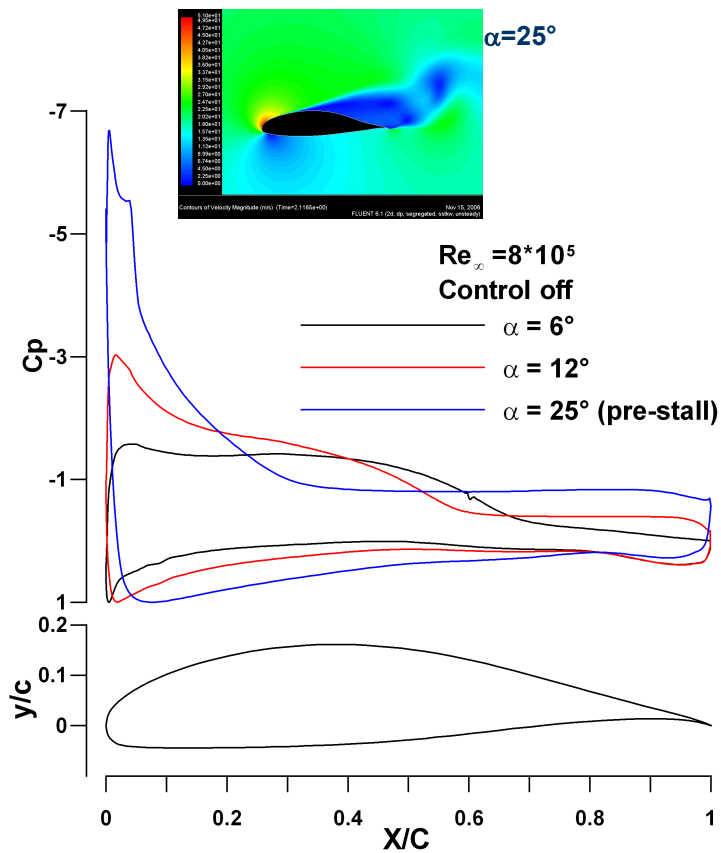
Figure 3.8: Pressure distribution for 3 angles of attack with control OFF velocity contour for pre-stall angle

3.3.2 Control ON: Frequency Effect

In this section the control is activated with steady and unsteady blowing for different frequencies, and the results are compared with baseline data obtained in the previous section. Primarily the frequency effect has been analyzed varying only pulsation of the injected flow, with the momentum coefficient kept constant. In the second part the effect of momentum coefficient is presented varying the mean velocity and keeping the frequency constant.

The control law has the wave form as indicated in (3.5) with mean value of velocity equal to 15 m/s. This value of velocity correspond to the momentum coefficient $C_\mu = 4*10^{-3}$ (0.4% percentage of added momentum respect to the free stream momentum).

In a range of angle of attack that goes from 4° to 25° five different actuation frequencies have been numerically tested, 0-30-50-80-120 Hz. The value of 0 Hz means that only steady part is activated (steady blowing). The aim is to recognize at each angle of attack the frequencies (either one or more than one) that best "*lock*" with the flow structure, and eventually individuate a general rule to predict system behaviour. It is also important monitoring both lift and drag, in fact it is not predetermined in advance that an optimal condition for lift would coincide with the condition that also maximizes the drag reduction.

The numerical simulation has been performed starting from steady solution and applying sequentially first steady blowing and then pulsating control with f=30Hz-50Hz-80Hz-120Hz. The duration in time for each frequency is not predetermined in advance, as the transient time could vary when the actuation frequencies are changed.

Some examples of a complete simulation is reported in the figures 3.9,.10,.11,.12 case (a) and (b) for four angles of attack, 4°,9°,12°,18°. Lift responses with frequencies (blue line) is compared to the uncontrolled case (black line) and the steady blowing case (red line). For the case of α=4° when the control changes from steady to pulsating flow with frequency of 30Hz, the lift starts to oscillate and reaches a steady mean value of 0.93 with oscillation around the mean value of 0.03. If the frequency increase to 50 Hz or 80 Hz the mean value of lift remains almost unchanged but the oscillations are lower (from the design point of view this situation ideally is preferable as less oscillations mean less structural fatigue). When the frequency is switched to 120 Hz the control is less effective with the lift reaching 0.9. The results globally not present a lift enhancement, in fact the value of baseline solution with control off (black line) is 0.92. As anticipated the correspondent results for drag (figure 3.9b) do not respect exactly the behaviour of

those related to lift; in fact the mean value produced with pulsating injection remains close to the value of uncontrolled case, and change a little with frequency but globally it does not produce appreciable positive results. The worst condition is when the steady blowing is applied. Its application produces drag increase instead of reduction. The control in this case produces disturbs to the flow field and it has negative effect on lift and weak negative effect on drag. The situation obtained with angle of attack equal to 9° present very different behaviour for lift but at the same time there is also a sensible reduction in drag at different frequencies. This is due to the fact that at this angle of attack the flow is partially separated and the shear layer exists, differently from the situation with angle of attack equal to 4° where the flow is completely attached. When the flow field around the airfoil presents partially separation the interaction mechanism between pulsating injection and shear layer starts to produce results and the control starts to be effective. The effectiveness, as mentioned in the introduction, catches the maximum when the control "locks" with the most unstable wave in the shear layer. In this situation the energy of the pulsating jet is convected downstream and the enhancing of mixing is obtained. In the figure 3.10 it is possible to observe how the lift enhancement produced by steady blowing is much more less effective than the ones obtained with pulsating control.

Considering the results for angle of attack 12° (see figure 3.11) the curves respect the overall behaviour obtained for 9°. Lift is increased and drag is reduced, and also the fluctuations respect the mean values continue to be present. The situation changes distinctly for the angle of attack equal to 18° (see figure 3.12). The application of pulsating control produce a considerable lift increase when the frequency is equal to 50 Hz respect to others values, and this value can be identified as the optimum for the lift coefficient. The situation change if the drag reduction is considered. The frequency of 50 Hz is contemporary the best for lift improvement and the worst for the drag reduction (respect to the others). This suggest that the best control law changes depending on the variable that would be optimized. Figure 3.13 illustrates the comparison between pressure distributions for

an angle of attack equal to 12° and 3 different levels of excitation: steady blowing (red line), 30Hz (blue line) and 120 Hz (green line). It is also illustrated the contour of velocity in the rear part of airfoil for the three excitation level. It is clearly visible as the excitation at frequency 30 Hz is more effective than instead of steady blowing and pulsation with frequency of 120 Hz. When the pulsation is applied with f=30Hz the mixing in the boundary layer is favourite and as results the separation point moved upstream.

In the figure 3.14 the summary of results with control activated are illustrated for lift and polar curves compared with uncontrolled case. To examine better the results, it is also interesting to study the percentage variation of lift and endurance with respect to the uncontrolled case. This is illustrated in figure 3.15a,b, where it is possible to observe the gain in lift (3.15a) changes with angle of attack and frequency, differently from the gain in endurance. For example if the attention is concentrated on the angle of attack of 12° the best lift enhancement is obtained with frequency of 30 Hz (blue line) and is equal to 23%, but considering the endurance the best frequency becomes 50 Hz (pink line). This non monotonic behaviour is repeated also at 15° and 18°. Another consideration is that even if the attention is fixed on one characteristic, for example on lift, it does not exist single optimal frequency for all angles of attack. In the lift curves is possible to observe that the frequency of 30 Hz (blue line) is the best one until the angle of attack is less than 15°. For the values of α equal to 18° the curve related to frequency of 30 Hz falls down and the lift increase related to pulsation with frequency of 50Hz becomes higher. In summary it is possible to consider that with regards to lift at low angles of attack the low frequencies produce better results than high frequencies, while the opposite happens at high angles. If the endurance is the principal aim to be maximized also the drag has to be considered and the frequencies 50 Hz and 80 Hz globally produce better results. In particular the frequencies of 30 Hz is the ones that shows best results at lower angles compared to the others and it is the best one at high angles, while the frequency of 50 Hz is the best one if the characteristic of endurance is considered both at high and low angles of attack.

This alternation between the optimal frequency for lift is probably due to the fact that the most unstable frequency in the shear layer that detaches from the airfoil surface, changes with angles of attack and the actuation that best "lock" with it change consequently. But if the wake is also considered in the interaction mechanism (and consequently the main objective is the endurance) it is possible to individuate a more regular behaviour as indicated in figure 3.15b where the frequency of 50 Hz (F^+=0.64) seems to give the best results. The same results are showed in the figure 3.16a,b where efficiency and endurance are reported for different actuation frequencies and angles of attack. It is more evident how the optimal condition changes depending the objective to be optimized. If is considered, for example, the green line (related to angle of attack of 15°) the optimal frequency for efficiency is individuate in 120 Hz while clearly for the endurance the optimal frequency is 50 Hz. the same behaviour also for 18° and 12°, while for 9° and 6° the optimum for efficiency coincide with the optimum for endurance. One possible explanation is that when the separation becomes strong also the non linear interaction between vortex structures becomes stronger and non intuitive phenomena occurs.
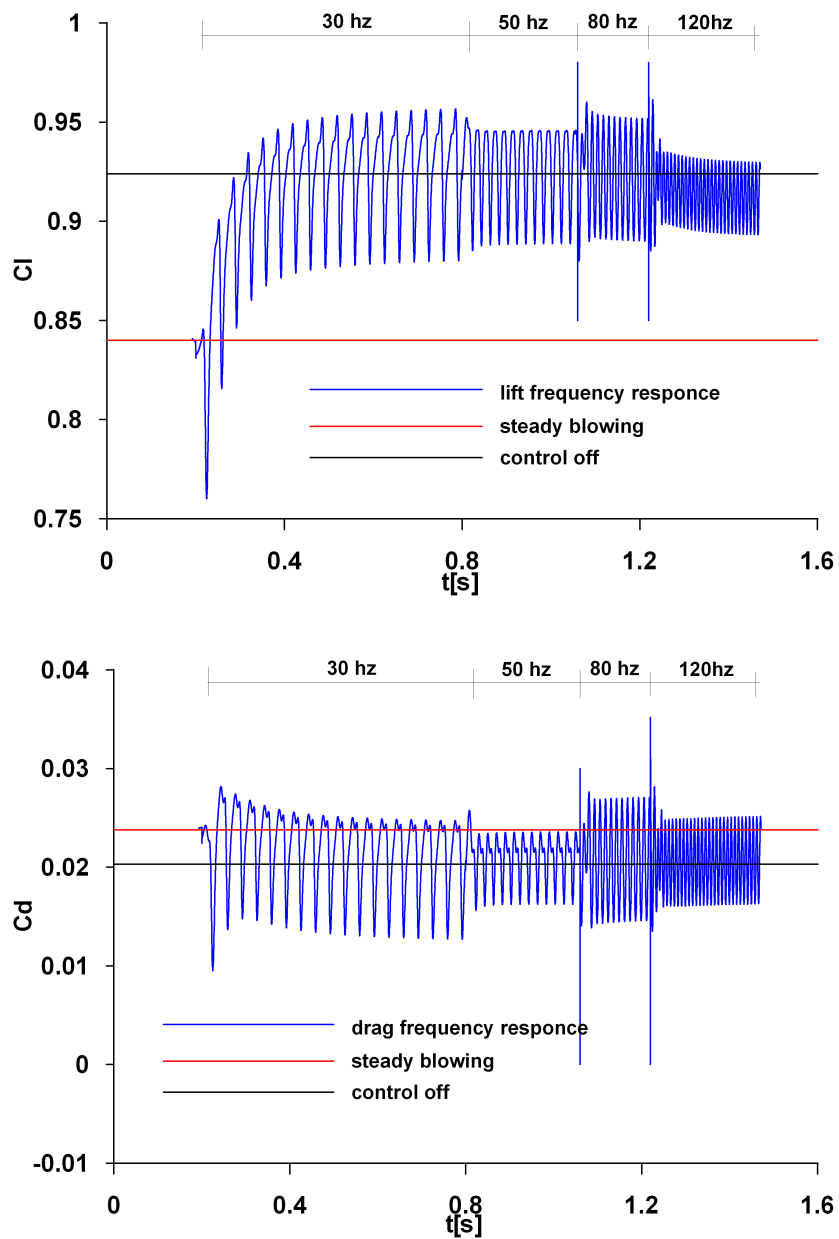
Figure 3.9: Lift (a) and drag (b) coefficients history with frequencies variation compared with uncontrolled case and steady blowing case, $\alpha=4°$
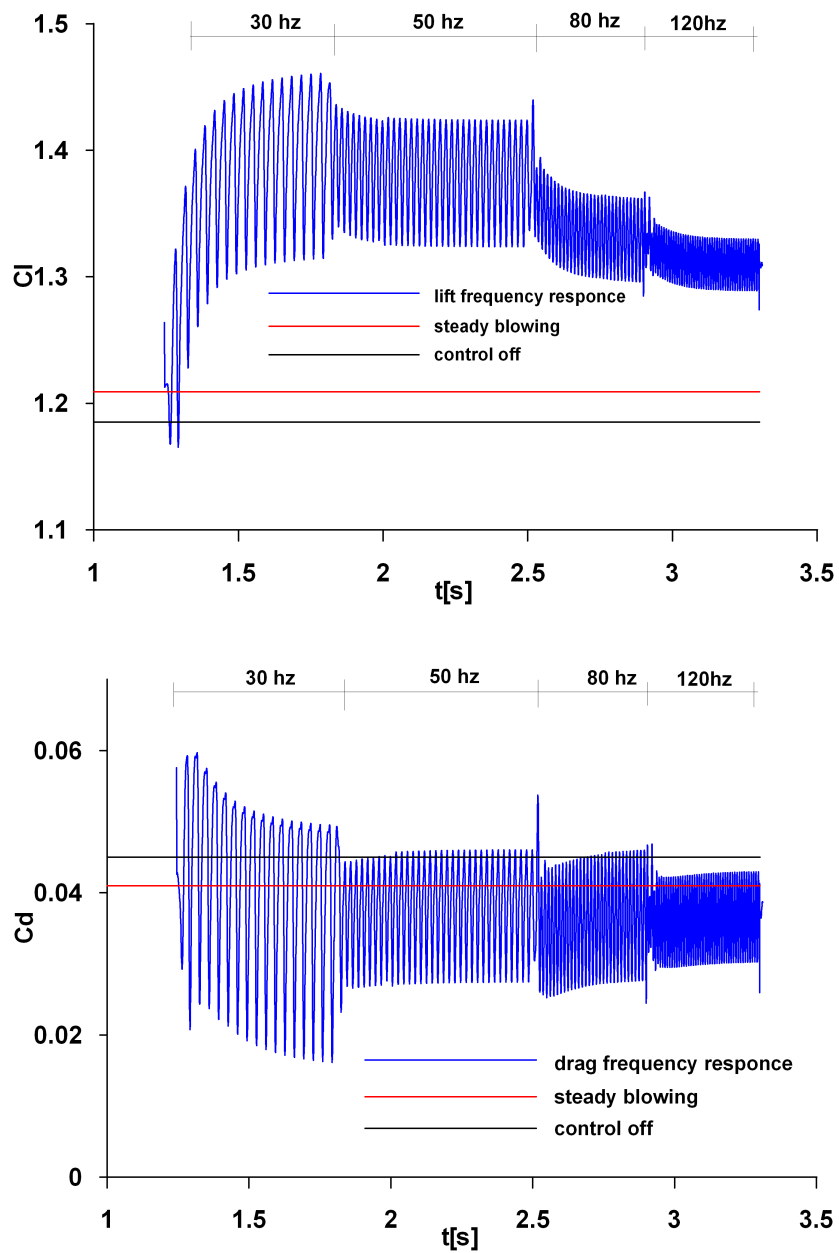
Figure 3.10: Lift (a) and drag (b) coefficients history with frequencies variation compared with uncontrolled case and steady blowing case, $\alpha=9°$
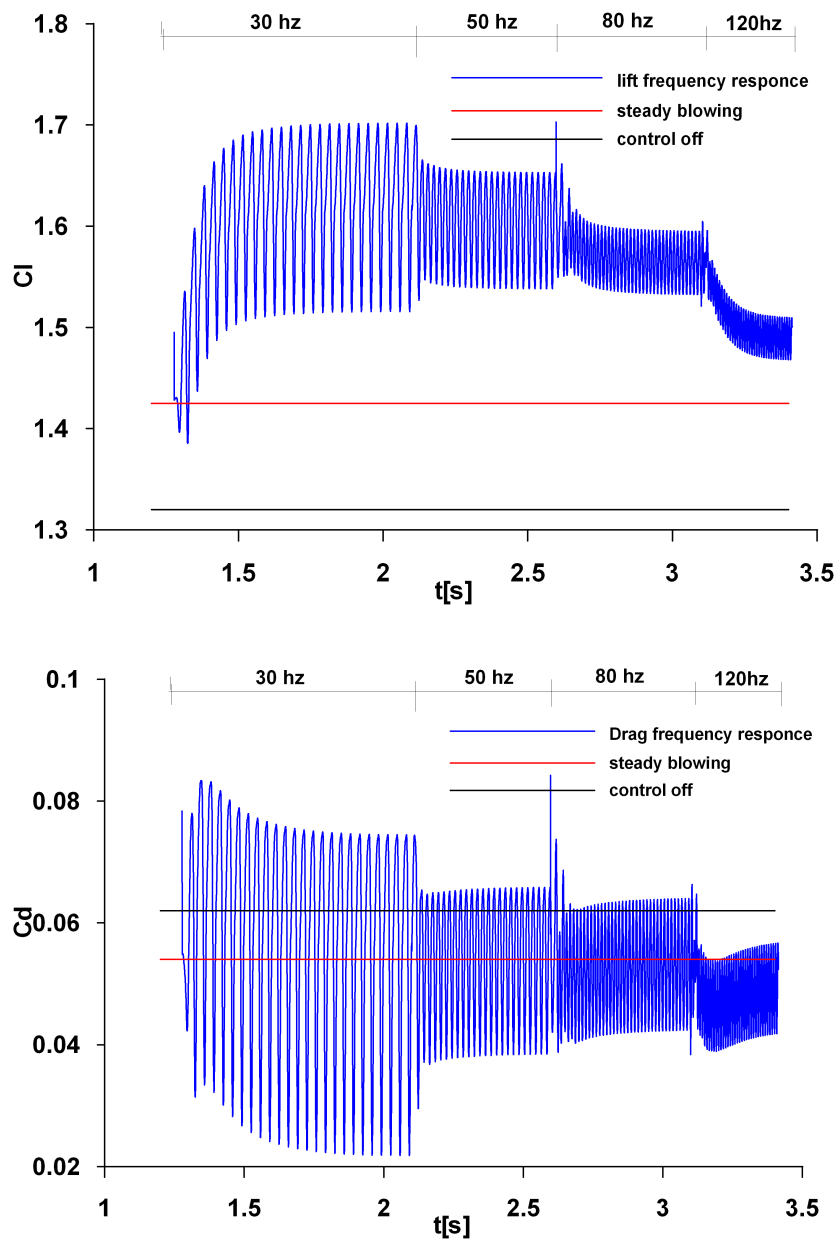
Figure 3.11: Lift (a) and drag (b) coefficients history with frequencies variation compared with uncontrolled case and steady blowing case, $\alpha=12°$
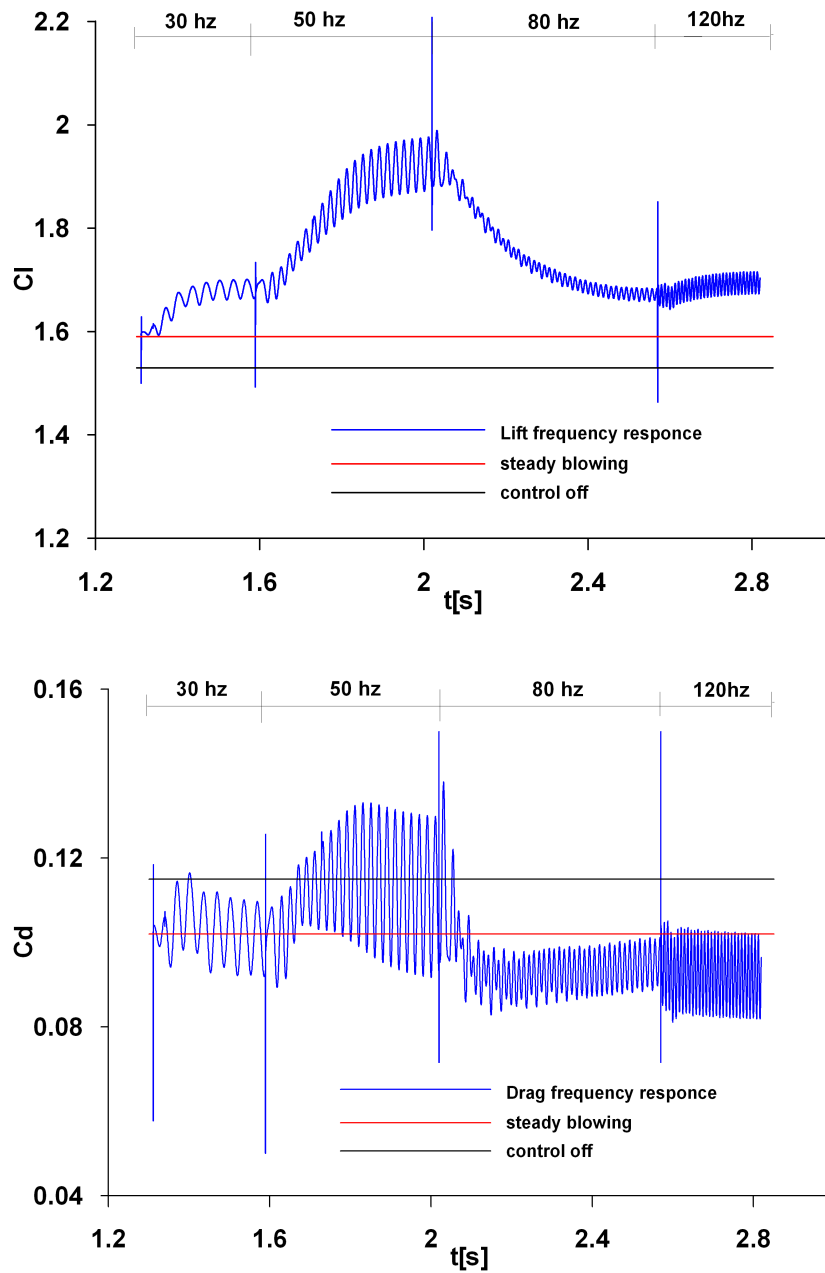
Figure 3.12: Lift (a) and drag (b) coefficients history with frequencies variation compared with uncontrolled case and steady blowing case, $\alpha=18°$
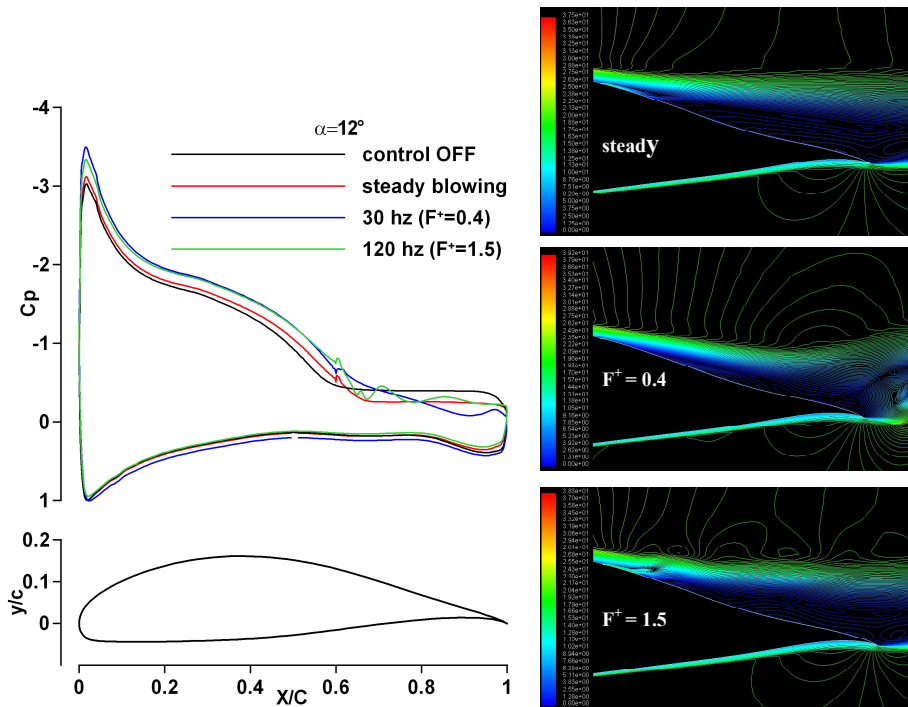
Figure 3.13: Comparison of pressure distributions and velocity contour for α=12°
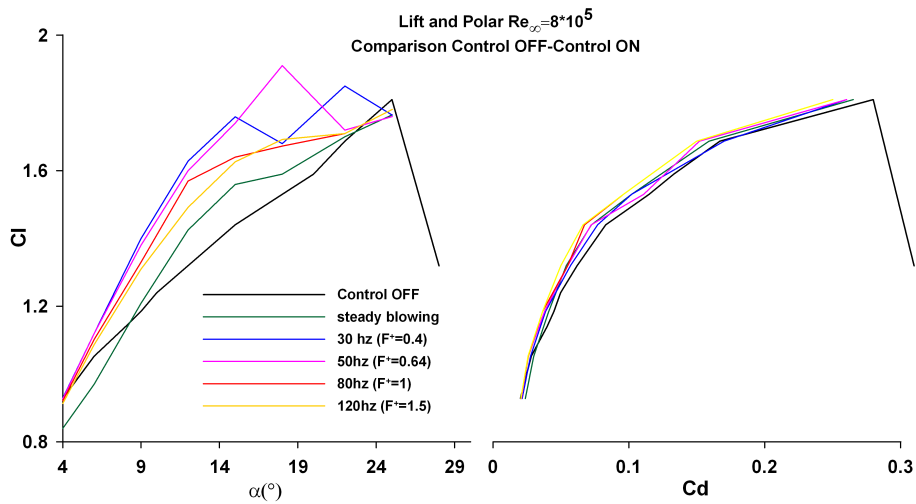
Figure 3.14: Lift coefficient and polar curves; comparison control OFF-ON

$Re_\infty=8*10^5$

Lift and Endurance variation (%) with reference to the baseline
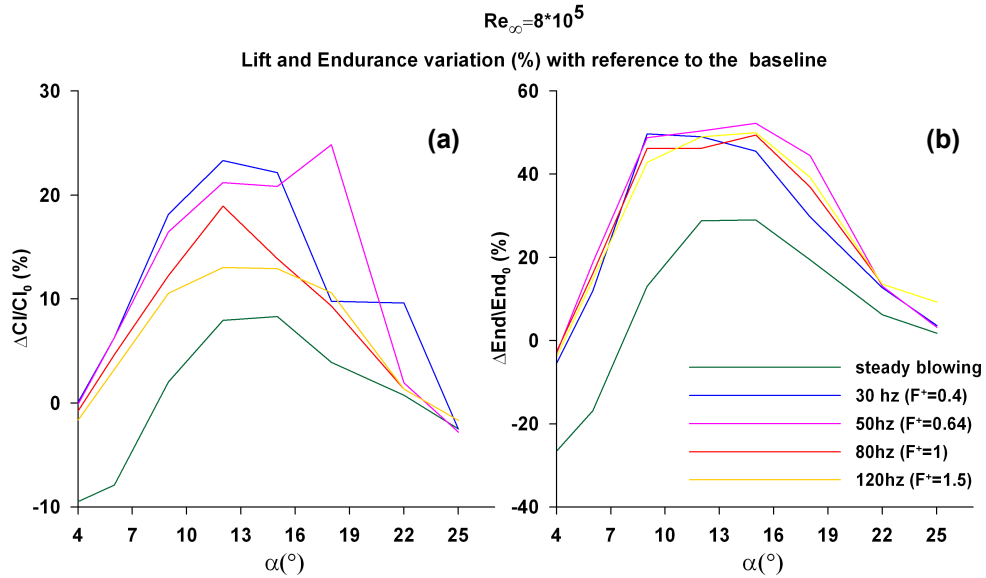
Figure 3.15a-b: Lift coefficient and endurance variation (%) with reference to the baseline (referred to control OFF)
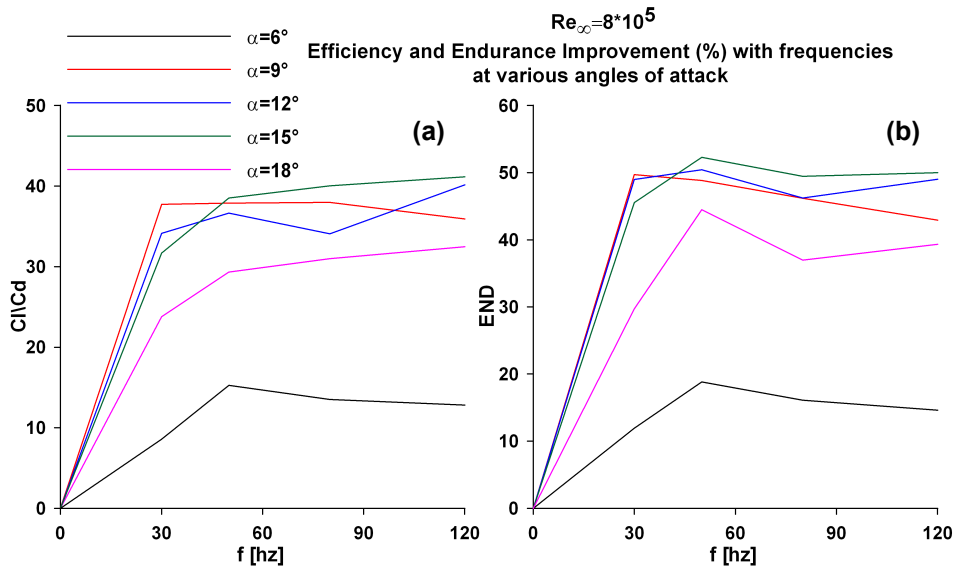
Figure 3.16a-b: Efficiency (a) and Endurance (b) improvement with frequency variation at various angles of attack

3.3.3 Control ON: Momentum Effect

The momentum coefficient has been defined in (3.2) and in this section it will be studied how the aerodynamics performance changes with varying its intensity. The analysis have been done fixing the angle of attack and the actuation frequency and varying the value of mean velocity (see (3.5)) in order to modify the momentum coefficient. Four level of mean velocity have been tested (5-10-15-25 m\s), and the lift and drag coefficient history is illustrated in figure 3.17. Also the endurance has been calculated and showed in figure 3.18 (in the table 2 the mean values of the results are summarized). The angle of attack is equal to 12° and the actuation frequency is equal to 50 Hz for all the four level of momentum coefficient.

It is possible to observe that the actuation produces lift benefit also at low intensity (C_μ=0.001) and the trend is in the direction of higher lift as the momentum coefficient rises. It is important to point out that the marginal gain decreases respect to an increase in momentum. In fact, as it is showed in figure 3.18 and in the table 2, if the momentum coefficient increases from 0.004 to 0.008 (two times) the endurance increase from 29 to 36 (+24%) and if the momentum increases from 0.004 to 0.02 (five times) the endurances increase from 29 to 51 (+75%). In the figure 3.19 the lift history is showed for α =18° and for the actuation frequency equal to 50 Hz. It is interesting to point out that the lift enhancement for the first two levels of momentum (that correspond to V_{mean} respectively equal to 5 and 10 m\s) is clearly lower than the others two levels (V_{mean} respectively equal to 15 and 25 m\s), indicating that for this angle of attack a sort of minimum ideal optimal ratio between injection velocity and free stream velocity exist and it is equal to 0.8.
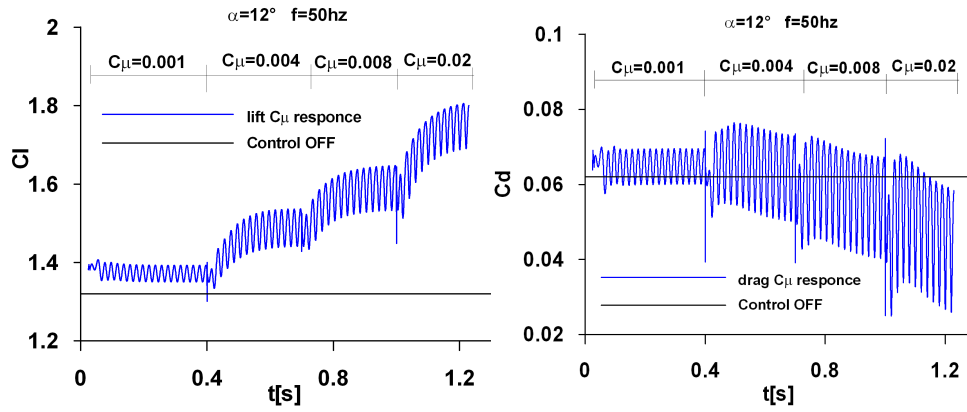
Figure 3.17: Lift and drag coefficients response with varying Cμ at α=12° and f=50Hz

Cmu	Vmean (m\s)	Cl	Cd	End
0.000	0	1.320	0.062	24.46
0.001	5	1.375	0.066	24.62
0.004	10	1.495	0.063	29.01
0.008	15	1.600	0.055	36.80
0.020	25	1.755	0.045	51.67
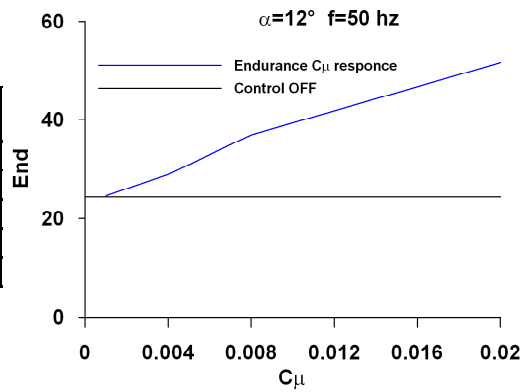
Table 2   **Figure 3.18:** Endurance at different Cμ
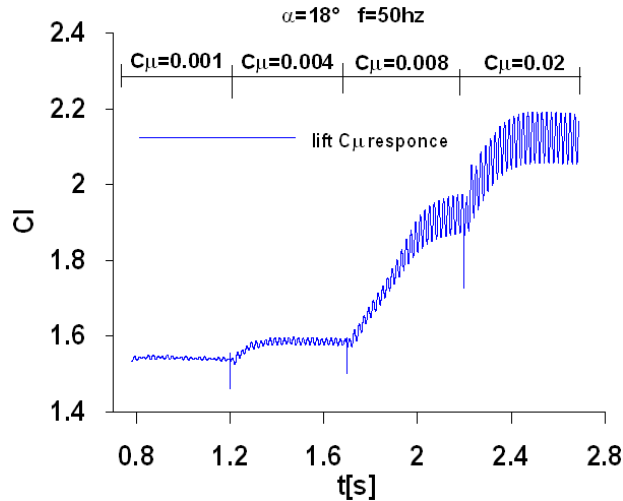
Figure 3.19: Lift coefficient response with varying Cμ at α=18° and f=50Hz

3.3.4 Control ON: Jet Angle Effect

In this section the effect of injection angle is analyzed. The injection angle is defined as the angle between the velocity and the normal to the surface boundary of slot, as indicated in figure 3.20. This analysis is important in order to understand if a small amount of injection in the direction tangential to the body surface can be useful or not in terms of lift enhancement or drag reduction. Is important to point out that also in the case treated in the previous cases the injection is not perfectly tangential to the surface since this reflects the real impossibility to create tangential blowing without modifying completely the upper surface of the airfoil. Remain to understand if this not perfectly alignment with the flow can create advantage or disadvantage in order to optimize the design of wind tunnel test.

In order to examine the influence of injection angle, the strategy followed has been to fix the configuration (angle of attack=12°) and starting from this condition five different injection angles have been tested and the momentum coefficient and reduced frequency have been fixed (f=30Hz). The results are reported in figure 3.21 where the lift and drag are illustrated in the five cases.
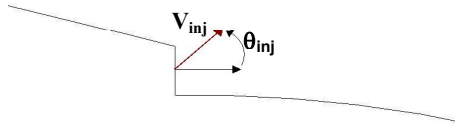
- 5 injection angles have been tested:
- θ_{inj} = 0°-5°-10°-20°-40
- angle of attack : 12°
- actuation frequency : 30 Hz

Figure 3.20: jet angle definition and test settings
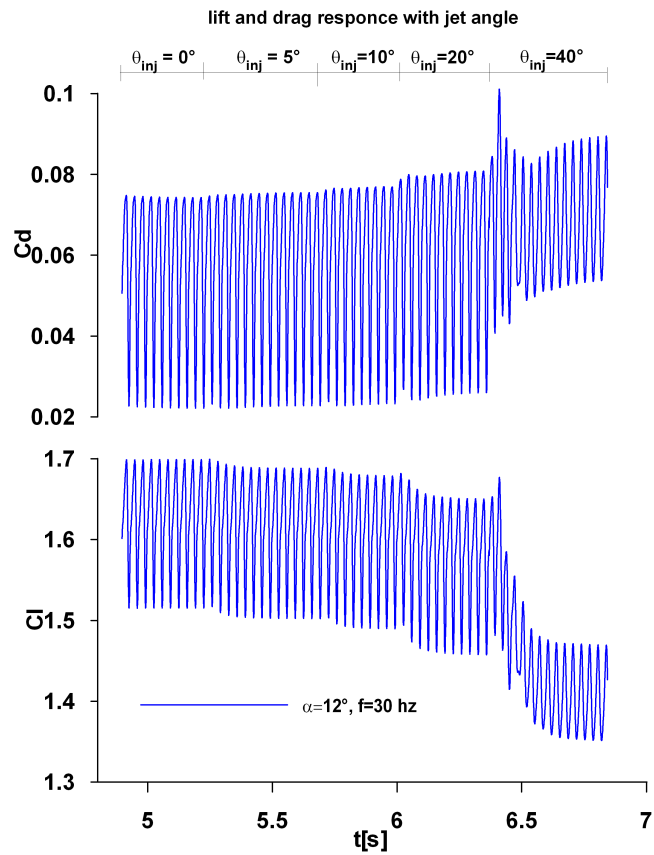
Figure 3.21: Effect of injection angles on lift and drag coefficients with fixed reduced frequency and angle of attack
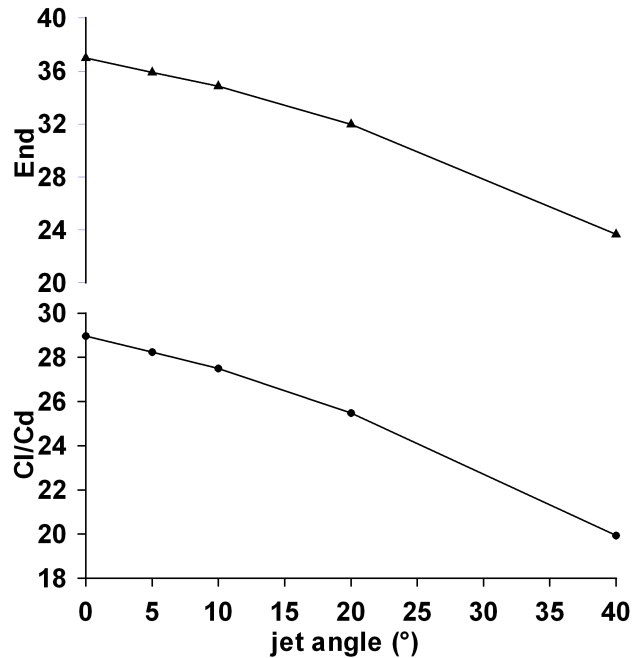
Figure 3.22: Efficiency and Endurance variation with jet angle. The values of coefficients are obtained using the mean values of lift and drag coefficients from figure 3.21

As it is possible to observe from figure 3.21 an increase of injection angle produces a progressive decreasing in lift followed by an increase in drag. In the figure 3.22 the mean values for lift and drag extrapolated from oscillating curves in figure 3.20, are used to plot efficiency and endurance with varying jet angle. As is possible to observe both the coefficient decrease as the jet angle increase, but is also important to point out that the general rate of decreasing is not constant, in particular it increases as the injection angle becomes higher than 10° (the trend is not linear). This indicates that the more suitable situation occur when injection is tangential to the airfoil surface both for lift and drag.

The information acquired in these numerical analysis have been used as general criteria to design and built the experimental model to test in the DPA wind tunnel,

as the location of slot exit for suction and blowing, the power required to operate suction, the optimal frequency for the rotating valve design and not last the orientation of slot exit for pulsed blowing. In the next chapters the experimental part will be illustrated with the small scale model design and testing and further the design and testing of full scale model.

Chapter 4

Pulsed Blowing System: Modelling and Simulation

4.1 Introduction on Oscillatory Actuators

The oscillatory actuators fall into two general classifications, zero-net-mass (synthetic jets) and pulsed blowing. Synthetic jets are self contained, with zero net mass addition to the flow, while pulsed-blowing actuators require a source of pressurized fluid, resulting in a non-zero average flow across the actuator interface (see figure 4.1).

For the unsteady blowing case, the rotating valve-tube-actuator resonant system has been considered and investigated. Particular attention has been devoted to the numerical evaluation of the influences of each element in the complete system chain to find the optimal values for the output velocity reduced frequency (14) as well as for the unsteady and steady part of momentum coefficient (15) needed to improve the aerodynamic performances. At this regard some experimental work [2],[4] has already been done for different model set-up indicating that the oscillatory flow component should promote mixing between the higher and lower momentum fluid, causing the reattachment of the flow. For flight Reynolds number of our interest and considering the separation close to 70% of the airfoil chord, the goal is to obtain output fluctuation velocity u' between 10-15 m/s with frequency f in the range 50-150 Hz. This goal can be obtained with an ad hoc designed rotating valve and with an optimal choice of tubing length, chamber volume (that in this case will be considered fixed and equal to those of suction case) and slot exit width, as fully explained in [5].
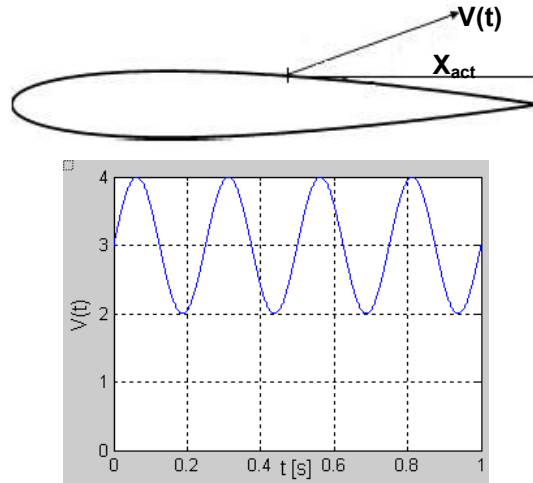
Figure 4.1: Example of output velocity for non zero mass flow injection

As mentioned in the introduction, excellent review on physics of unsteady excitation is given by [6],[7],[8]. As mentioned above the key parameters that control this mechanism are strongly dependent on reduced frequency (4.1) and momentum coefficient (4.2)

$$F^+ = \frac{f * X_{act}}{V_\infty} \tag{4.1}$$

$$C_\mu = <c_\mu> + c'_\mu = \frac{2h}{X_{act}}\left(\frac{V_{mean}}{V_\infty}\right)^2 + \frac{2h}{X_{act}}\left(\frac{V'}{V_\infty}\right)^2 \tag{4.2}$$

Seifert, Wygnanski and Tinapp [2,3,4,9] suggest that the most effective forcing frequency for flow control is $F^+\sim 1$, where X_{act} is the distance between the injection point and the model trailing edge. Shedding flow and pulsating injection interaction produce lift enhancement and a significant reduction in drag excursions by using frequencies that are comprised in range of 1-3 times of shedding frequency (which correspond as order of magnitude to our definition of $F^+\cong 0.8$). Indications of these effects were experimentally identified by Seifert [2]. Using an appropriate combination of frequency (F^+) and momentum ($<C_\mu>$) the flow should be steadier, even if it should continue to show intermittently separation. This analysis can be

useful to design the electromechanical system in order to obtain the optimal performance close to the frequency that lead to reduced frequency approximately one, once the separation point and free stream velocity have been fixed.

4.2 Pulsed Blowing: Modelling with Electro-Acoustic Analogy

Practically the pulsed blowing system can be obtained through a steady air supply modulated by rotating valve to produce unsteady excitation that is transmitted to the actuator (cavity) by transmission line (tube). The scheme is illustrated in figure 4.2.
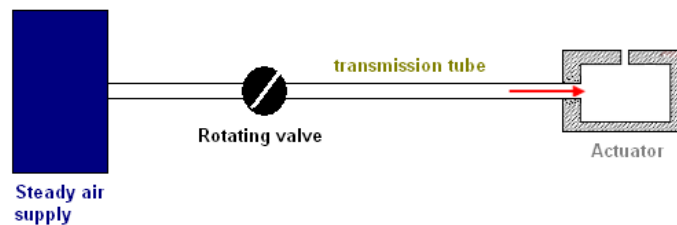
Figure 4.2: Configuration for a pulsed blowing system

The Input voltage for rotating valve (RPM) control the rotation frequency, and single valve can be designed to supply more than one actuator located inside profile.

In fact one aim is to connect a large number of internal vanes to only a few (in this case one) rotating valves. This constraint leads to a variety of different tubing lengths between the oscillating valve and internal actuators, which will produce a number of different resonant frequencies in the system. In addition, the vanes have small cut, which tend to damp oscillations. Since the main scope is to maximize the velocity fluctuation amplitude at the exit of the slot over a wide range of forcing frequencies, it is often desirable to operate the actuator at resonant conditions. The task of predicting the velocity fluctuation amplitude that will occur at the exit of an actuator for a given pressure input and oscillating valve frequency and system configuration becomes difficult. The system described can be modelled using the

approach of electro-acoustic analogy, as suggested by Mc Cormick [29], where mechanical system is substituted by equivalent electrical circuit (see figure 4.3), and the overall transfer function is studied in order to evaluate the influence of each component on exit velocity. In this analogy the motion of the fluid is equivalent to the electrical current, and the pressure difference across mechanical elements is electrically correspondent to the voltage across the corresponding part of the electric circuit. In summary, it is possible to define an overall relation between input pressure P and output flow rate Q. It can be expressed as,

P = ZQ   (4.3)

where pressure and flow rate have to be understanding as mean part plus fluctuating part and Z is the system impedance that can be obtained once the modelling of the system parameters has been done.

The idea is to design a system to have resonant condition near the frequency of our interest (100 Hz). Mainly two kind of models are used to obtain the overall system impedance, lumped and distributed models.
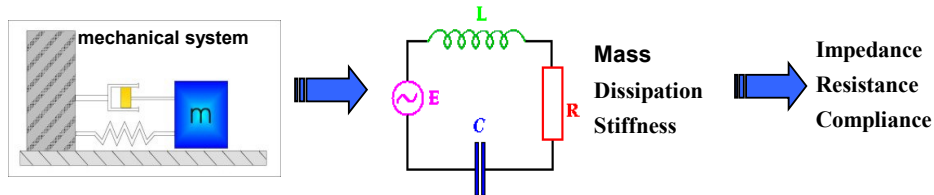
Figure 4.3: Electro acoustic analogy (from McCormick [26])

4.2.1 Lumped Element Model for Actuator

In general in the electro-acoustic analogy the parameters of the system are dependent by geometrical characteristics of the devices and by the frequency of pulsation, resulting into a set of governing partial differential equations.

In the Lumped modelling, the various energy domains of original mechanical system (inertance, dissipation and stiffness) are thought as simplified device connected to form an equivalent electrical circuit, where the single circuit elements are defined by lumping the distributed energy associated to single domains.

The requirements to use lumped model is that the characteristic length scale of the device must be small compared to the acoustic wavelength of the oscillations. With this assumption the acoustic variables are considered spatially constant so that the coordinates can be ignored in the equation of motion. As result the system of partial differential equations can be substituted into a set of coupled ordinary differential equations, and the fluctuating part of pressure and velocity are defined as follow:

$$p'(t) = \sqrt{2}|p'|e^{j\omega t} \text{ and } u'(t) = \sqrt{2}|u'|e^{j\omega t} \tag{4.4}$$

The impedance parameters for LEM (Lumped Element Model) are constituted by acoustic mass (inertance) that is the element that store kinetic energy, compliance (cavity of the actuator) that store potential energy and acoustic resistance, associated with dissipative losses in the orifice or slot cut. The complete derivation of the following results are fully explained in the work of Kim and Williams [5].

Acoustic mass *L*

Acoustic mass is defined as a mass of air accelerated by a net force, which acts to displace the gas without appreciably compressing it. This element represents stored kinetic energy. Using the assumption of fully developed laminar flow in pipe, the acoustic mass can be expressed as following:

$$L = \frac{\rho l}{A} \tag{4.5}$$

where l is the effective thickness of closing plate that is calculated as sum of real thickness (l_n) of closing plate and mass end correction thickness that depend on geometrical shape of cut. A is the area of slot exit and ρ is the gas density. If the assumption of plate area sufficiently bigger that slot area the final form of acoustic inertance is:

$$L = \frac{\rho(l_c + l_n)}{A} = \frac{\rho}{A}\left(l_n + 0.48\sqrt{A}\right) \tag{4.6}$$

Acoustic Cavity Compliance *C*

The cavity is a chamber with volume V_c that contains a gas that can stores potential energy and is modelled as an acoustic compliance. With the assumption of fluid as isentropic ideal gas and assuming the process of compression as adiabatic in frictionless flow, the acoustic compliance depend by chamber volume (V_c), gas density (ρ) and speed of sound ($\underline{c}$) as indicated in (4.7):

$$C = \frac{V_c}{\rho \underline{c}^2} \tag{4.7}$$

Acoustic resistance *R*

The acoustic resistance is associated to the losses due to the slot exit. Rigorously the acoustic resistances follow the nonlinear behaviour of the flow through an orifice or slot due to the vortex formation for oscillating flows. This should be considered for the evaluation of actuator resistance, but if the linear approximation is used and the assumption of fully developed flow in laminar pipe is assumed (Hagen-Poiseuille equations), the solution gives the acoustic resistance indicated in (4.8):

$$R = \frac{\Delta P}{Q} = \frac{8\mu l}{\pi r^4} \tag{4.8}$$

where Q is the volume flow rate produced by pressure jump ΔP, μ is the viscosity and r is the radius of the orifice. The first part of previous formula suggests also an experimental way to measure the acoustic resistance as the ratio of the mean flow rate through the slot produced by a mean pressure jump between external ambient and internal chamber.

All these parameters depend only by the geometrical characteristics of the device and they do not depend on the frequency of disturbance.

Once the parameters of the system have been defined the lumped element model for the actuator can be illustrated. The reference figure is 4.4a-b.
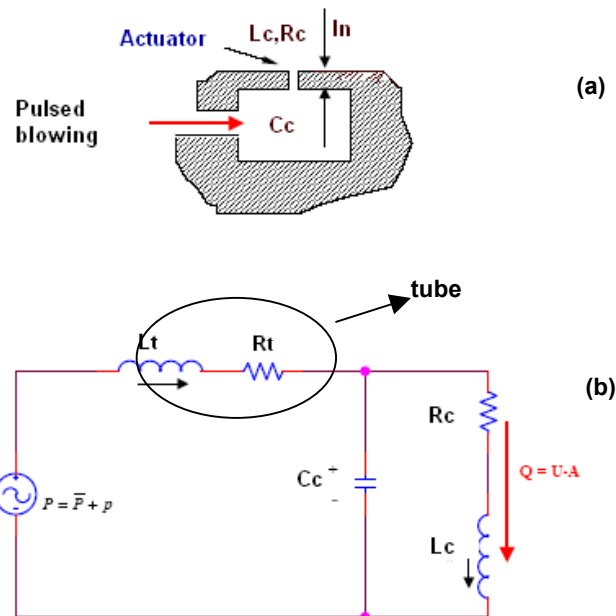
Figure 4.4a-b: Lumped model for the actuator (from Kim [5] and Karam [30])

The actuator (4.4-a) is modelled as a resistance and an impedance in parallel with a conductance (the subscript *c* stands for "chamber"), while, as anticipated, the flow rate is "equivalent" to the current that circulate in the circuit. The rest of the circuit in the figure 4.4-b with impedance and resistance L_t and R_t are the equivalent concentrated parameter for the connection tube (the subscript *t* stands for "tube") that link the actuator chamber to the rotating valve producing pulsating pressure (here presented as voltage).

In spite of the simplicity of the system illustrated in figure 4.4-b the lumped element model used for the actuator cannot be used also for the connection tube. In fact with reference to the approximation representing the basic assumptions for the use of LEM, the characteristic length of the connection tube, in this case, might not meet this condition. For situations in which the characteristic length and wavelength of sound are comparable ($l \sim \lambda$), as for tubing length of 2 m and

frequency near 100 Hz (order of magnitude of our interest), it is necessary to use a distributed model.

4.2.2 Distributed Model for Connection Tube

Contrarily to the Lumped Model in the distributed model the system's parameters are dependent both on geometrical characteristics and frequency of perturbation. The infinitesimal segments of a transmission line can be modelled with lumped elements such as L, R, C and G (conductance), and the transmission line contains infinite numbers of these lumped elements (see figure 4.5). The lumped elements are determined per unit of length and following multiple of the entire length of tube. The single parameters are evaluated solving the equations of oscillating flow in circular channel (as discussed in White 1974) in condition of incompressible and isentropic flow.
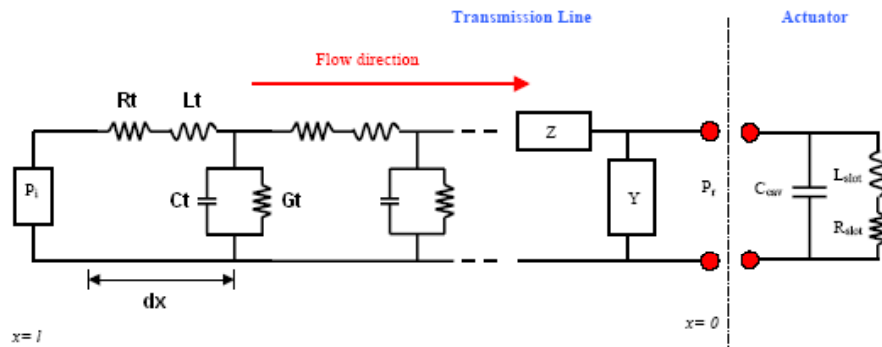
Figure 4.5: Distributed model for a tube (Kim [5] and Karam [30])

The fluctuating velocity profiles obtained for LEM (see 4.4), are substituted by the following:

$$p'(x,t) = p'(x)e^{j\omega t} \text{ and } u'(x,t) = u'(x)e^{j\omega t} \tag{4.9}$$

and the solution of momentum and energy equations leads to (considering only the first order terms, neglecting the variation of temperature, u velocity in x direction, symmetry and imagining uniform pressure in the cross section):

$$
u = f(St_v, \delta_v) = \frac{j}{\omega \rho} \frac{dp'}{dx} \left[1 - \frac{J_0\left(\frac{1}{2} \cdot \frac{2r}{\delta_v} \cdot j^{3\backslash 2}\right)}{J_0\left(\frac{1}{2} \cdot St_v \cdot j^{3\backslash 2}\right)} \right]
\tag{4.10}
$$

where St_v is the viscous Stokes number ($\sqrt{\dfrac{\omega d^2}{\nu}}$), δ_v is the viscous boundary depth

J_0 is the Bessel function of zero order and d is the diameter of circular channel.

The velocity profile is also determined by the Stokes number St_v. As it increases the thickness of Stokes zone decreases and at limit of high Stokes number, it becomes little respect to the inviscid region. An ideal division in this case exists between inviscid and viscous annular region. For the high Stokes number approximation for the velocity profile the equation for pressure and flow rate fluctuation becomes as follows (derived from momentum and energy equation after substitution of velocity profile):

$$
\frac{dp'}{dx} = (R_t + i\underline{\omega}\underline{L}_t)q'
$$
$$
\frac{dq'}{dx} = (G_t + i\underline{\omega}\underline{C}_t)p'
\tag{4.11}
$$

where the coefficient are the following:

$$
L_t = \frac{\rho}{A} \qquad\qquad C_t = \frac{A}{\gamma P_{abs}}
$$
$$
G_t = \frac{\gamma - 1}{2\sigma} C_t \sqrt{\omega \omega_v} \qquad R_t = \frac{1}{2} L_t \sqrt{\omega \omega_v} + \frac{8\pi\mu}{A^2}
\tag{4.12}
$$

Where P_{abs} is the absolute pressure, A is the area of tube section, $\underline{\omega}$ is the pulsation (2πf), ω_v is the characteristic frequency (8πν\A), γ is the ratio of specific heats.

The parameter in (4.11) are the resistance, inductance, conductance and compliance of distributed model (see 4.12), for an infinitesimal piece of tube. Some of them, as anticipated, are also frequency dependent (conductance and resistance).

4.2.3 Combined Model

The combined model is the results of using together the Lumped Element Model for modelling the dynamics of actuator and Distributed model for modelling the dynamics of connection tube. The overall scheme of the system is illustrated in figure 4.6.
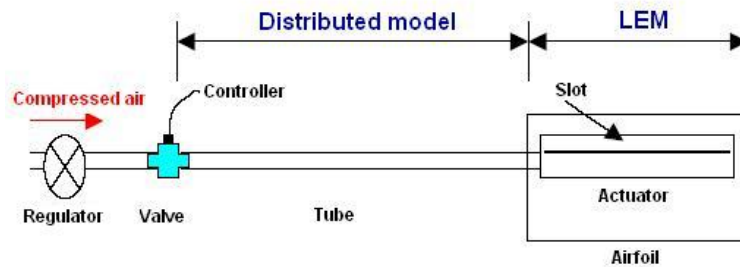
Figure 4.6: Scheme for combined model (from Kim)

The summary of the results are reported in the following formulas:

$$R_c = \frac{\overline{\overline{P}}}{Q_s} \left[\frac{Ns}{m^5}\right] \quad C_c = \frac{V_c}{\rho \underline{c}^2} \left[\frac{m^5}{N}\right], \quad L_c = \frac{\rho l}{A} \left[\frac{kg}{m^4}\right] \quad \underline{\textbf{LEM}}$$

$$L_t = \frac{\rho}{A} \qquad\qquad C_t = \frac{A}{\gamma P_{abs}}$$

$$G_t = \frac{\gamma - 1}{2\sigma} C_t \sqrt{\underline{\omega \omega_v}} \qquad R_t = \frac{1}{2} L_t \sqrt{\underline{\omega \omega_v}} + \frac{8\pi\mu}{A^2} \qquad \textbf{Distributed Model}$$

Once the coefficients are estimated (the tube is considered distributed and the correspondent coefficients have to be understanding for unit length, while the actuator is considered lumped and the relative coefficients have to be

understanding as related for the entire device), the overall transfer function of the system can be obtained. The procedure consists in the determination and assembling of impedance for each single subsystem to form the total impedance (see right part of figure 4.5) :

- Z_{act} (4.14b) is the impedance of actuator that is obtained in parallel between impedance Z_s (that is equal to the series between resistance and impedance) and impedance of compliance Z_{cc} (4.13).
- Z_{tt} (4.14a) is the impedance of transmission tube that is dependent by acoustic conductance G_t connected in parallel to the compliance C_t (resulting in the admittance Y_t) and in series with resistance and inductance of tube.

The overall impedance is illustrated in (4.15). Once it has been determined, the parametric analysis can be done to understand the influence of tubing length, slot width and chamber volume on exit velocity, in terms of transfer function module $|u'_e/p'_i|$ (Slot exit velocity fluctuation\input pressure fluctuation).

$$Z_s = R_c + (\omega * l_c) * j, Z_{cc} = 1/(\omega * C_c * j), Z_t = R_t + (\omega * L_t) * j, Y_t = G_t + (\omega * C_t) * j \quad (4.13)$$

$$Z_{tt} = \sqrt{\frac{Z_t}{Y_t}} \quad \text{impedance for the transmission tube} \quad (a)$$

$$Z_{act} = \frac{Z_s * Z_{cc}}{Z_s + Z_{cc}} \quad \text{impedance for the actuator} \quad (b)$$

$$(4.14a,b)$$

$$\frac{u'_e}{p'_i} = \frac{2.0}{\left\{ \left[e^{\left(\sqrt{Z_t * Y_t} * L_t\right)} + e^{\left(-\sqrt{Z_t * Y_t} * L_t\right)} \right] + \left[e^{\left(\sqrt{Z_t * Y_t} * L_t\right)} - e^{\left(-\sqrt{Z_t * Y_t} * L_t\right)} \right] * \frac{Z_{tt}}{Z_{act}} \right\} * a_s * Z_s} \quad (4.15)$$

(a_s is the slot area).

Figure 4.7a illustrates the result for the combined model (lumped + distributed) in the frequency range 0-1400 Hz for tubing length of 0.8 m and slot width of 1 mm and chamber volume equal to 0.00084 m^3.

Starting from this condition a parametric analysis has been done varying alternatively slot exit, chamber volume and tubing length and the results are illustrated in Figure 4.7b in the frequency range 0-500 Hz (range of our interests). As it can see from figure 4.7b, for this range of frequency the tubing length is the parameter more influencing the resonance frequencies, while slot width and cavity volume influence only excitation amplitude but not the frequencies response. For frequencies close to 100 Hz, the solution with longer tube is preferable respect to the other, as the first system resonance falls exactly very close to 100 Hz, while for the solution with shorter tube, the first peak occurs near 210 Hz.
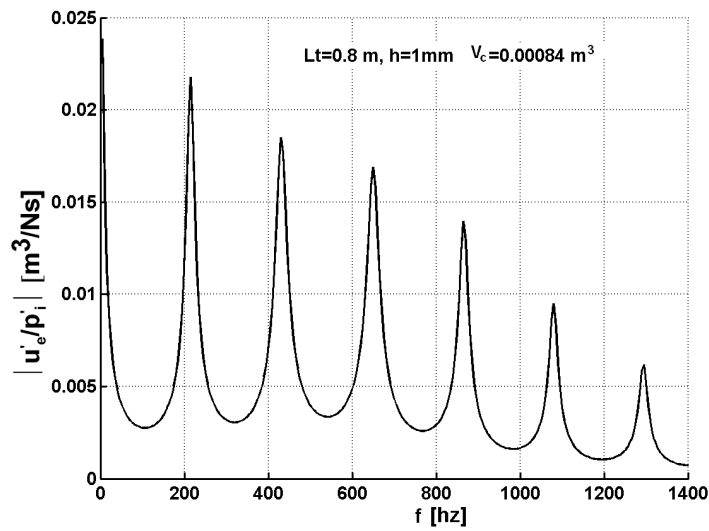
Figure 4.7a: Performance of pulsed blowing system in the range 0-1400 Hz
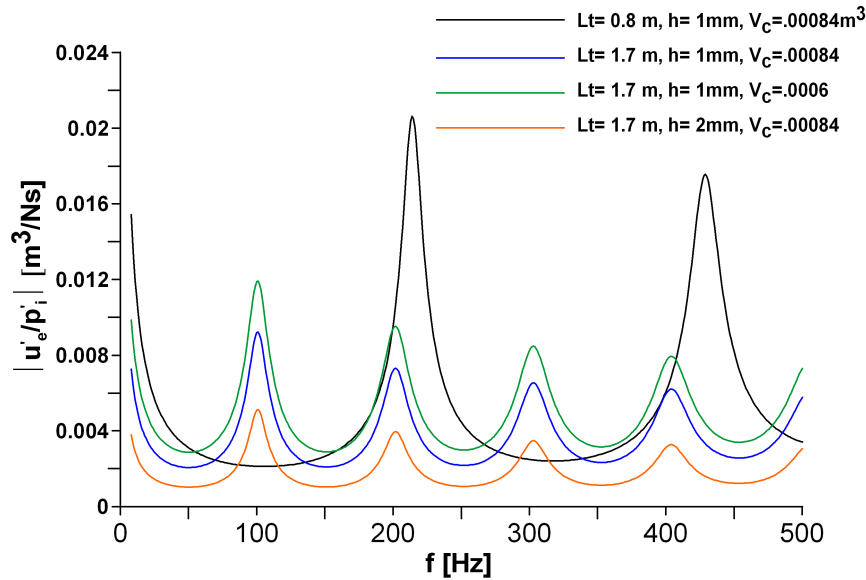
Figure 4.7b: Performance of pulsed blowing system in the range 0-500Hz

The physics of this behavior stands in the observation that lumped element modeling predicts only one resonant peak, while the distributed model predicts a number of resonant condition increasing with tubing length. The resonance of a pulsed blowing system is characterized with open-end resonance and closed-end resonance as well explained in [5]. The first peak frequency of about 200 Hz could be predicted by using a simple rule that a tube, terminating with an open end resonates when the tube length is equal to the half wavelength (or multiple) of the sound. But the prediction of the resonance characteristics for the same tubing with an actuator at the end is not predicted with the simple rule of open-end resonance, because the actuator is not completely open and the impedance of the actuator, which is the boundary condition of the transmission tubing, determines the resonance mechanism for the pulsed blowing system. It is possible to observe from figure 4.7a a little shift in resonant frequencies when the frequency rise at high values (near 800 Hz). For frequencies of our interest this shift is little and, in summary, it is possible to conclude that the resonance frequencies of the

transmission line strongly depend on the tubing length, while the geometry of actuator (slot exit, chamber volume and plate thickness) strongly affects the peak, and not the resonant frequencies.

Chapter 5

Small Scale Model: Experimental Tests

5.1 Experimental Setup

5.1.1 DPA Wind Tunnel

The Wind tunnel at the Department of Aeronautical Engineering-University of Naples Federico II, is a closed loop wind tunnel with closed test chamber Figure 5.1.
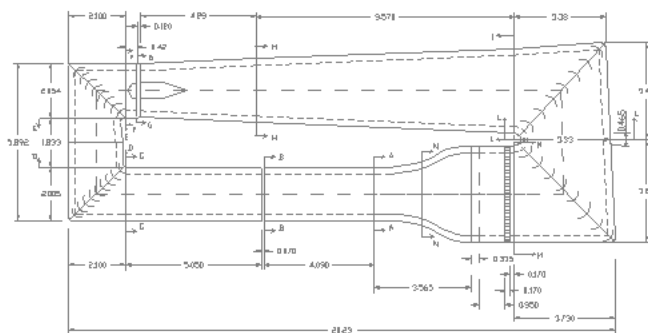
Figure 5.1: Low Speed Wind Tunnel at DPA

Test section has the following dimensions: 1.4 m height and 2 m wide. Turbulence level is about 0.1%. Maximum velocity is 45 m\s

5.1.2 Data Acquisition System

In this section a rapid survey on the instrumentation used at DPA (Dept. of Aerospace Engineering of Naples) is presented. Some of this instrumentation has been used for experiments on steady suction, while other only for unsteady blowing experiment.

For Pressure acquisition it has been used pressure data scanning model Zoc 33TCU by Scanivalve corporation. This is an electronic pressure scanner with 64 channel sensor with following characteristics:

- scan rate: from 0.01 Hz to 2000 Hz
- pressure max.: ± 20 inch H_2O
- accuracy: 0.15% FS
- required hardware: CPU PII, LAN with TCP\IP protocol

Also a multimanometer with 100 sensors has also been used (only for full span model experiment), see figure 5.2, to capture wake pressures for drag measurement and evaluation.
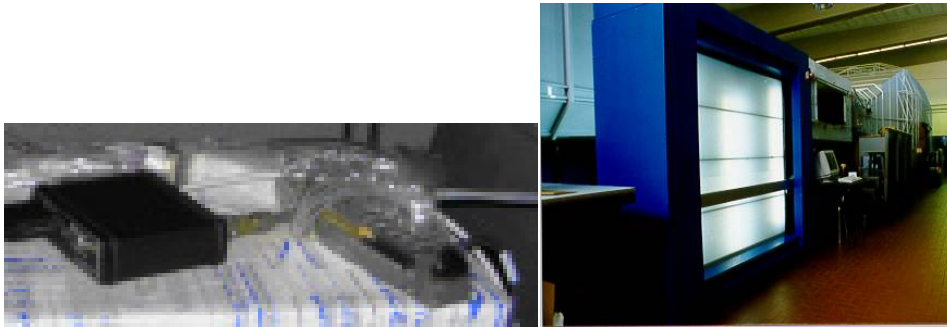
Figure 5.2: Zoc and multimanometer for pressure acquisition

For velocity measurement at slot exit (also in this case only for blowing case) a single component hot wire anemometer distributed by Dantec Dynamics has been used, calibrated in the range 0-40 m/s in the open test section wind tunnel (DPA). For data acquisition and processing Spartan device with 12 channels and sampling rate up to 10kHz has been used.

5.2 Small Scale Model: Design, Building and Wind Tunnel Arrangement

Based on the numerical tests on the best suction location, previously illustrated, the model has been set at an angle of attack such that the separation is present on

the upper surface with an extension of 30% of the chord and the suction area has been placed just upward the separation onset point. Active control on separating flow with predetermined control will be presented, and the variables that should be taken into account have been summarized in chapter 1. As it has been illustrated many aspects should be investigated, but some of them would requires more than one airfoil construction to perform this analysis, like the effect of slot exit position, or geometry of actuators. In this first work it has been decided to study the influence only of some of total number of variables: flight condition, slot shape, suction ratio and for unsteady blowing case, also frequency and momentum. The number of pressure taps on the airfoil are 41 and they have been drilled on the upper surface of the model while some pressure taps have also been placed in one of the three internal chambers, each sized 4 cm in chord, 7 cm in span and 3 cm in height. Different typologies of closing plates have been built: a porous plate with even distribution of suction points (porosity A_{Holes}/A_{Plate} equal to 0.25 with 1 mm hole diameter) and plates with a 1 mm slit cut in the middle with different angle of the flow injection direction. The plate has been installed from x/c= 0.6 to x/c=0.7. The connection air input tube (one for each chamber) has internal diameter of 10 mm. The CAD scheme and the real airfoil model are illustrated in Figure 5.3a-b (design) and 5.4a-b-c (building).
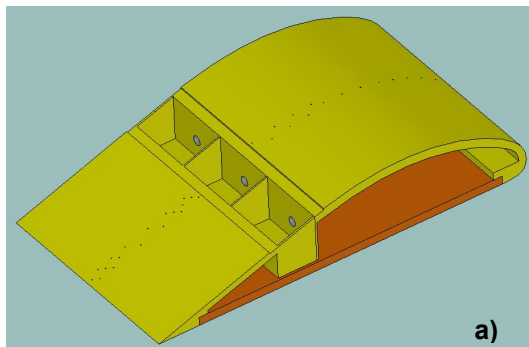
Chord: 0.4 m
Span: 0.21 m
Pressure taps: 41 (on upside)
Suction area: from 0.6 to 0.7 in chord

Figure 5.3a: Small scale model design
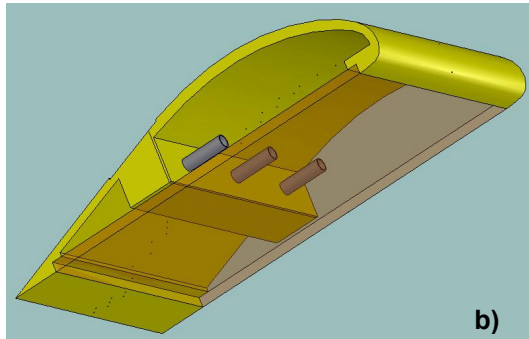
N° chamber: 3
Dimension: 7x3x4 cm
Input tube diameter: 1 cm
Lower side is removable for inspection

b)

Figure 5.3b: Small scale model design

Pressures have been acquired with Scanivalve scanner Zoc 33TCU and an off-the-shelf blowing pump has been used as air supply. To by-pass problems connected to flow meter losses (too high for the pump used), an ad hoc total and static pressure probes have been inserted in one of the connection tube for internal maximum velocity evaluation. Flow rate has been estimated using standard formulas for fully developed flows in pipes.
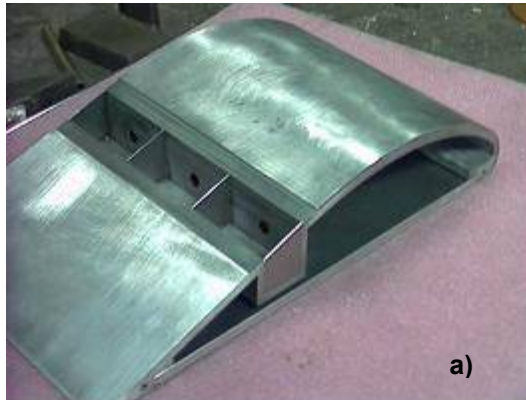
Building of the model
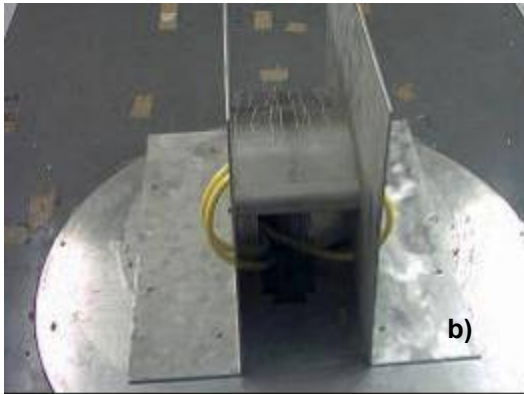
Arrangement in the wind tunnel (lateral walls to limiting the 3D effect)
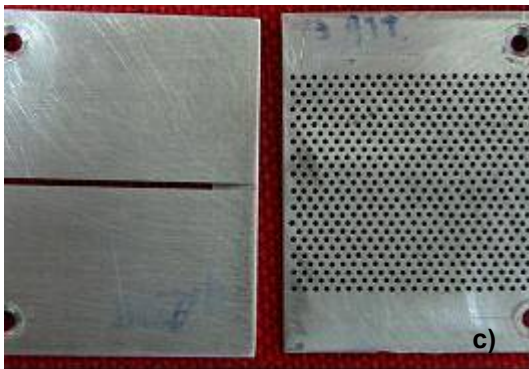
Closing plate typologies
Slot cut: 1 mm
Porous surface with porosity equal to 0.25 ($A_{holes}\backslash A_{plate}$)

Figure 5.4a,b,c: Small scale model building and closing plates

5.3 Small Scale Model Wind Tunnel Tests: Steady Suction

Figures 5.5a-b-c illustrate the results for three different angles of attack (3°, 6°, 9°), corresponding to increasing area of separation. For each of these cases the power of the pump has been varied to obtain different levels of suction intensity (measured by flow rate q from central chamber). As it can be seen in Figure 5.5a-b, suction is effective starting from 30 lt/min and the final effect is the same as for 130 lt/min. This is in agreement with numerical predictions that suggest applying suction just before separation. In fact as the angle of attack raises to 9°, the separation moves upward and suction becomes less effective, with the result that minimum value of the flow rate necessary to reattach the flow becomes much higher (90 lt/min). It is worth to point out that the Cp distribution in the separated area is not constant because in the set-up arrangement of this first small model, the airfoil is working in proximity of the tunnel floor (ground effect) thus slightly modifying the upper pressure on the rear part of the airfoil. It has not been taken particularly care about this effect as well as about the small aspect ratio of the model since the goals, for this first set of experiments, were not those of reproducing the exact two-dimensional flow in free stream air: this is left for the full span 2D model. The estimation of separation point when suction is not applied has been made using film oil and wool tufts techniques. In Figure 5.6, the comparison between distributed suction applied for the porous plate and for slot (the exit flow is normal to the surface) has been reported. Even though the effect on Cp distribution seems to be the same both for the slot and for the porous plate (with fixed flow rate), in the first case the jump in pressure between the chamber equipped with slot plate and the external flow is double respect to the porous surface: this will lead to higher required power to operate the suction. The suction is then more effective when it is distributed.

The problems connected with low aspect ratio of small scale model has suggested to pass directly on full scale model for testing the pulsed blowing control. This is due also to the presence of lateral walls in the small scale model that could create

too much disturb to the interaction process between shedding, wake and oscillatory blowing, as mentioned in the introduction. In fact, even if the lateral walls helps to create pseudo bidimensional flow, contemporary they produce the growth of boundary layer starting from upstream of model, and if the alignment with the flow is not "perfect" a shear layer detach from its surface and interact with injected flow control, yielding difficult the analysis of results.
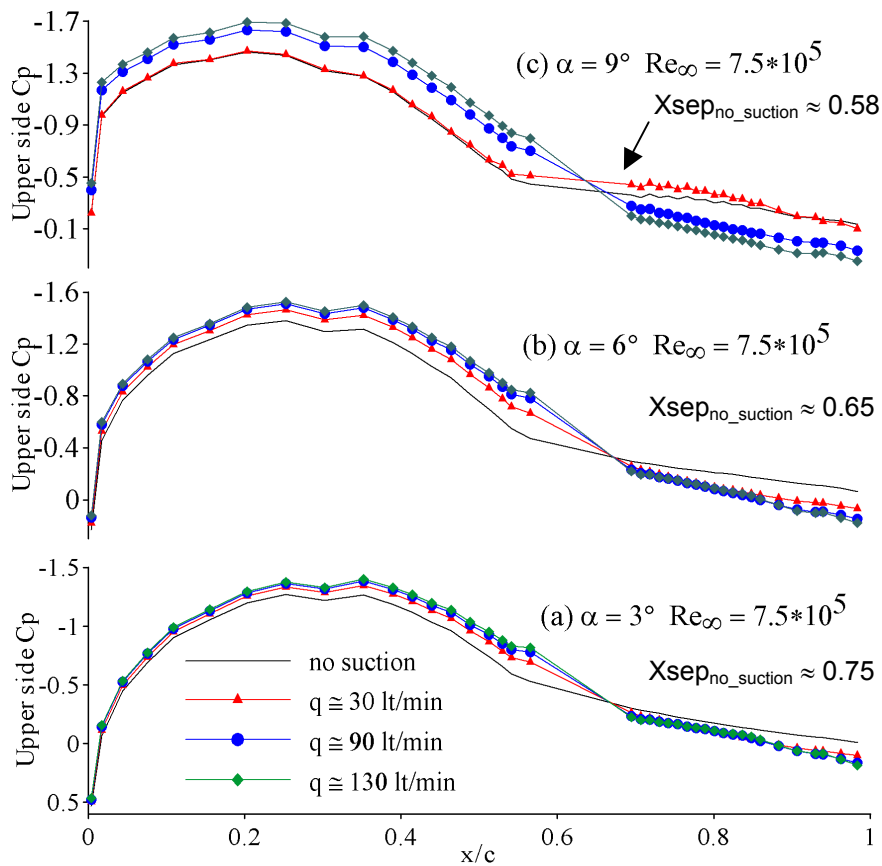
Figure 5.5: Experimental result for steady suction
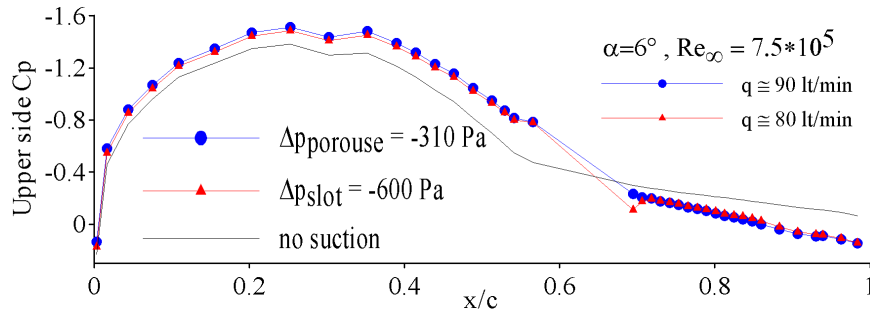
Figure 5.6: Steady suction comparison for slot and porous surface, α=6°

5.4 Rotating Valve Design & Setup Arrangement

The rotating valve has been designed and built (see Figure 5.7 and 5.8). It is characterized by 12 output holes with internal diameter of 10 mm distributed on three rings and 4 input holes with internal diameter of 14 mm. The valve has been designed to guarantee continuous flow rate and it should rotate at about 1500 rpm leading to a frequency of the output velocity fluctuation of 100 Hz. For small scale model with only 3 chambers, 3 outputs have been used, leaving the other outputs for the full scale model test.

The pulsed blowing scheme is illustrated in figure 5.9, where an intermediate tank between compressor and rotating valve has been added to kill any eventual fluctuating air component ensuring steady air supply (0-4 bar). The aims are twofold: to reduce fluctuations due to compressed air and to measure pressure directly inside the tank through pressure taps.

Velocity measurements have been done through a Mini CTA single component hot wire anemometer model 55P16 produced by Dantec Dynamics, while data acquisition and processing have been performed using the Spartan device with 12 channels at 16 bits and sampling rate up to 10 kHz. The pressure has been measured utilizing DPA Multi Manometer and unsteady pressure scanner with 64 channels by Scanivalve Corporation.

- 4 input with diameter of 14 mm
- 12 output distributed on 3 section with diameter of 10 mm

Input hole 14 mm

output hole 10 mm

Section
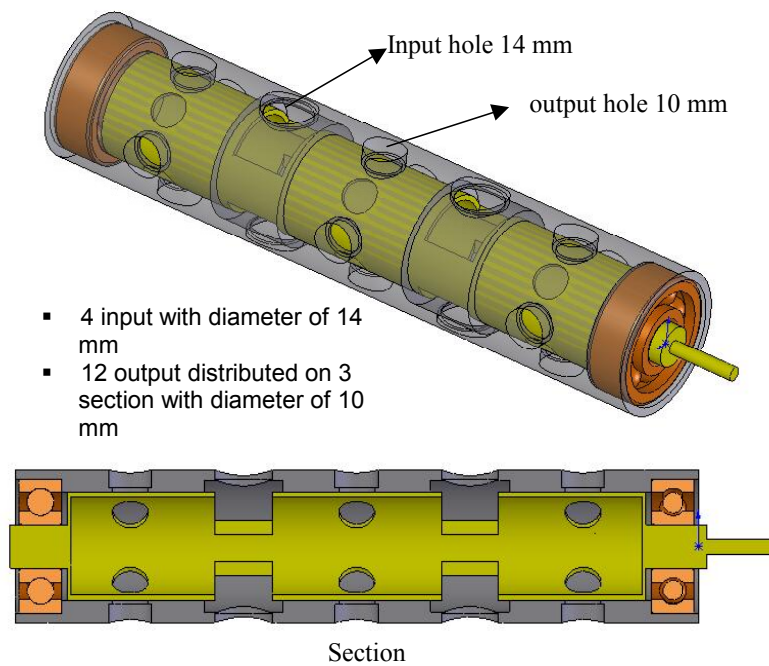
Figure 5.7: Rotating valve design

Lenght 190 mm

Figure 5.8: Rotating valve realization
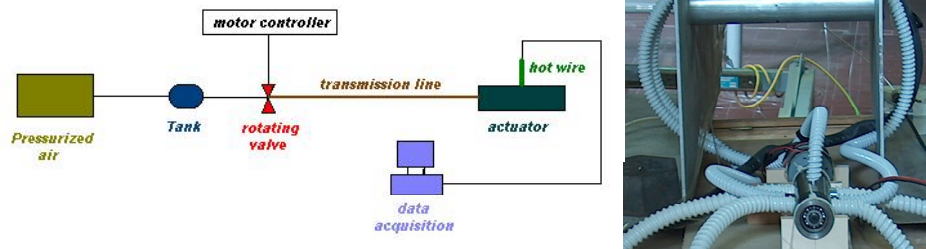
Figure 5.9: Pulsed blowing scheme and particular of valve-tube-actuator system

5.4.1 Experimental Characterization of Pulsed Blowing Actuator

Preliminary tests on open valve with no connection tube are illustrated in figure 5.10. The valve exit velocity for RPM equal to 750 and 1500 correspond respectively to 50 and 100 Hz as the theory predicts for only one opening. In the second figure, other two curves are added, for the condition of two and 3 openings. The results obtained, reflect the expectations: in fact considering more than one output opened, the peak is lower but the frequency is conserved.
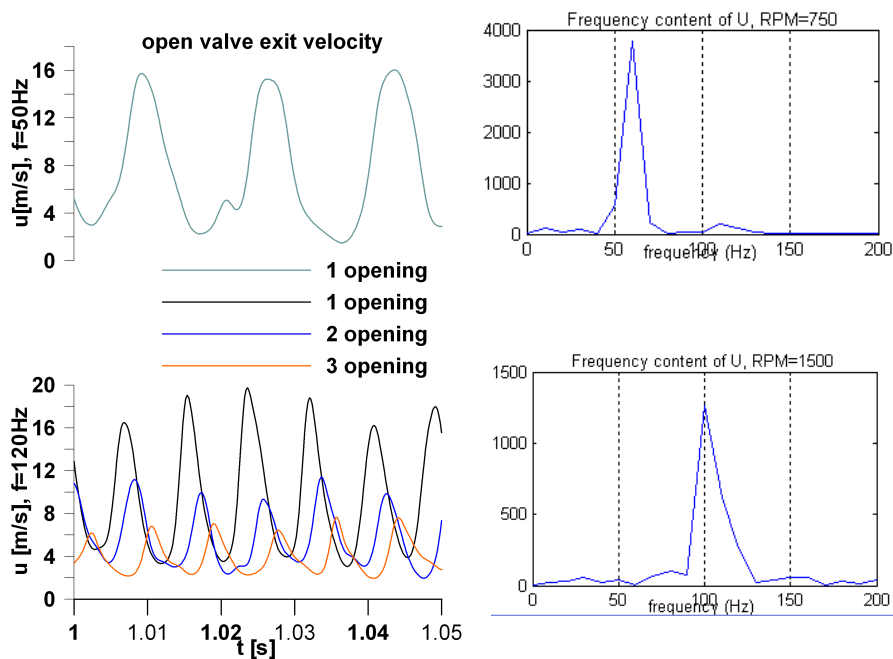
Figure 5.10: Open valve tests

In the figure 5.11 the valve-tube-actuator characterization for closing plate type 2 is illustrated, where the actuator output velocity has been reported together with mean value in the frequency range 30-133 Hz for two different values of tubing length and pressure. As it can be observed, the response depends strongly on excitation frequency, and the resonance condition changes with tubing length, while it remains substantially unchanged with pressure, and even if in certain areas mean value is unchanged, the fluctuating velocity is different. As showed by numerical calculations the system performance with tubing length of 1.6 m is better than the one with tubing length less then 1.6 m when the frequency is near 100 Hz.
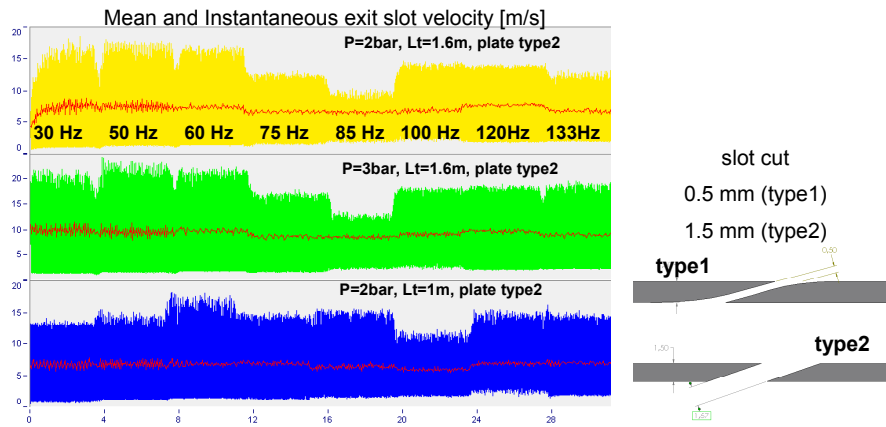
Figure 5.11: Valve-tube-actuator characterization

Comparisons between closing plates type 1 and 2 are illustrated on the following. In figure 5.12 output velocities are reported for fixed pressure in the tank (11 cm H2O) and tubing length (1 m), while in figure 5.13 the standard deviation of velocity is reported. This can be considered as an index on how the energy of the signal is distributed between the mean and the fluctuating part. The sampling rate for the acquisition is 5 kHz.

As the figure 5.12 shows, closing plates of type 1 and 2 seem to be similar in terms of resonance conditions for the overall system, but the output velocity distribution is strongly different. In fact, for plate type 1 the fluctuating part is much higher than the mean value (for f=100 Hz V_{mean} » 5 m\s and V_{max} » 15 m\s), in comparison with plate type 2 (for f=100 Hz V_{mean} » 9 m\s and V_{max} » 15 m\s).

In addition, the fluctuation for plate type 1 is higher than type 2, but the standard deviation for type 2 is higher than that relative to the type 1 suggesting that the energy of fluctuating part added to the flow is always higher for closing plate 2. This depends on the exit velocity profile that is reported for different frequencies in the figure 5.14-17. Exit velocity for plate 1 is more similar to Dirac function, and it remains unchanged with frequency, while for plate type 2 the exit velocity is more similar to sine function, but the form does not remain constant with frequency, showing the appearance of some disturbances (see the case of 140 Hz).

SR=5kHz; ΔP_{TANK} = 11 cm H2O; L_{tube} = 1.0 m
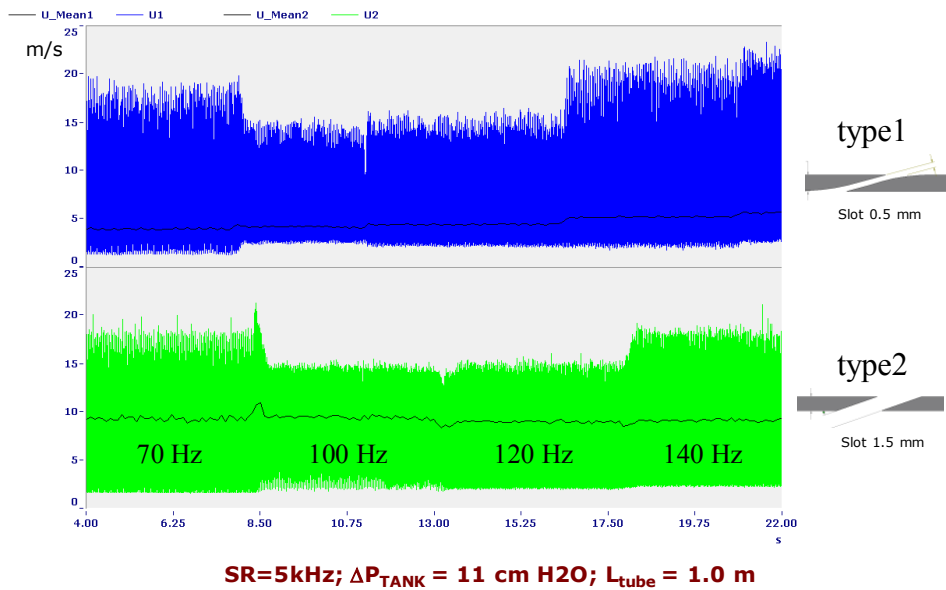
Figure 5.12: Exit slot velocity with two different plate
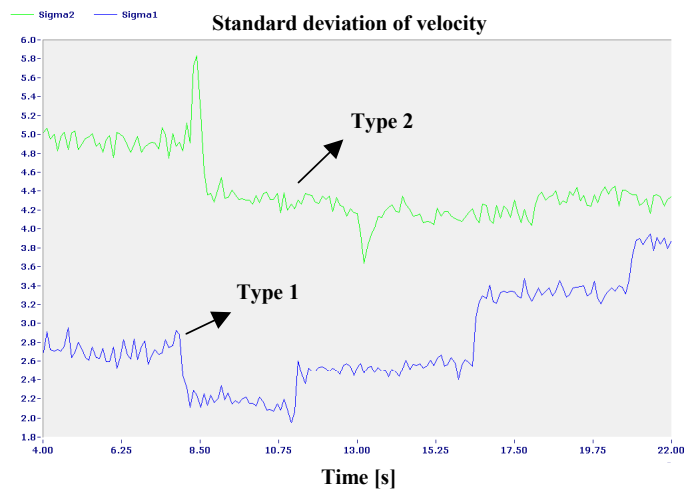
Figure 5.13: Standard deviation of velocity signal

Despite of the fact that the exit slot velocity profile for closing plate type 2 (sine function) is more suitable than that obtained with closing plate type 1 (Dirac function), for the first test in the wind tunnel it has been decided to use closing

plate type 1, as the response in terms of exit velocity profile seems to be more stable in the frequency range of our interest.
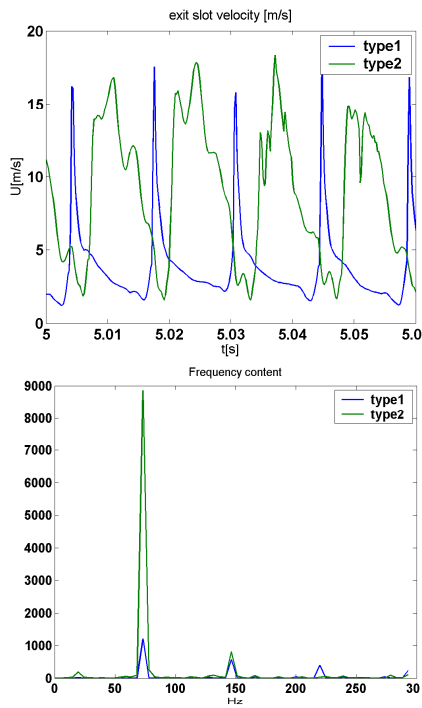
Figure 5.14: Exit velocity at 70 Hz   **Figure 5.15:** Exit velocity at 100 Hz
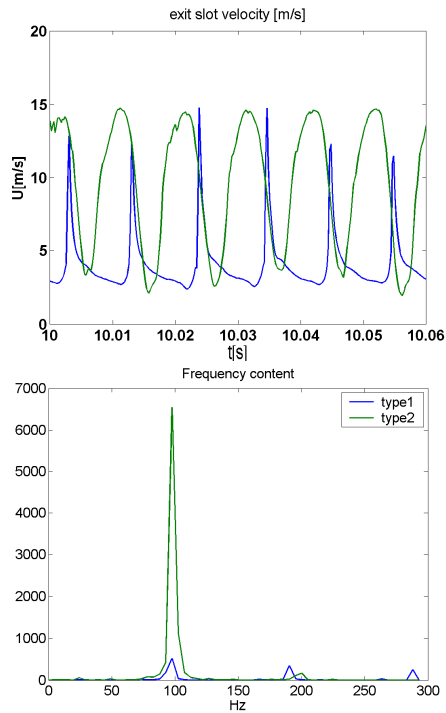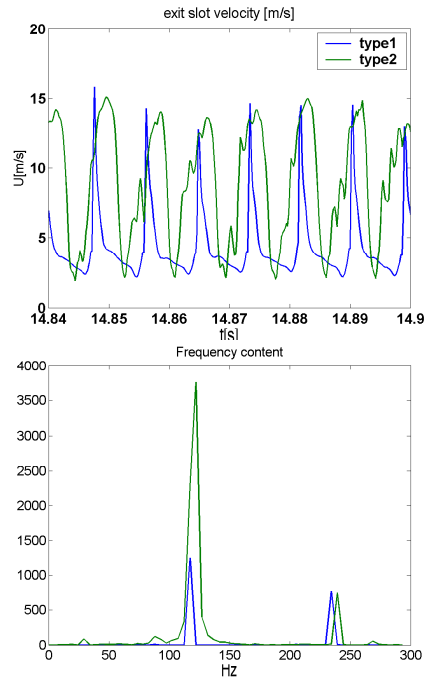
Figure 5.16: Exit velocity at 120 Hz   **Figure 5.17:** Exit velocity at 140 Hz
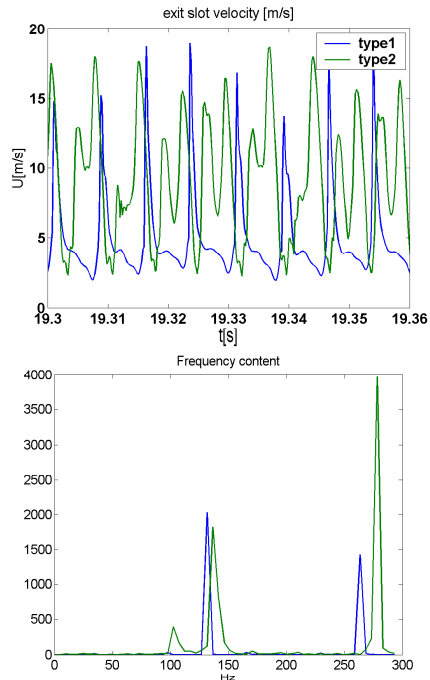
5.4.2 Small Scale Model Wind Tunnel Tests: Blowing

In figure 5.18 pressure distribution on the upside of the model is reported for three different free stream Reynolds numbers (370000-530000-700000) and for two conditions: no actuation (black line) and valve frequency rotation equal to 75 Hz (red line). In all cases, the pressure in the tank is equal to 20 cm H2O, and the tube length is equal to 1.6 m. As it can be observed the actuation becomes less effective when Reynolds number becomes too high (700000). In this condition, in fact, the ratio $V_{inj}\backslash U_\infty$ is too low to produce positive effect, suggesting that the strength of the injected flow is also important as well as the frequencies of injected flow. The influence of the valve rotation and frequency of rotation are reported in figure 5.19 and 5.20. Figure 5.19 illustrates how starting from condition of no control (black line) correspondent to not blowing case, it is possible to improve

performances adding a steady blowing (blue line, 0 Hz and Ptank=15 cm H2O) or pulsed blowing with frequency equal to 75 Hz. The pressure in the tank between compressor and valve has been kept the same for both cases.
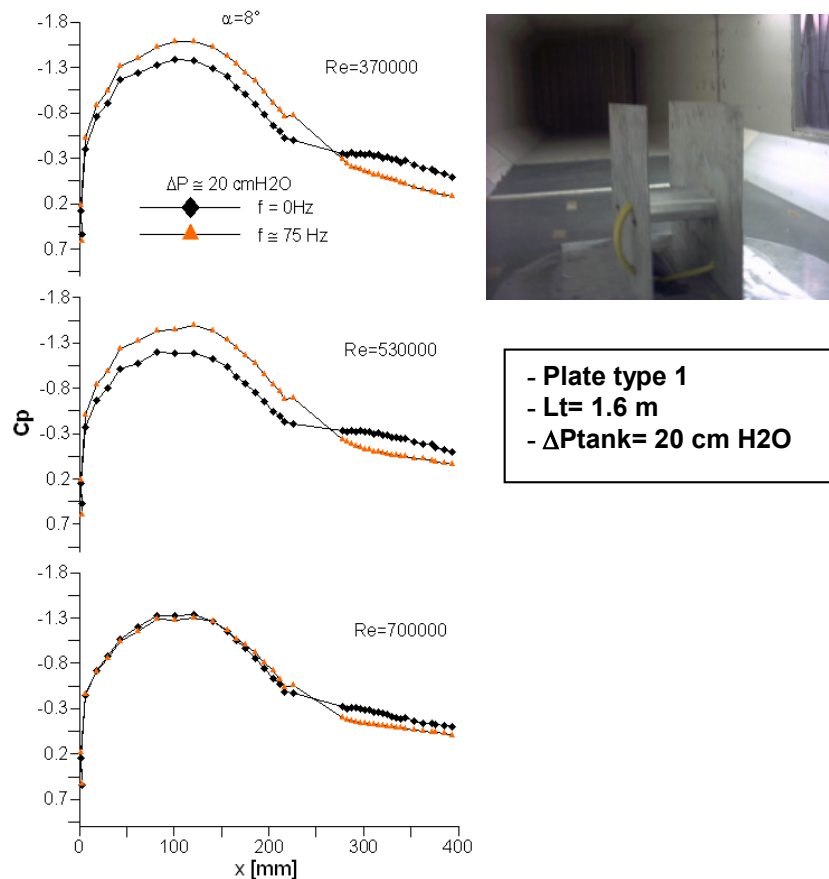
Figure 5.18: Upside pressure distribution for three different Re_∞

The two curves seem to collapse, suggesting that steady and pulsed blowing produce similar effects, but in the case of pulsed blowing the exit velocity is approximately 30 m\s, while with steady blowing the mean velocity is » 5 m\s. This means that the injected mass flow could be reduced by using unsteady injection rather than steady injection. In fact, keeping the same pressure in the compressor

for the case with 75 Hz of rotation and the case with steady blowing, the results is clearly better for the case with rotation (red line with "plus" symbols) than that with steady blowing. This comparison between steady and unsteady cases suggests that the power consumption is lower when unsteady actuation is applied. Figure 5.20 shows the results for different frequencies once the tank pressure has been fixed. The results seem to be similar to those with no control (no blowing), and the effect of the frequency is not evident. In fact, the other curves (blue-red-green) produce the same pressure distributions, in contrast to the expectations. One of the possible reasons of these discrepancies is that the flow field is strongly affected by the three-dimensional effects (low span and lateral plates) that can slightly modify the physical behaviour of the system.
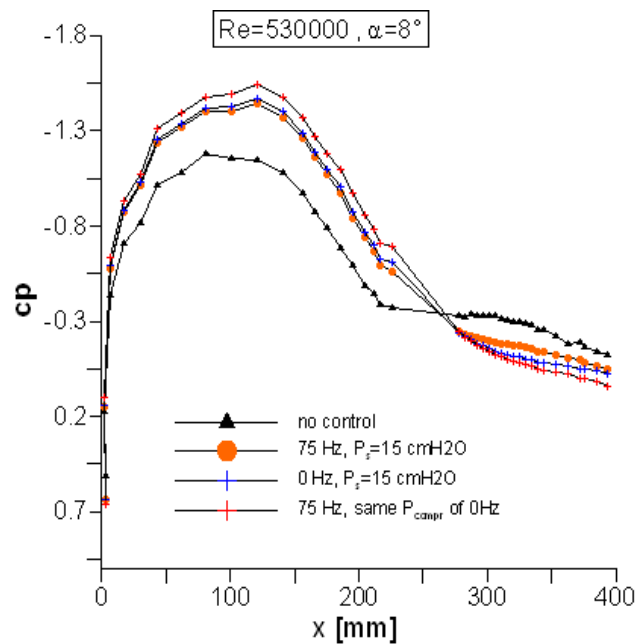
Figure 5.19: Influence of valve rotation
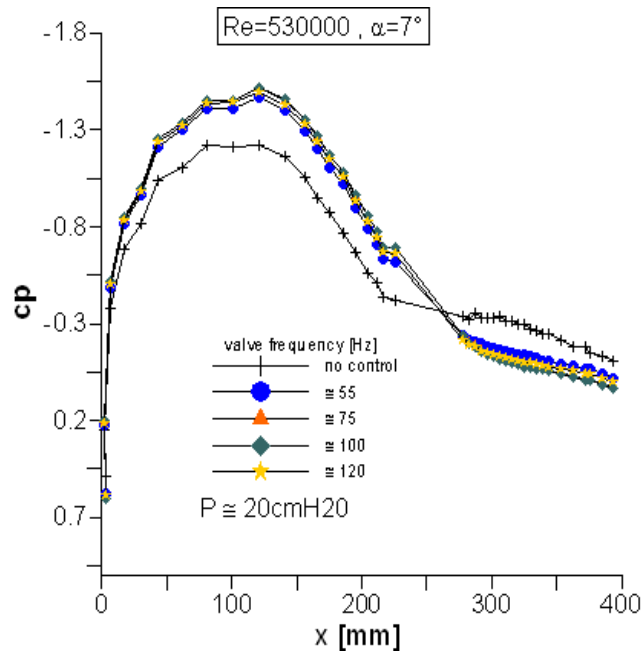
Figure 5.20: Influence of frequency

The aerodynamic effects produced by excitation control may interact strongly with the effects due to the reduced span. Another argument to be taken into account is that the exit velocity profile produced by tested closing plate is similar to a Dirac function and not to a sine function. For this reason, for the next future experiment on the full-scale model it will be designed an ad hoc actuation system in order to obtain sine function in the overall range of our interest (50-150 Hz).

This preliminary wind tunnel experiments performed on a small scale model, has showed that the excitation reduces the power spent to re-attach the flow, but the frequency resonance affect actually seems to be not clearly evident, due to some aerodynamic interferences and to the closing plate chosen for the experiments. The information acquired with these preliminary tests on small scale model will be used in the final phase of this work in order to optimize the design and tests of unsteady blowing on full scale model.

Chapter 6

Full Scale Model: Experimental Tests

6.1 Introduction

As for the experimental tests on small scale model many aspects should be investigated, but some of them would requires more than one airfoil construction to perform this analysis, so also for the full scale model it has been decided to study the influence only of some of total number of variables (Reynolds number and injected flow frequencies and momentum), remanding to one of future work the studies on influence of different actuator geometry and position.

6.2 Full Scale Model Design, Building and Setup Arrangement

For the 3D full scale model tests, it has been used the airfoil profile illustrated in figure 6.1, designed by CIRA researchers. The airfoil has 0.60 m in chord and a maximum thickness about 20% located at 40% in chord and is 1.40 m in span. On this baseline profile an interchangeable part with blowing actuator has been designed, see figure 6.2 and 6.3. This part has been thought interchangeable in order to be able in the next future to try different actuators geometries on the same model. The actuators has 3 main components, internal chamber, closing plate and slot. The entire span is divided in 12 internal cylindrical chambers each one of 0.115 m (in span) with radius of 13 mm (see figure 6.4). The exit slot is located approximately at 60% in chord, with cut width of 0.8 mm. The closing plate with slot cut has thickness about 3.5 mm (yellow part in figure 6.2-4). Each chamber is connected with rotating valve through input "*tube*" with internal diameter of 10 mm (figure 6.4) and distribution line (connection tube) 2.0 m long that connect chambers with rotary valve. The building of the model is illustrated in figure 6.5, 6.6a-b, with some details (main part of model and interchangeable part with

actuators) in figure 6.7. Mounted model with connection tube is illustrated in figure 6.6b where is possible to see the red plate that separate internal chamber from each other, and in figure 6.7 particulars of closing plate and slot exit profile are illustrated.
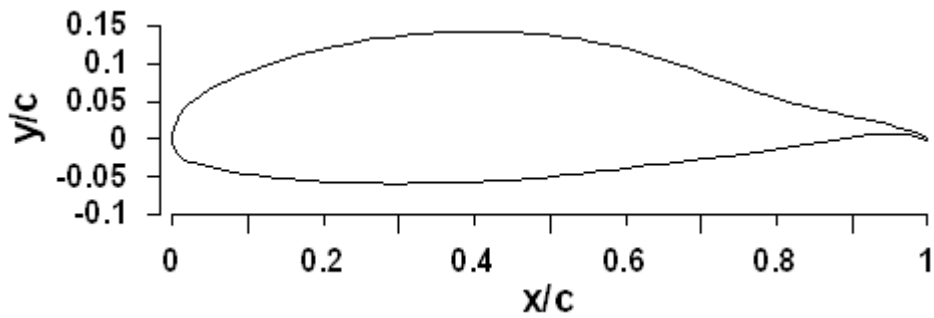
Figure 6.1: CIRA airfoil profile
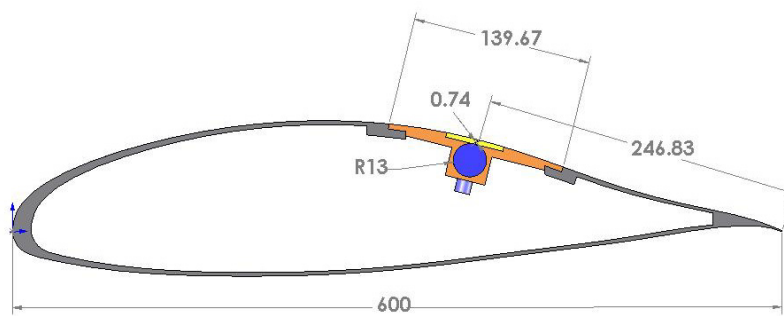
Figure 6.2: Cad model for the chambers (measures in mm)
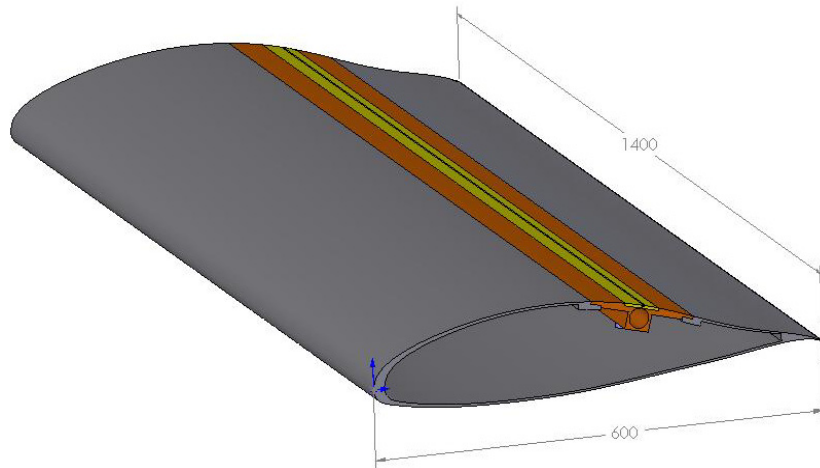
Figure 6.3: Full scale model design (measures in mm)
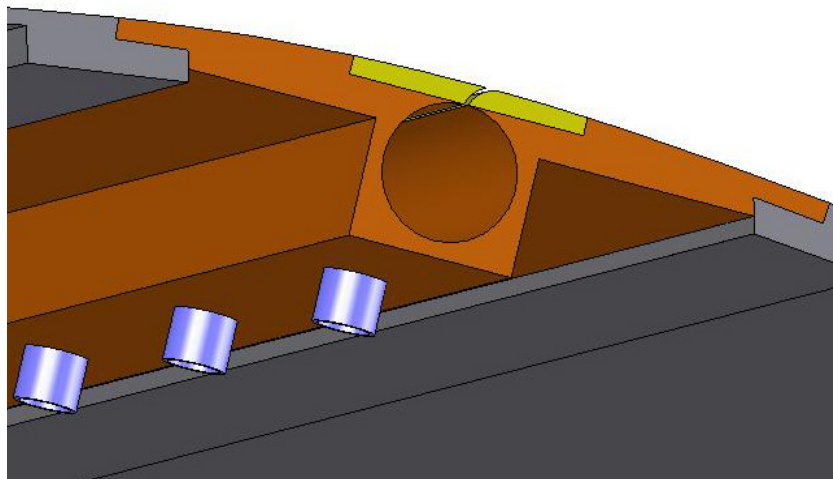
Figure 6.4: Cad particular of actuator

Figure 6.5: Building of the model, main part and movable part with chambers

(a)
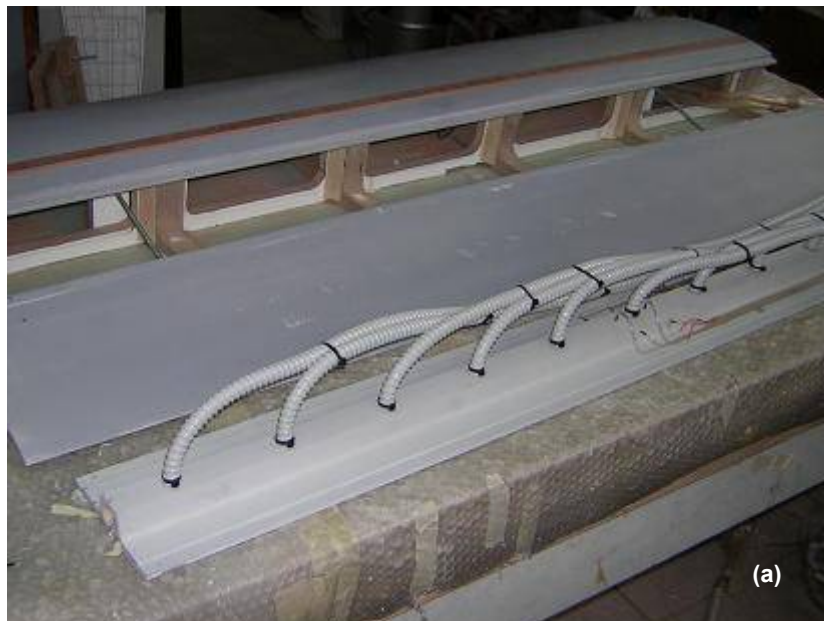
Figure 6.6a: Interchangeable part with tubing

Figure 6.6b: Complete model with tubing

Figure 6.7: Particular on actuator
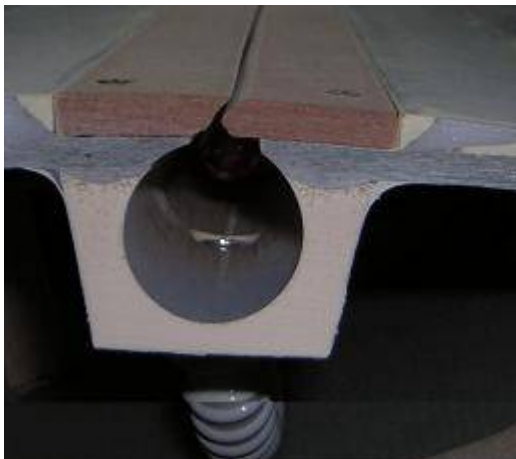
Slot
widht: 0.8 mm
position: 60% from leading edge
Jet angle: ≈ 20° (respect airfoil upside)
Chamber
shape: cylindrical
dimension: section diameter 26mm
 volume: 6.1×10^{-5} m^2

The model has been set in the wind tunnel as showed in figure 6.8a, and in figure 6.8b the particular of the actuation system is illustrated, along with rotating valve driven by DC motor and connection tube between valve and internal chambers. Model dimensions are 1.40 m in span and 0.60 m in chord, and 54 pressure taps has been distributed along the mid section at 0.70 m in span (2d condition) as illustrated in figure 6.9. Some other pressure taps have been positioned inside central chamber in order to monitoring the mean pressure distribution when actuation is applied (figure 6.10).

The drag has been measured through the wake rake with 89 pressure taps connected with DPA multimanometer, and the pressure on the model has been acquired with an electronic unsteady pressure scanner produced by *Scanivalve Corporation* with 64 channel also used for small scale model tests. The accuracy of multimanometer is about 1.5 Pascals, while the electronic transducers have an accuracy of about 2 Pascals.

Figure 6.8a: Model setup in the wind tunnel   **Figure 6.8b:** Rotary valve
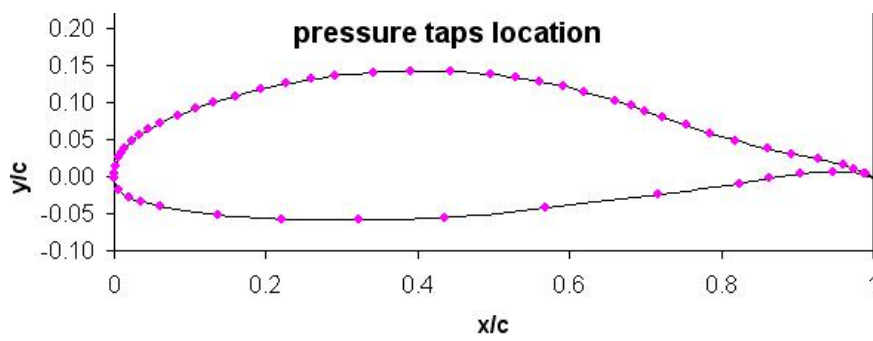
Figure 6.9: Pressure taps on the airfoil

Figure 6.10: Particular on pressure taps in the chamber

6.3 Experimental Characterization of Pulsed Blowing Actuator

Preliminary tests have been made to investigate exit slot velocity for different valve rotation frequencies (input voltage of the motor that driven the valve). The necessary inlet pressure jump is obtained with a blower and the valve is driven by standard DC motor in the range 0-12 volt that correspond to 0-120 Hz of rotation rate. The exit velocity is acquired by single component hot wire anemometer connected wit Spartan device for data sampling and processing (sampling rate of 5000Hz). The exit slot velocities are referred to the chamber near the mid span of the airfoil (0.70 m), where also the pressure taps for pressure measurement are located (figure 6.11)
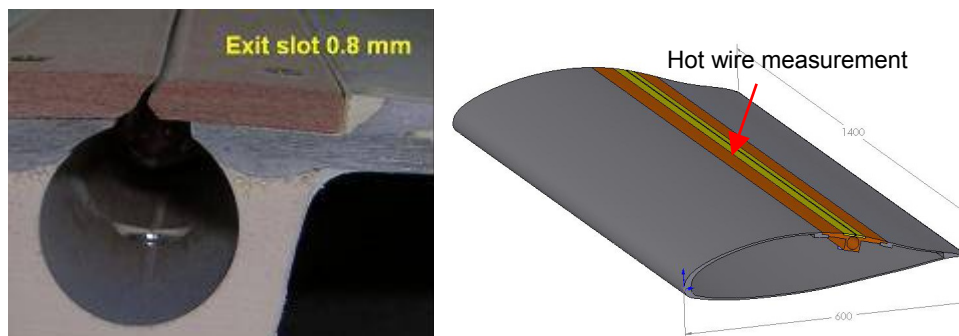
Figure 6.11: Exit slot and hot wire position

An example of exit slot velocity in the range 3-9 volt (equal to 40-120Hz) is reported in figure 6.12. As in the preliminary analysis on small scale model, also with full scale model the effect of distributed system is to produce different excitation varying the frequencies. The figure 6.12 shows exit velocities without any post processing (black line) and mean value (red line) and standard deviation (blue line). Standard deviation gives an idea on behaviour of fluctuating part. From the analysis of results it is possible to point out how the system works better for low and high frequencies, while in correspondence of input voltage of 7 volt (equal to 90 Hz) the system shows less amplitude in mean value and fluctuation together with worse velocity shape than the other two. In terms of reduced frequency F^+ the range considered is equal to 0-1.5, where for the computation of reduced frequency the reference length is the distance between exit slot and trailing edge (0.23 m) and the reference for velocity is the free stream velocity ($Re_\infty = 8x10^5$ means V_∞=18.6 m/s). In the figure 6.13a-b-c the velocity and Fourier analysis for input voltage 5, 7 and 9 volt are reported.
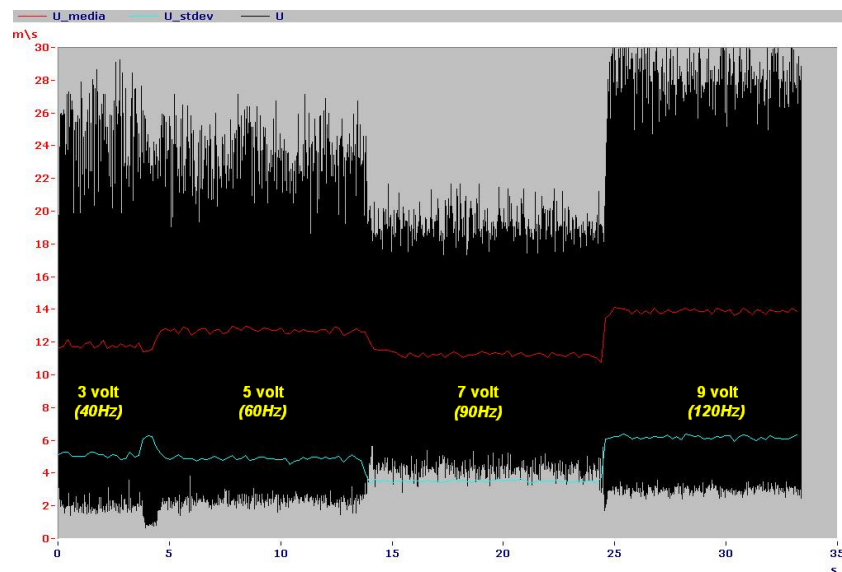
Figure 6.12: Exit slot instantaneous velocity, mean and standard deviation
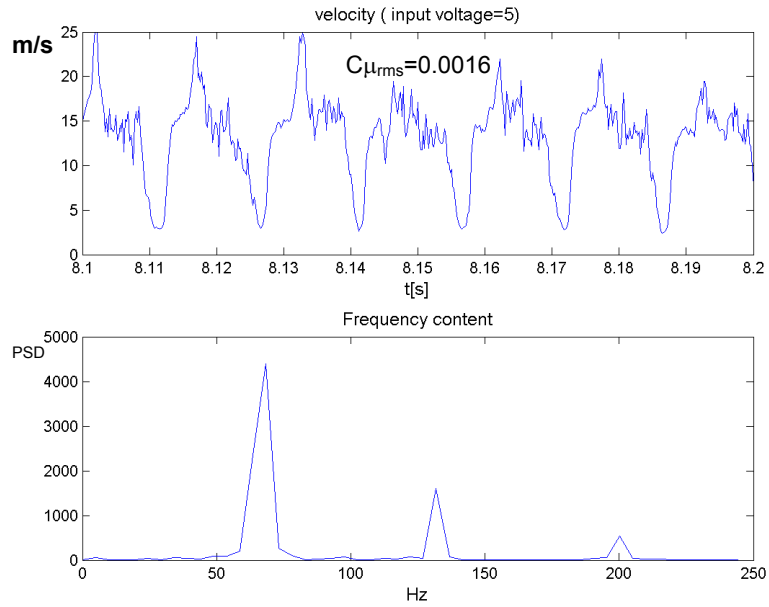
Figure 6.13a: Exit slot velocity and FFT at input voltage 5 volt
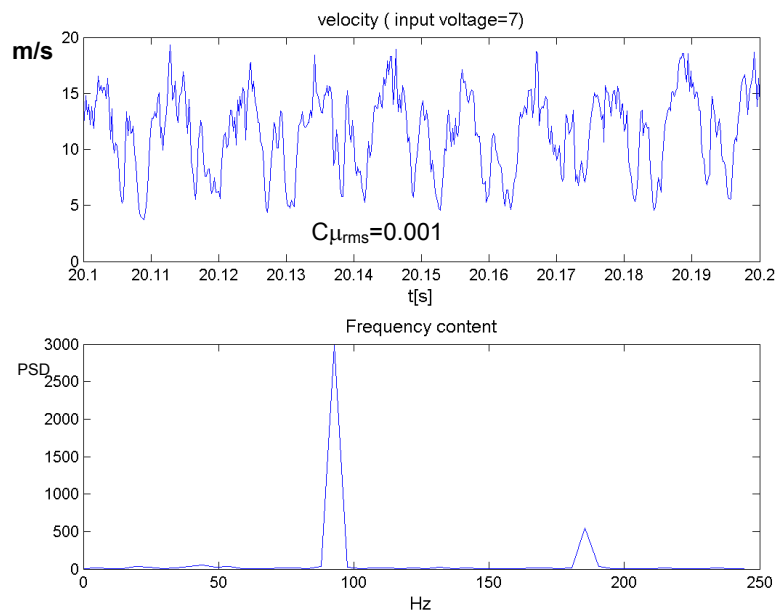
Figure 6.13b: Exit slot velocity and FFT at input voltage 7 volt
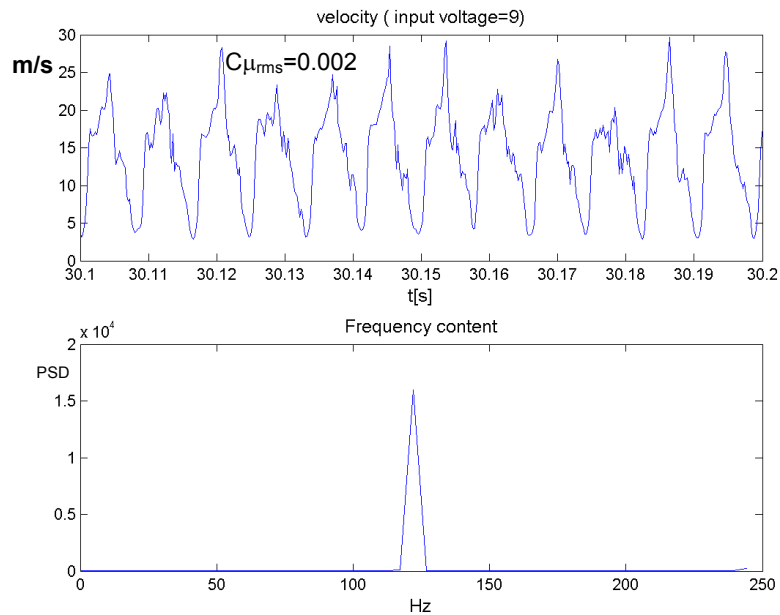
Figure 6.13c: Exit slot velocity and FFT at input voltage 9 volt

6.4 Full Scale Model Wind Tunnel Testing

6.4.1 Control OFF

In this section the results for the uncontrolled case is presented. The aerodynamic characteristics that will be presented are relative to lift, drag, polar and endurance curves with and without controlling. All wind tunnel data are acquired through a program (*Easy Wind Tunnel 2d*) developed at DPA for experimental data management. In figure 6.14 an example of typical user interface output with profile and pressure taps location, pressure distribution and wake form with indication of integral calculations of lift and drag.

Drag is calculated from measured data using different techniques. The best approximation is obtained with interpolated Betz drag that is also the value that will be reported in the characteristics curves. Lift is obtained through integral of measured pressure on the airfoil.
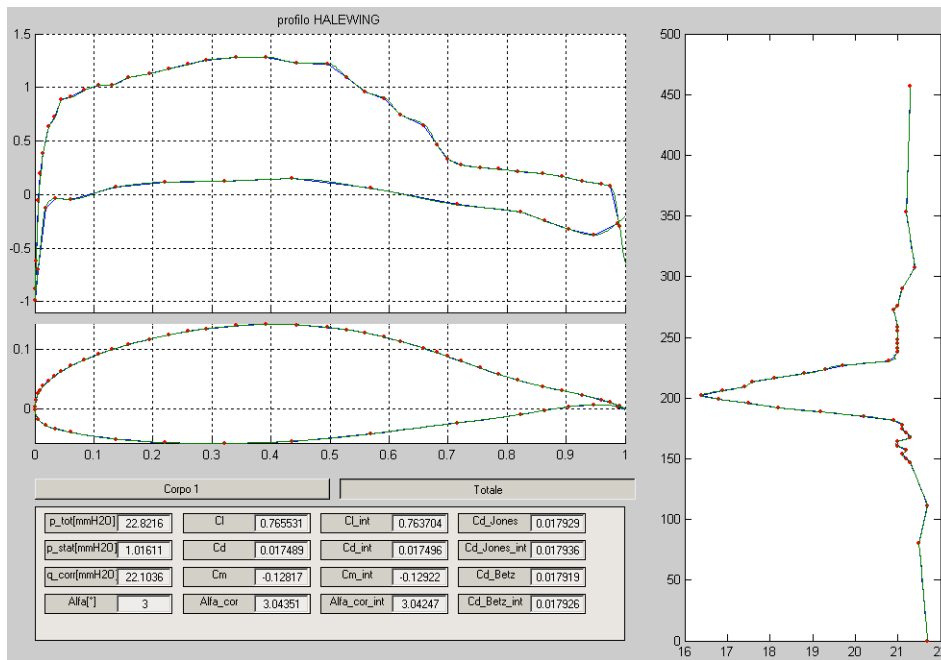
Figure 6.14: Example of user interface of DPA wind tunnel program

Two configurations has been tested: the clean configuration without imposed transition and stripped configuration with transition imposed at 4% in chord. Preliminary visualization tests has been done to identify the minimum numbers of strip layer to be used in order to produce transition in the range 0-10°. In figure 6.15 the visualization on the profile (upside) with and without strip for angle of attack equal to 4°.
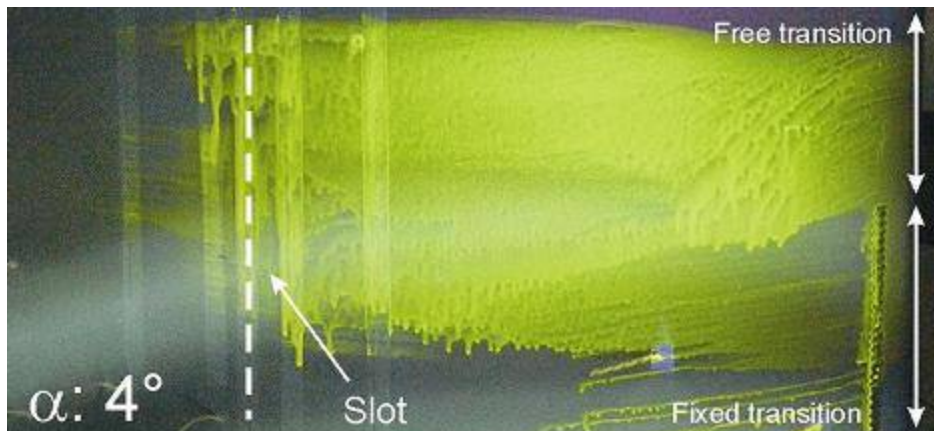
Figure 6.15: Flow visualization

Figure 6.16,.17,.18 show the comparison of results between clean and strip configurations for lift curve, polar and endurance with free stream Reynolds number equal to 8×10^5 for the uncontrolled case. As it can be seen the airfoil shows a strong dependence on surface roughness and laminar-turbulent condition. The airfoil, without imposed transition, seems to reach stall at $\alpha=9°$, but as illustrated in figure 6.16 the real stall occurs near $\alpha=30°$. The phenomenon occurring at α equal to 9° is only the changing of flow field from attached to separate condition (t.e. separation); after this angle the peak continues to grow, until the gain balances the loss due to higher separated area, and at $\alpha=32°$ the pressure peak falls down. As an example, figure 6.19 is illustrates some pressure distributions, where it is possible to see the "apparent stall" that occurs between $\alpha=8°$ and 9°and the real pre-stall condition at $\alpha=30°$. Finally in the figure 6.20 is reported the lift curve for the configuration with imposed transition for two different free stream Reynolds numbers, 8×10^5 and 1.2×10^6. The results seem to show not significant difference between the two tests, suggesting that in this velocity range the behaviour of uncontrolled airfoil does not change drastically.
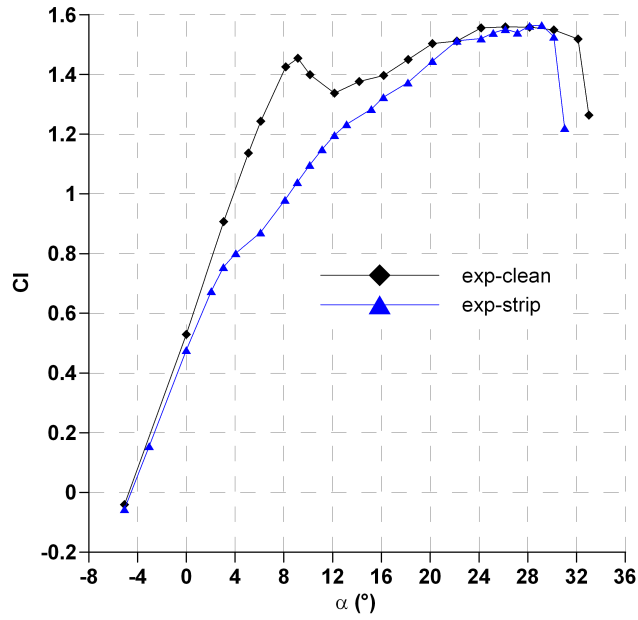
Figure 6.16: Comparison of strip-clean lift coefficient curves
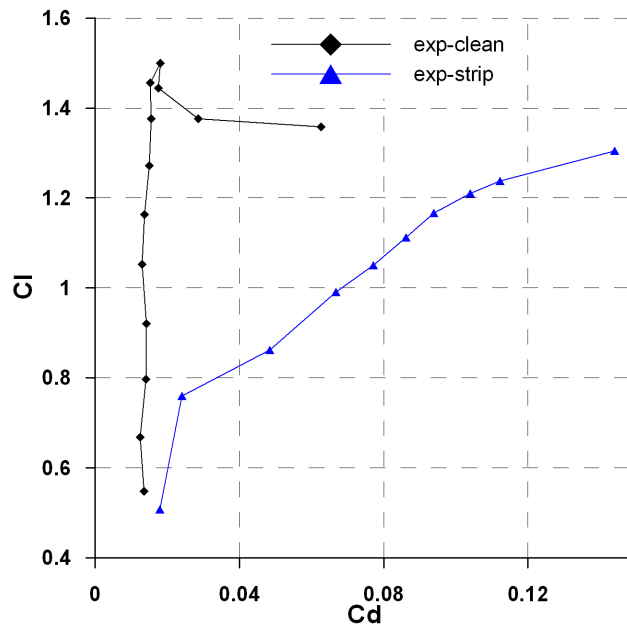
Figure 6.17: Comparison of strip-clean polar curves
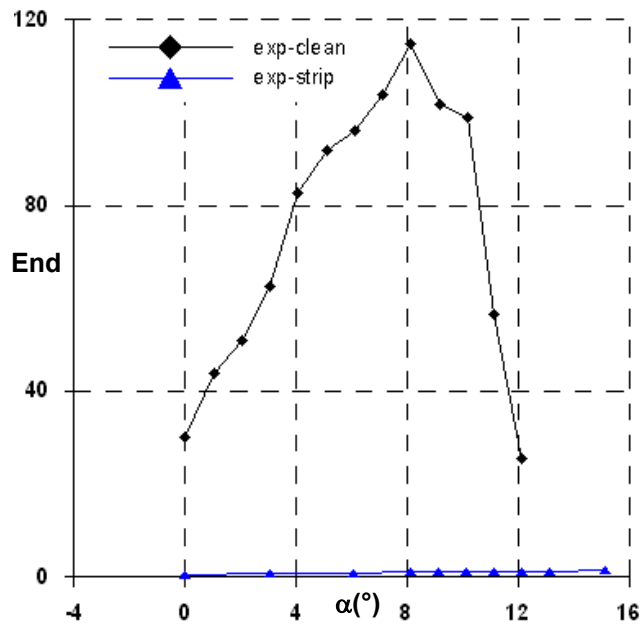
Figure 6.18: Comparison of strip-clean endurance
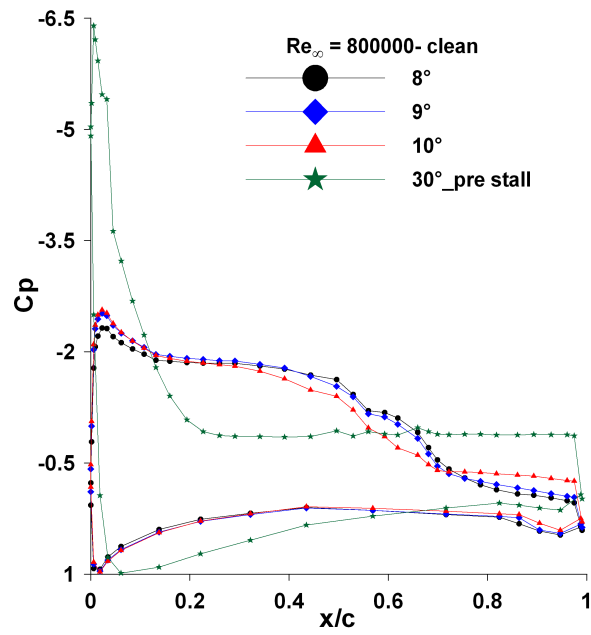
Figure 6.19: Pressure distributions
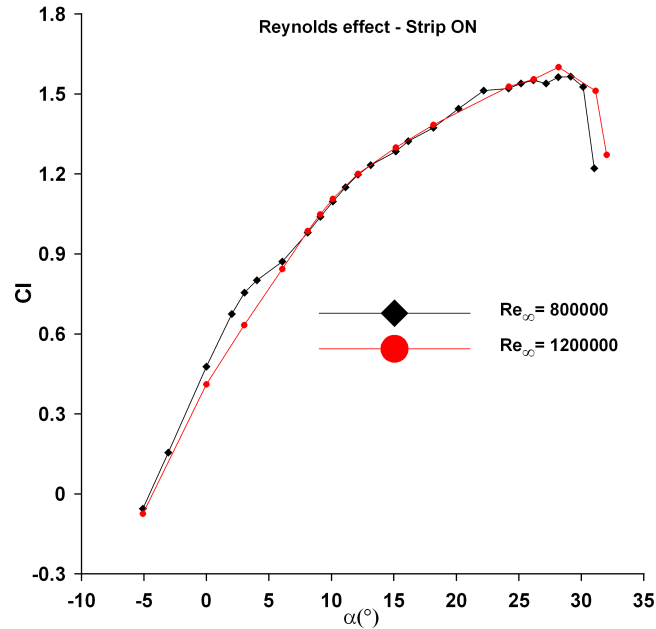
Figure 6.20: Lift coefficient curve, Reynolds number effect for uncontrolled case

6.4.2 Control ON

In this section the results relative to the application of control are presented. Different configurations have been tested, with and without imposed transition, both of them with steady and unsteady blowing for different reduced frequencies and momentum coefficient.

Figure 6.21a,b shows the lift coefficient and polar curve for the configuration without imposed transition for four conditions: no control applied (baseline), steady blowing with mean value of velocity equal to 18 m/s (green line), excitation frequency equal to 50Hz (blue line) and excitation frequency equal to 120 Hz (red line). In all cases the root mean square of momentum coefficient is approximately 0.2%. The same results are reported for the configuration with imposed transition, in figure 6.22a,b. Lift curves show that for all configurations the application of unsteady blowing produces better improvements than steady control, in particular

with frequency equal to 50 Hz. If only the polar curves is considered, this improvement remains only on configuration with imposed transition. In fact, when actuation is applied on clean configuration this shows an enhanced performance in terms of lift, but a worse behaviour in terms of drag (see polar curve), while on configuration with strip the application of steady\unsteady blowing produces improvement on both lift and drag characteristics (and obviously endurance and efficiency). This could be due to the fact that with clean configuration the laminar bubble, extending from leading edge to proximity (maybe including) the slot exit, and this inhibits the application of control, producing slightly positive effect on lift (increasing the pressure peak) but substantially increasing also the drag. A possible phenomenon could be that the weak blowing inside or near bubble produces an higher boundary layer thickness at bubble reattachment after transition, and this produces higher drag measurement. This phenomenon can be also observed in the figures 6.23a,b and 6.24a,b that shows the pressure distribution on the body surface and the wake survey for two cases: the first on is relative to clean configuration (α= 10°) and the second to strip configuration (α= 8°). For the clean configuration even if the effect in term of pressure distribution is slightly positive, the wake profile is larger (higher losses). There is an opposite behaviour for strip configuration where, at the same time the improvements on pressure is accomplished by slimmer wake profile respect to the uncontrolled case, improving the aerodynamic performances.
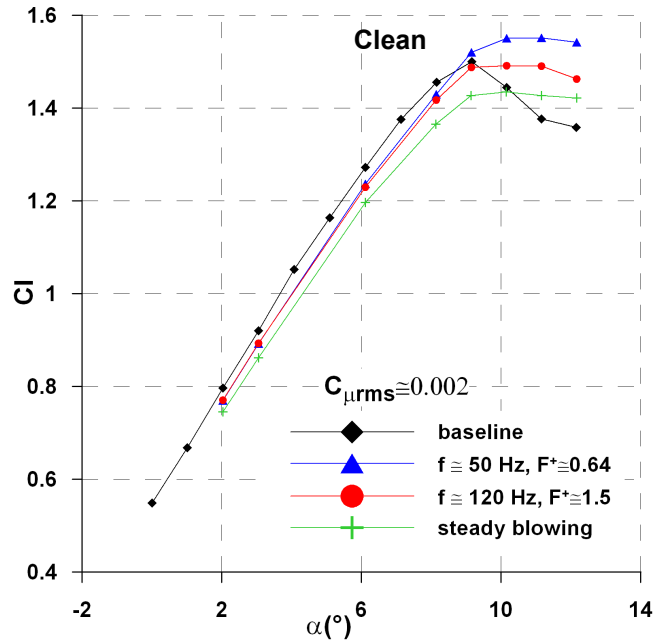
Figure 6.21a: Blowing effects on lift coefficient (free transition)
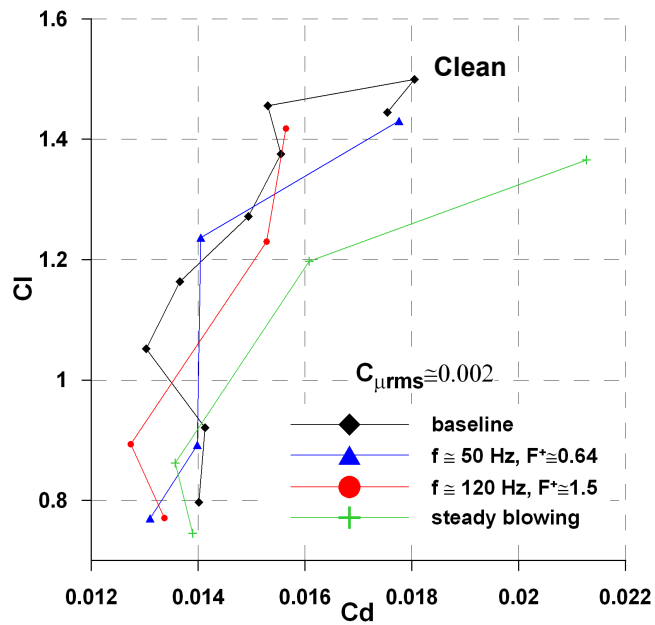
Figure 6.21b: Blowing effects on polar curves (free transition)
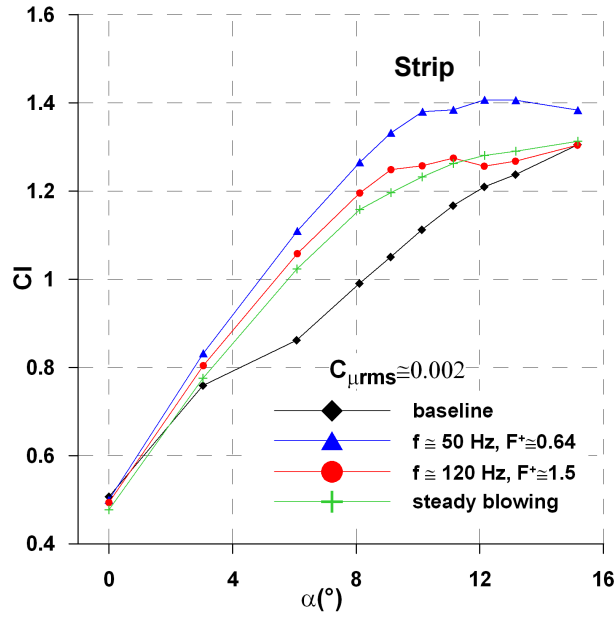
Figure 6.22a: Blowing effects on lift coefficient (strip on 4% in chord)
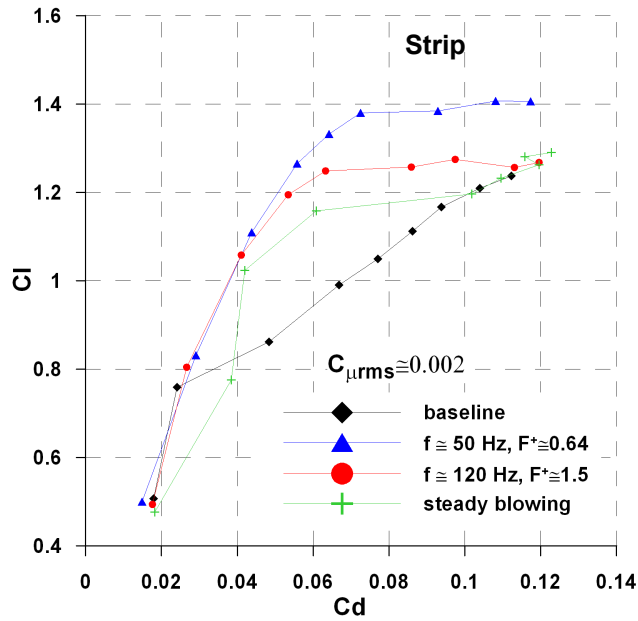
Figure 6.22b: Blowing effects on polar (strip on 4% in chord)
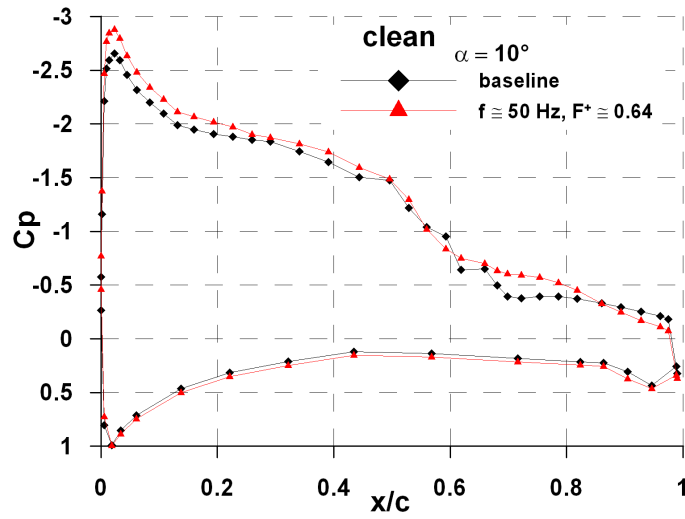
Figure 6.23a: Example of control effect on pressure distribution (free transition)
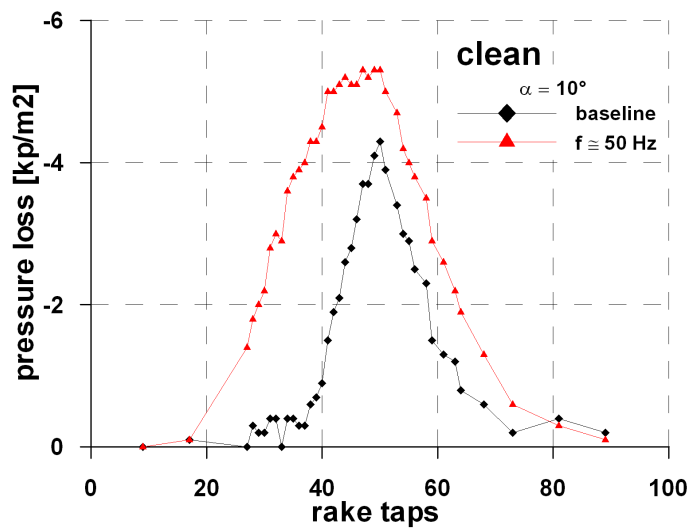
Figure 6.23b: Example of control effect on wake (free transition)
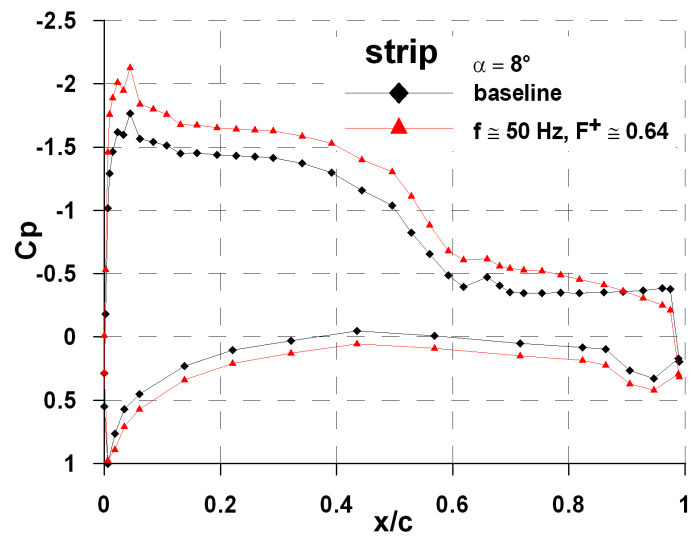
Figure 6.24a: Example of control effect on pressure distribution (strip on)
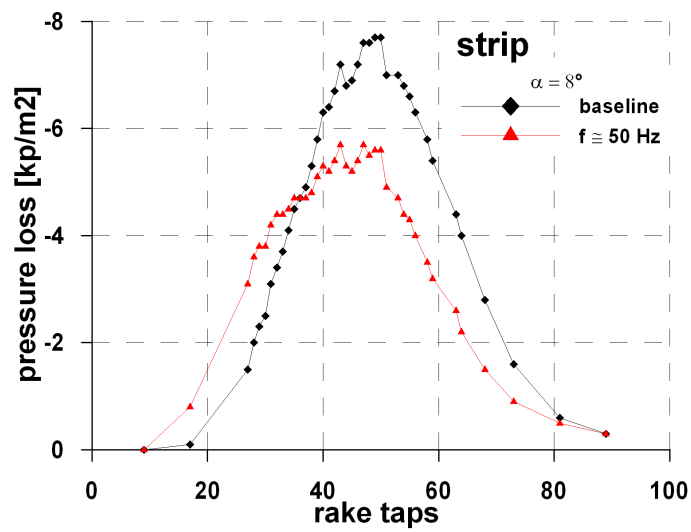
Figure 6.24b: Example of control effect on wake (strip on)

6.4.2.1 Frequency Effect

On the configuration with transition imposed, the effect of frequency variation on aerodynamic performances at some angles of attack has been studied deeply. The angles of attack chosen allow us to analyse the effect from the condition of weak separation (close to trailing edge) corresponding to $\alpha=4°$, to the condition of strong separation (upstream of slot exit) corresponding to $\alpha=12°$. At each angle of attack different values of actuation frequency has been tested in the range 0Hz-120Hz (0-1.5 in terms of reduced frequency), starting from the case with closed valve (0 Hz, no control applied). The results are presented in figure 6.25a,b in terms of percentage variation of lift and endurance respect to the condition of no control applied. It is possible to see how the positions of maximum improvement change with varying angles of attack, moving from 30 Hz (for the curve relative to $\alpha=12°$) to 120 Hz (for the curve relative to $\alpha=4°$), while for the curve relative to $\alpha=6$ and $8°$, the maximum remains at 80 Hz. This is due to the fact that higher angles of attack produce more extended separated area, and because the main shedding frequency of separated flow depends also from distance between separation point and trailing edge, the optimal actuation frequency changes with angle of attack. In particular higher is the angle of attack and the separated area, lower is the optimal actuation frequency. Another interesting result is that even if the endurance improvement is also appreciable for $\alpha=4$ and $12°$, the effect is stronger when the angle of attack is 6 or $8°$ where the improvement is higher than 60%. This is due to the fact that the exit slot position is fixed, and when the angle of attack is $4°$ the separation point is near trailing edge, far downstream from slot exit, and in the case of $\alpha=12°$ the separation point occur upstream the exit slot, while for angle of attack equal to 6 and $8°$ the separation point is close to exit slot location. This suggests that also the position of slot exit is strongly important for controlling the flow, and that, in principle, a movable slot exit position is desirable to obtain an optimal control system for all flight conditions.
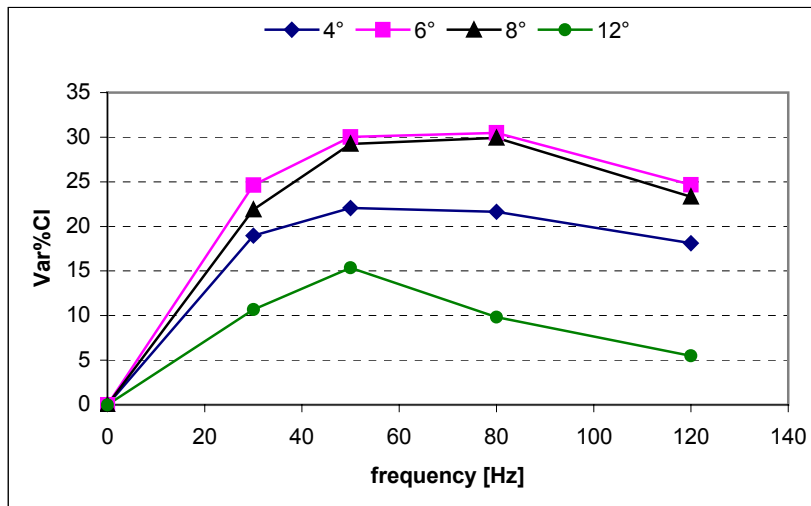
Figure 6.25a: Lift coefficient, detailed investigation on frequency effect (strip on)
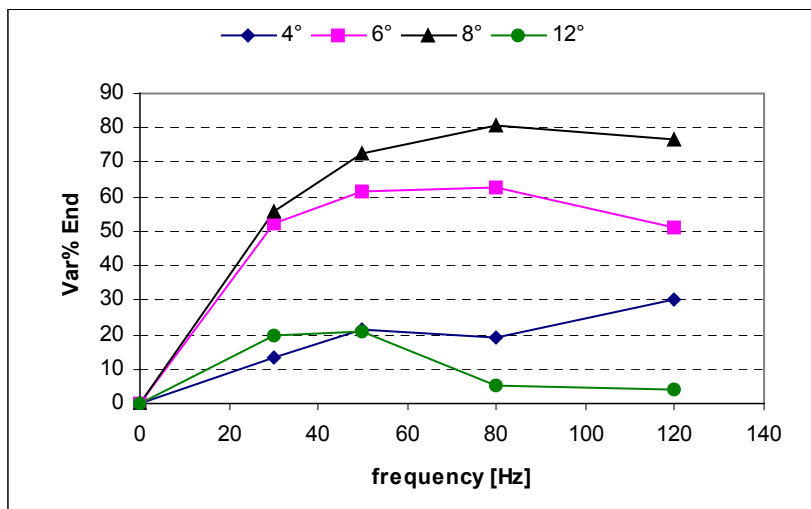
Figure 6.25b: Endurance, detailed investigation on frequency effect (strip on)

6.4.2.2 Reynolds Number Effect

The effect of free stream Reynolds number has been considered and the results are reported in the figure 6.26. The angle of attack has been fixed at $\alpha=8°$ as well as the exit slot mean velocity has been fixed. For this conditions, and for four different free stream Reynolds numbers (from 8×10^5 to 12×10^5) the maximum lift increment obtainable for the actuation frequency range 0-120Hz has been reported. The values in table 1 and the figure 6.26 summarize the results obtained. It is possible to see that increasing free stream Reynolds number the maximum lift coefficient increment decreases. The more significant jump in the lift coefficient increment is when the ratio between injection velocity and free stream velocity rises from 0.45 to 0.53. In fact increasing of 17% for this ration produces   100% increasing in lift coefficient increment, while when velocity ratio jumps from 0.53 to 0.81 (increase of 52%) the lift increment increases only about 36%. Higher velocity mean higher improvement, but also higher power input, so from this analysis and for this case, it is possible to identify, for the velocity ratio close to 0.5-0.6, a good compromise in terms of cost/benefits analysis.

	Vj_mean	Vjet/Vinf	Vinf	f_opt	d_Clmax
A	15 m/s	0.81	18.5	80 Hz	0.3
B	15 m/s	0.53	28.3	120 Hz	0.22
C	15 m/s	0.48	31.2	120 Hz	0.19
D	15 m/s	0.45	33.3	80 Hz	0.11

Table 1
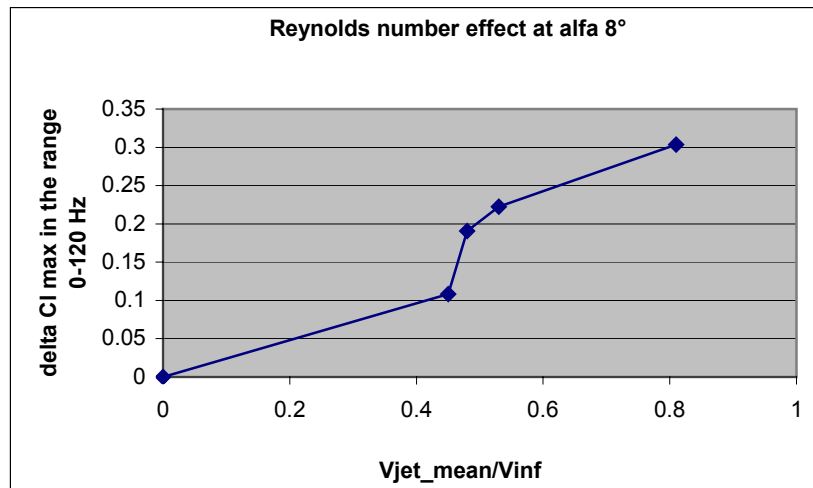
Figure 6.26: Strip configuration, maximum lift coefficient increment with varying
free stream Reynolds number

6.4.2.3 Comparisons with the Numerical Simulations

In this section the comparison of experimental results with the numerical simulations both for controlled and uncontrolled case (with strip ON) is presented in the figures 6.27,.28,.29,.30. In all figures the full line is related to the numerical simulation and marker line to experimental results.

In the first two figures 6.27 and 6.28 the results are related to the case with control not activated. In the figure 6.27 are reported the lift curves (figure 6.27a) and the pressure distribution (figures 6.27b,c,d) for three different angles of attack that correspond to three increasing levels of separated area. In the figure 6.28a,b the curves of efficiency and endurance are reported in the range 0-15°. In fact although the numerical simulation have been performed also for higher angles of attack, the drag can be accurately measured up to 15° (for higher angles the wake becomes too large to be correctly captured). The figures show an overall good agreement with experimental data for this configuration, the high lift behaviour and the lift slope are well captured from the numerical simulation. Some problems come out

when also the drag prediction is considered; in fact the figure (6.28a) shows how the efficiency is over predicted by numerical simulation respect the experimental tests, even though the general behaviour is well captured. These differences are mainly due to the turbulence model, airfoil shape and model building. It is important to point out in fact that if one hand the numerical simulation is intrinsically characterized by errors due to the use of turbulence model developed for boundary layers but also used for massive separation (small errors in the prediction of velocity fields could lead to sensible errors in drag prediction), it is also true that the tested airfoil is very sensible to the experimental condition, and very fine differences between theoretical shape and "built" shape (actuator section, surface roughness and airfoil curvature) may influence the results.

In the figures 6.29 and 6.30 and 6.31 the comparison of results with control activated are reported. In the figure 6.29 the lift curves are reported with the control activated with frequency equal to 50 Hz (red lines) and 120 Hz (blue lines) together with the baseline (control off, black lines). The figure shows as the numerical simulation predicts a more effectiveness of control respect to the experimental data.

For both excitations (red and blue continues lines) the lift enhancement in positive also near the stall angle, while in the experimental tests the control is effective until the angle of attack of 15°. The same behaviour showed in the figure 6.30 and 6.31, where the numerical simulation over predict the efficiency gain and endurance gain when the control is applied. In spite of this discrepancy the general behaviour is well captured, in fact all the lift coefficient curves, efficiency and endurance curves suggest that the solution of 50 Hz is more effective respect the ones at 120 Hz, and also the ineffective of control at low angles of attack is captured from numerical simulation. Globally the numerical tests has respect its main role of identify a qualitative behaviour of the system, in order to identify the best suitable configurations to test in the wind tunnel. It remains the disagreement with experimental results for a quantitative analysis. An important observation is that in the numerical control law a sinusoidal wave without distortions has been

considered, while in the real flow condition the wave form is slightly different. Future improvements could be to consider an inlet injection that exactly match the experimental injection jet measured in the wind tunnel (at the slot exit) and comparing the results. Some others improvements could be adopted with using of more sophisticated techniques that actually are being very popular to treat this argument, like LES (Large Eddy Simulation) or the less expensive (in the sense of computational cost) DES (Detached Eddy Simulation). This will be object of future studies.
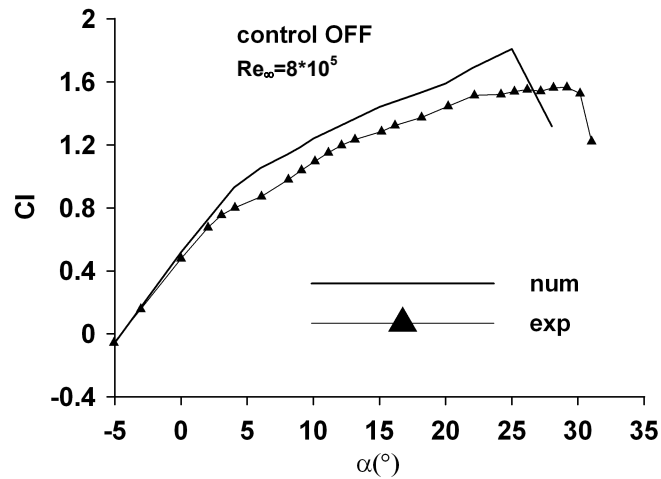
Figure 6.27a: Comparison of numerical and experimental results for lift coefficient
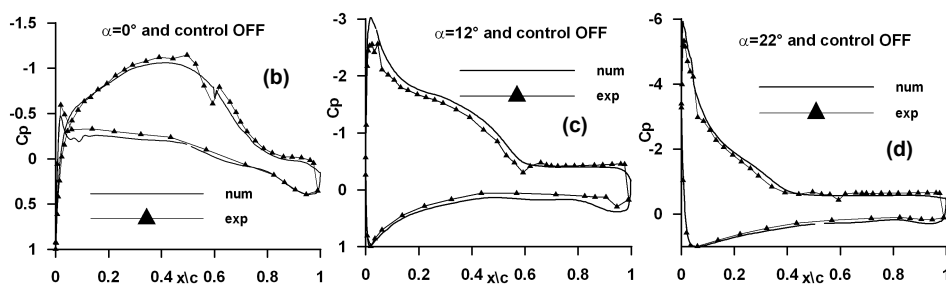
Figure 6.27b,c,d: Comparison of numerical and experimental results for pressure distribution for $\alpha=0°$-$12°$-$22°$ (b,c,d)
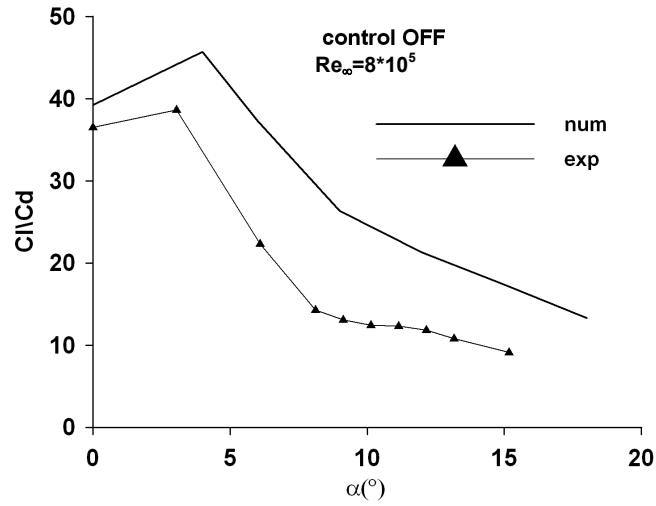
Figure 6.28a: Comparison of numerical and experimental results for effciency
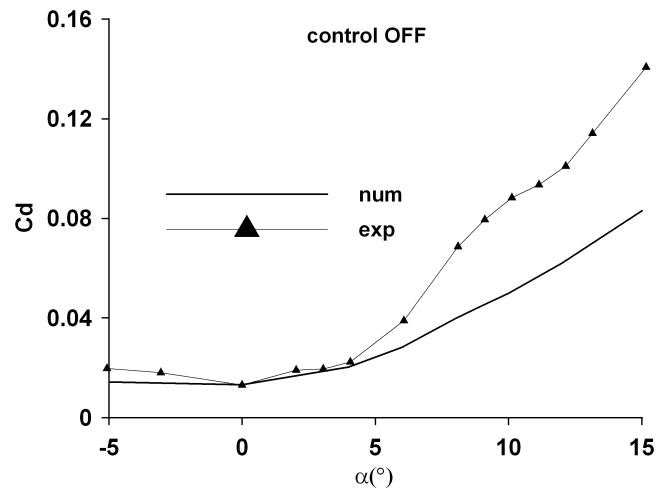
Figure 6.28b: Comparison of numerical and experimental results for drag
coefficient
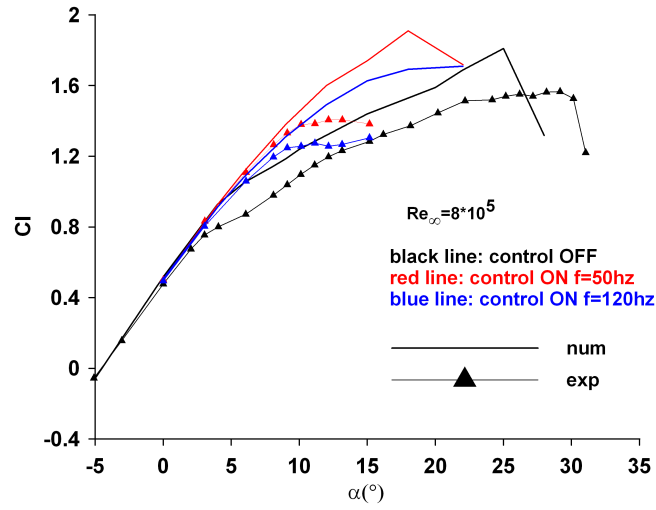
Figure 6.29: Lift coefficient curves, numerical and experimental comparison.
Control ON
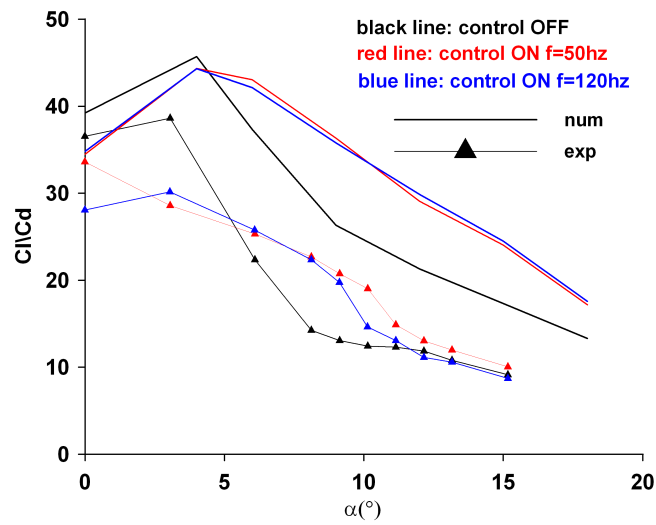
Figure 6.30: Efficiency curves, numerical and experimental comparison. Control
ON
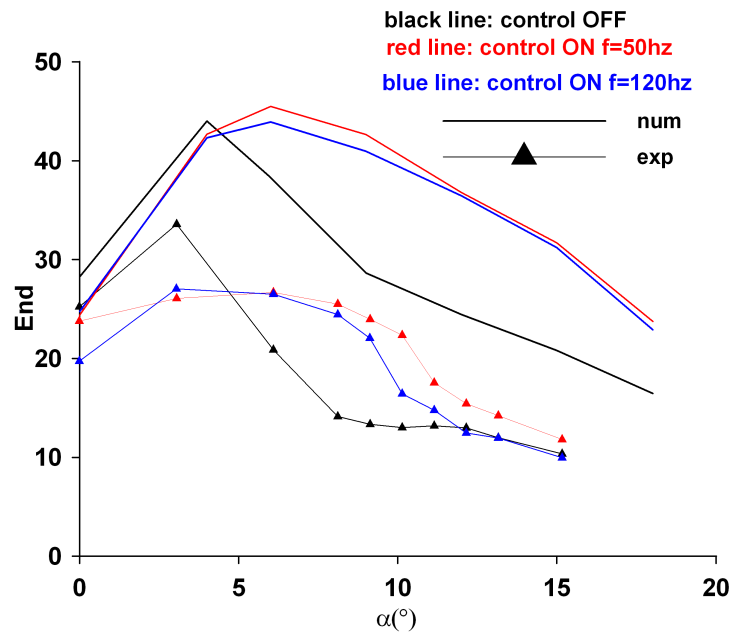
Figure 6.31: Endurance curves, numerical and experimental comparison. Control ON

Chapter 7

Conclusions and Future Works

7.1 Conclusions

Detailed

- Steady suction is an effective tool to delay separation but its performances are strongly dependent on the position of slot cut.
- Turbulent boundary layer velocity profile is strongly affected by wall transpiration, and an "ad hoc" modification is desirable for closure formulas used in the viscous-inviscid interaction method.
- In the pulsed blowing system the tubing length seems to produce the most significant effect on resonant frequencies, while slot exit and cavity volume influence mainly the resonant peak's amplitude.
- Numerical computations and experimental tests have pointed out that unsteady blowing is more effective than steady blowing, and that an optimal range of actuation frequencies exists once the flow conditions have been fixed. In the same way the excitation can also have detrimental effects on the boundary layer structure if the jet angle is too high or the position of slot cut is far upstream respect separation point.
- The endurance improvement can be close to 70% if the reduced frequency and momentum of injected flow are properly chosen.
- The optimum frequency depends on the aerodynamic objective to be maximized.

General

Numerical and experimental investigation in the wind tunnel has been performed for the steady suction and unsteady blowing. Steady suction has been investigated theoretically through the analysis of velocity profile in turbulent boundary layer, numerically through 2d panel methods and experimentally through tests on small

scale model in the wind tunnel. Unsteady blowing has been investigated theoretically, through the modelling of the whole system behaviour, numerically through RANS computations and experimentally through tests on a 2D wing in the wind tunnel. The unsteady blowing has been realized through a rotating valve, and the theoretical performance of the whole unsteady-blowing system has been examined using electro-acoustic analogy to model the system from the oscillating valve to the exit of the actuator. A combination of a lumped-element model for the actuator and a distributed model for the tubing, has been used to obtain a transfer function for the overall pulsed-blowing system. This has allowed the analysis of the functional dependence of the whole system on geometrical parameters (tubing length, cavity volume and slot exit) and has shown that the ratio between injection slot velocity and input pressure could be maximized once the system operates in proximity of resonant condition. Tubing length seems to produce the most significant effect on resonant frequencies, while slot exit and cavity volume affect mainly the resonant peak's amplitude. Theoretical considerations suggest that the effectiveness of pulsed blowing depends mainly on the extension of the separated area, free stream Reynolds number, excitation frequency and strength of injected flow. This can be summarized through two dimensionless parameters: reduced frequency and momentum coefficient. Numerical and experimental tests have been performed in order to point out the behavior of the system varying these two parameters through the variation of the compressed air pressure, valve frequencies rotation and angle of attack. The result is that, depending on the aerodynamic performance to be optimized (efficiency, lift or endurance), the best actuation frequency changes. During this study many interesting new aspects has been pointed out through experimental results, but some other aspects have not been investigated, due to the high complexity of the problems. The influence of slot cut shape and position or the influence of chamber volume and tubing length, for example, are part of this group.

7.2 Future Works

In the next future the idea is, on one hand, to continue the investigation on configurations used for the present work, for example, analyzing the behaviour of the system varying the slot shape and tubing lengths, and, on the other hand, considering a new approach for the problem of controlling the separation on the rear part of airfoil though an "ad hoc" system, hopefully more robust respect to the variation of flow field condition and without using a distributed system between rotary valve and actuators. In fact, it is our opinion that, even if an optimally use of the distributed system produces maybe better performances in terms of slot exit velocity than system without tubing, it is also true that a solution without tubing, from practically point of view, is more technologically viable. An idea on the valve shape and insertion is currently being considered that could strongly simplify the entire system. The valve should be directly inserted into the airfoil and connected to the internal chambers, avoiding the use of distribution system. Together with experimental investigation, also numerical analysis are planned in order to achieve more understanding about some results that apparently were not expected, like the worse behaviour of the system with clean configuration, probably due to the interaction with the laminar separation bubble.

Appendix A

In this appendix the problem of transpired flows is faced examining the effects of wall transpiration on integral boundary layer equations. In the first part the derivation of skin friction formula for not transpired flows following the approach used by Coles is presented, and in the second part the same approach will be applied with the attempt to derive similar formula when wall transpiration is imposed.

- <u>Turbulent boundary layer when transpiration is zero</u>

The integration of the momentum equation of boundary layer gives the well known von-Karman integral relation (see White [21]).

$$\frac{d\theta}{dx} = \frac{1}{2}Cf - (2 + H_{12})\frac{\theta}{u_e}\frac{du_e}{dx} \qquad (A1)$$

where θ is the momentum thickness, H_{12} is the shape parameter (ratio of displacement and momentum thickness), u_e is the velocity at the outer edge of boundary layer, and Cf is the skin friction.

Note that this equation has the same form as that for laminar flow since has been neglected normal stresses and the Reynolds stress term vanishes at the wall and at the edge of the boundary layer (the integral parameters θ and δ^* are defined in terms of the mean velocity components).

In the case of laminar flows is possible to obtain a solution to the boundary-layer problem by assuming an appropriate velocity profile shape. This is obtainable by considering that for laminar flows:

$$\frac{u}{u_e} = f\left(\frac{y}{\delta}\right) \qquad (A2)$$

Unfortunately, due to the more complex nature of turbulent flows, no similar solution of this type produce results of adequate precision. The one exception to this is Prandtl's power law profile for zero pressure gradient flows.

Since equation (A1) contains three unknown variables θ, H_{12} and Cf, others two additional independent relations to provide closure are necessary. Unfortunately, the two new relations, if they are reliable over a wide range of conditions, will contain other variables for which more relations must be found without simplify the problem. To construct an accurate model for turbulent boundary-layer calculation is necessary to start with a consideration on its velocity profiles.

Turbulent velocity profile (see Pope[30] and White[21])

The turbulent boundary-layer velocity profile looks like different from laminar profile and generally is much fuller with higher velocity gradients near the wall. To describe this profile more in deep, it is convenient to divide it into its principal layers:

- INNER LAYER : VISCOUS SHEAR DOMINATES - $\mu\dfrac{\partial\overline{u}}{\partial y}$

- OUTER LAYER : TURBULENT SHEAR DOMINATES - $\rho\overline{u'v'}$

- OVERLAP LAYER : BOTH TYPES OF SHEAR ARE IMPORTANT

Considering the physical laws that govern each of these regions suggested by Prandtl and von Karman:

INNER LAW

$$\overline{u} = f(\tau_w, \rho, \mu, y) \qquad \text{Prandtl}$$

The mean velocity in the inner region depends on the wall shear, fluid properties and the distance from the wall.

OUTER LAW

$$u_e - \overline{u} = f(\tau_w, \rho, y, \delta) \qquad \text{von Karman}$$

For the outer layer, von Karman deduced that the wall tends to act as a source of retardation, reducing the local velocity u below the free stream value u_e in a

manner which is dependent upon the wall shear stress and the distance y from the wall and not from viscosity.

OVERLAP LAW

$$\overline{u}_{inner} = \overline{u}_{outer}$$

This law says that in the overlap region both outer and inner laws must be valid.

Both the inner and outer equations contain 5 variables and 3 fundamental dimensions (mass, length and time), so from Buckingham theory there are 5-3=2 dimensionless groups that are involved in each case.

From this consideration is possible to see that the two laws are the following:

for the INNER LAW $\quad \dfrac{\overline{u}}{u^*} = f(\dfrac{yu^*}{\nu})$ (A3)

where $u^* = \sqrt{\dfrac{\tau_w}{\rho}}$ is the friction velocity

and for the OUTER LAW:

$$\frac{U - \overline{u}}{u^*} = g(\frac{y}{\delta})$$ (A4)

In the overlap layer both laws are valid, so:

OVERLAP $\quad \dfrac{\overline{u}}{u^*} = f(\dfrac{\delta u^*}{\nu} \dfrac{y}{\delta}) = \dfrac{u_e}{u^*} - g(\dfrac{y}{\delta})$ (A5)

It is possible to demonstrate that it is only satisfied if the functions involved are both logarithmic. Thus the results is:

INNER $\quad \dfrac{\overline{u}}{u^*} = \dfrac{1}{\kappa} \ln(\dfrac{yu^*}{\nu}) + B$

OUTER $\quad \dfrac{U - \overline{u}}{u^*} = \dfrac{1}{\kappa} \ln(\dfrac{y}{\delta}) + A$ (A6a,b)

Where κ, A and B are dimensionless constants. Thus in the overlap region:

OVERLAP $\quad \dfrac{\overline{u}}{u^*} = \dfrac{1}{\kappa} \ln(\dfrac{yu^*}{\nu}) + B = \dfrac{u_e}{u^*} + \dfrac{1}{\kappa} \ln(\dfrac{y}{\delta}) - A$ (A7)

The values of the dimensionless constants come from experiment and as proposed by Nikuradse (1930) or Coles (1955) they can be considered equal to:

$\kappa \cong 0.4$ and $B \cong 5.5$ (Nikuradse) or $\kappa \cong 0.41$ and $B \cong 5.0$ (Coles)

The parameter A in the outer region as been considered constant. It has, however, been found that this value is not the same for different types of flow and that it is influenced by pressure gradient. It should also be noted that, from equation (A7) the value of A must change outside the overlap region reducing towards zero at the boundary layer edge.

When separation occurs the outer layer becomes important.

In the region very close to the wall, as has been already indicated, the laminar viscous shear term dominates and the following expression is valid:

$$\tau_w = \mu \frac{\partial \bar{u}}{\partial y} \quad \text{(viscous sub-layer)}$$

close to the wall is also true that:

$$\frac{\partial \bar{u}}{\partial y} = \frac{\Delta \bar{u}}{\Delta y} = \frac{u - 0}{y - 0} = \frac{\bar{u}}{y}, \text{ so}$$

$$\tau_w = \mu \frac{\bar{u}}{y} \Rightarrow u^+ = y^+ \tag{A8}$$

where $\quad u^+ = \dfrac{\bar{u}}{u^*}$ and $y^+ = \dfrac{y\, u^*}{\nu} \quad$ (inner variables)

At some point in the boundary layer the viscous-sub-layer must merges smoothly into the inner layer as indicated by the equations (A6a,b).

Various schemes have been developed, from physical considerations of the flow, to provide a smooth change from equation (A8) to one which satisfies the inner law. The resulting profile is usually plotted as y^+ versus u^+ and the profile shape resulting from the equations is shown in the figure A1 (taken from White[21]).
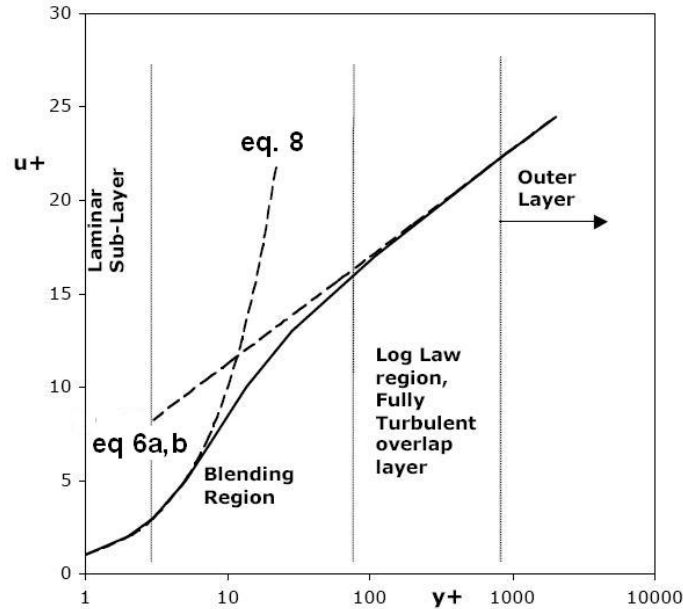
Figure A1: Typical velocity profile in turbulent boundary layer (White[21])

Considering with more attention that the outer region of the turbulent boundary-layer is more sensitive to the effects of pressure gradient than the inner layer, is important to modify opportunely the outer formulation in order to take into account the pressure gradient. So for the outer law the correct functional dependencies are:

$$u_e - \overline{u} = f\left(\tau_w, \rho, y, \delta, \frac{dp}{dx}\right)$$ where now it is present the external pressure gradient.

This becomes after dimensionless procedure:

$$\frac{U - \overline{u}}{u^*} = g(\frac{y}{\delta}, \frac{\delta}{\tau_w}, \frac{dp}{dx})$$

The new parameter involving pressure gradient is characteristic of flow in the outer layer. It is convenient, however, to replace the boundary-layer thickness δ with the displacement thickness δ^*

$$\delta^* = \int_0^\infty \left(1 - \frac{u}{u_e}\right) dy \tag{A9}$$

The parameter then becomes

$$\frac{\delta^*}{\tau_w}\frac{dp}{dx} = \beta \quad \textit{Clauser} \text{ parameter} \tag{A10}$$

An approach to the outer layer was proposed by Coles for zero pressure gradient flow, and assumed that the deviations from logarithmic law of the velocity above the overlap layer, once normalised by the maximum deviation (at y=δ), was dependent from a single parameter named wake function f_w.

If this correction is not considered a considerable error occurs in the boundary layer calculation, in fact in the overlap region the law is (using inner variables):

$$u^+ = \frac{1}{\kappa}\ln(y^+) + B \tag{A11}$$

where κ = 0.4 B = 5.5 (Nikuradse values)

and after substitution:

$$u^+ = 2.5\ln(y^+) + 5.5 \tag{A12}$$

If this behaviour is compared with experimental measurements significantly differences are present as indicated in figure A2. This is particularly true when adverse pressure gradients is present.
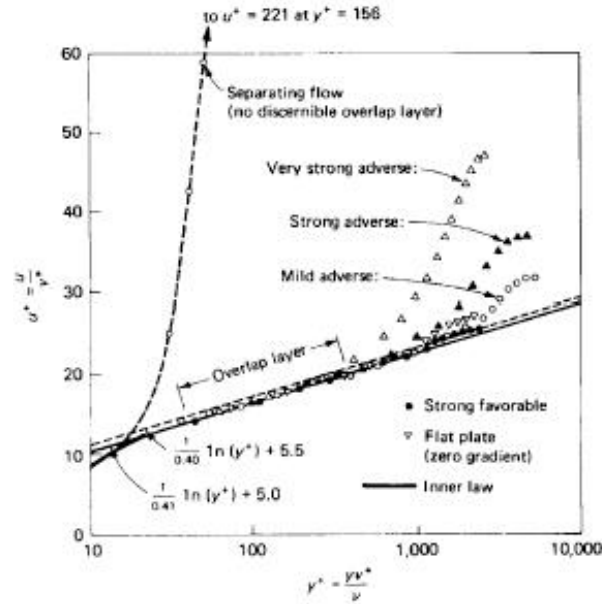
Figure A2: Formula A12 and comparison with experimental data (from White [21])

The deviation between this equation and the data was partially resolved by Coles who proposed the following correction after an experimental curves fitting:

$$\frac{u^{+} - \frac{1}{\kappa}\ln(y^{+}) - B}{u_e^{+} - \frac{1}{\kappa}\ln(\delta^{+}) - B} \cong 0.5f_w(\frac{y}{\delta}) \approx 2\sin^2(\frac{\pi}{2}\frac{y}{\delta}) \tag{A13}$$

where $\delta^{+} = \dfrac{\delta u^{*}}{\nu}$

In this equation the velocity deficit between the measured velocities u^{+} and u_e^{+} and those predicted by (A12) are linked to some function of y/δ.

The function f_w is called the *wake function* and is normalised to be zero at the wall and has the value $f_w = 2$ at $y = \delta$. This satisfies the condition that u/u_e must be 1 at at $y/\delta=1$.

This expression is known as the law of the wake and can be combined with the overlap equation or law of the wall to provide a composite function that covers both overlap and outer layers with more accuracy also when pressure gradient is present.

It is important to point out that when equations (A6a,b) for the outer layer are used, the parameter A will vary outside the overlap region. Coles wake function, however, allows to fix A as a constant through both the overlap and outer layers. This is achieved with the following procedure:

Coles developed (A13) function by first reconsidering equation (A7) that when rearranged gives:

$$A = u_e^+ - 2.5\ln(\delta^+) - 5.5 \tag{A14}$$

Observing that:

$u_e^+ = u_e^+$ (log law) + [u_e^+ (actual value) – u_e^+ (log law)]

and considering that in the overlap region the actual value will be the same as the log law value, the above expression becomes

$u^+ = 2.5 \ln y^+ + 5.5 +[u^+ -(2.5 \ln y^+ + 5.5)]$

or

$$u^+ = 2.5\ln(y^+) + 5.5 + \overbrace{\left[\frac{u^+ - 2.5\ln(y^+) - 5.5}{u_e^+ - 2.5\ln(\delta^+) - 5.5}\right]}^{(a)} \cdot \overbrace{\left[u_e^+ - 2.5\ln(\delta^+) - 5.5\right]}^{(b)}$$

The term (a) is equivalent to Coles wake function and term (b) is equivalent to the constant A. Finally the equation becomes:

$$u^+ = \frac{1}{\kappa}\ln(y^+) + B + \frac{\Pi}{\kappa}f_w(\frac{y}{\delta}) \tag{A15}$$

For equilibrium turbulent boundary layers Π has been found to be a function of Clauser parameter β as given by equation (A10), and one possible form of this function has been given by White [21] as:

$$\Pi \sim 0.8*(\beta + 0.5)^{0.75} \tag{A16}$$

Thus, through this relation a pressure gradient dependence is considered in the velocity profile shape. It is of particular importance since it is applied to most of the boundary layer. From the consideration that If the boundary layer is divided into its constituent parts, expressing each region as a percentage of the total Boundary-layer thickness, the results is (from Pope [30]):

- Viscous sub-layer: $\approx 1\%$
- Logarithmic Region: $\approx 20\%$
- Outer Region: $\approx 90\%$

It is interesting that equation (A15) which is applied only to the logarithmic overlap region and outer region may be valid over 99% of the boundary layer.

It is possible, therefore, by using equation (A15) to derive simple expressions for the boundary-layer thickness parameters. These expressions should provide an acceptable approximation to reality. The procedure is to consider the integral boundary layers parameters (A17) and proceeds to integrate through boundary layer thickness using (A15).

$$\delta^* = \int_0^\infty \left(1 - \frac{u}{u_e}\right) dy \quad \text{(a)}$$

$$\theta = \int_0^\infty \frac{u}{u_e}\left(1 - \frac{u}{u_e}\right) dy \qquad \text{(b)} \qquad \text{boundary layer integral parameters} \qquad \text{(A17a-b-c)}$$

$$H_{12} = \frac{\delta^*}{\theta} \qquad \text{(c)}$$

observing that $\dfrac{u}{u_e} = \dfrac{u}{u^*}\dfrac{u^*}{u_e} = \dfrac{u^+}{u_e^+}$, it is possible to write the (A17a-b) as follow

$$\frac{\delta^*}{\delta} = \int_0^1 \frac{u_e^+ - u^+}{u_e^+} d\left(\frac{y}{\delta}\right) \qquad \text{(a)}$$

$$\frac{\theta}{\delta} = \frac{1}{u_e^{+2}} \int_0^1 \frac{u^+ (u_e^+ - u^+)}{u_e^+} d\left(\frac{y}{\delta}\right) \qquad \text{(b)}$$

(18a,b)

substituting the (A15) and the expression for f_w:

$$\frac{\delta^*}{\delta} = \int_0^1 \frac{\frac{1}{\kappa}\ln\delta^+ + B + \frac{2\Pi}{\kappa} - \left[\frac{1}{\kappa}\ln y^+ + B + \frac{2\Pi}{\kappa}\sin^2(\frac{\pi}{2}\frac{y}{\delta})\right]}{u^+} d(\frac{y}{\delta}) \qquad (A19)$$

But $u^+ = \dfrac{u}{\sqrt{\tau_w/\rho}}$ and the skin friction coefficient $C_f = \dfrac{\tau_w}{0.5\rho u_e^2}$

so $u_e^+ = \dfrac{2}{\sqrt{C_f}} = \lambda$

the integral becomes (after some omitted passages):

$$\frac{\delta^*}{\delta} = \frac{1}{\lambda}\left\{\left[\frac{1}{k}\frac{y}{\delta}\ln\delta^+ + \frac{y}{\delta}B + \frac{y}{\delta}\frac{2\Pi}{k}\right]_0^1 - \int_0^1\left[\frac{1}{\kappa}\ln y^+ + B + \frac{2\Pi}{\kappa}\sin^2(\frac{\pi}{2}\frac{y}{\delta})\right]d(\frac{y}{\delta})\right\}$$

finally it becomes

$$\frac{\delta^*}{\delta} = \frac{1}{\lambda}\left[\frac{1}{k}\ln\delta^+ + \frac{\Pi}{k} - \int_0^1\frac{1}{k}\ln y^+ d(\frac{y}{\delta})\right]$$

as: $\int u\, dv = vu - \int v\, du$ \qquad\qquad\qquad (A20)

and observing that:

$$\frac{1}{\kappa}\int_0^1 \ln(y^+)\, d(y/\delta)$$

may be expressed as

$$\frac{1}{\kappa\delta}\int_0^\delta \ln(y^+)\, d(y)$$

using the (A20) with following positions:

$$u = \ln\frac{yu^*}{\nu} \quad \text{and} \quad v = y \qquad\qquad (A21)$$

the entire integral becomes

$$\frac{\delta^*}{\delta} = \frac{1+\Pi}{\kappa\lambda}$$

(A22)

following the same process for the momentum thickness equation the results is:

$$\frac{\theta}{\delta} = \frac{1+\Pi}{\kappa\lambda} - \frac{2+3.179\,\Pi+1.5\,\Pi^2}{\kappa^2\,\lambda^2}$$

(A23)

and consequently the parameter H_{12} is given by (after some omitted manipulations):

$$H_{12} = \frac{\dfrac{1+\Pi}{k\lambda}}{\dfrac{1+\Pi}{\kappa\lambda} - \dfrac{2+3.179\,\Pi+1.5\,\Pi^2}{\kappa^2\,\lambda^2}} = \frac{\lambda}{\lambda - a(\Pi)}$$

(A24)

where $\quad a(\Pi) = \dfrac{2+3.179\,\Pi+1.5\,\Pi^2}{\kappa(1+\Pi)}$

As it is expected the mathematical model for turbulent boundary layer is more complicated than the laminar model.

Skin friction formula derivation

For this method the Coles velocity profile representation is used to derive a skin friction correlation formula. It has been already illustrated that, starting from Coles profile representation for velocity in the boundary layer is possible to obtain the shape parameter H_{12} from equation (A24). Considering again the Coles law of the wake (A15):

$$u^+ = \frac{1}{\kappa}\ln(y^+) + B + \frac{\Pi}{\kappa}f_w(\frac{y}{\delta}) \quad \text{Coles law of the wake}$$

and considering that the skin friction ($4/\lambda^2$) is related to Re_δ and Re_θ by solving following equation at the edge of the boundary layer:

$$\lambda = u^+\Big|_{y=\delta} = u_e^+ = \frac{u_e}{u^*} = \frac{1}{k}\ln\delta^+ + B + \frac{2\Pi}{k} = \frac{1}{k}\ln\frac{Re_\delta}{\lambda} + B + \frac{2\Pi}{k} \quad \text{(a)}$$

(A25a-b)

where $\quad Re_\delta = Re_\theta \dfrac{\delta}{\delta^*}\dfrac{\delta^*}{\theta} \qquad$ (b)

using equation (A23) δ can be eliminated from the above equation, and an expression for λ such that $\lambda=\lambda(Re_\theta, \Pi)$ can be derived.

In conclusion two functional equations can be obtained:

$H_{12}=H_{12}(\lambda,\Pi)$ and $\lambda=\lambda(Re_\theta, \Pi)$

explicating Re_θ from the second of above equations:

$$Re_\theta = \frac{1+\Pi}{\kappa H}\exp(\kappa\lambda - \kappa B - 2\Pi)$$ It is possible to obtain: $\qquad$ (A26)

$$\lambda = a(\Pi)\frac{H_{12}}{H_{12}-1} \qquad (a)$$

$$a(\Pi) = \frac{2+3.179\,\Pi+1.5\Pi^2}{\kappa(1+\Pi)} \qquad (b) \qquad\qquad\qquad \text{(A27a-b-c)}$$

$$Re_\theta = \frac{1+\Pi}{\kappa H_{12}}\exp(\kappa\lambda - \kappa B - 2\Pi) \qquad (c)$$

From the parametric studies of the above equations Coles obtained an empirical correlation between skin friction, Reynolds number (based on momentum thickness) and shape parameter H_{12} following reported:

$$Cf \cong \frac{0.3e^{-1.33H_{12}}}{\left(\log Re_\theta\right)^{1.74+0.31H_{12}}} \qquad \text{Coles formula} \qquad\qquad \text{(A28)}$$
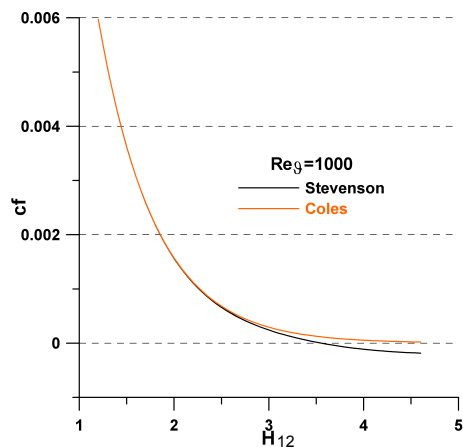
this formula well capture the skin friction behaviour for values of H_{12} and θ not too high, and has been corrected by Coles to take into account also negative values of skin friction (for the separated flow integration), as well described in [32]. This relation is the most used formula for the skin friction prediction in the numerical code based on viscous-inviscid interaction.

Figure A3: Skin friction variation with shape parameter H_{12} (from Drela)

▪ <u>Turbulent boundary layer with transpiration</u>

The skin friction formula obtained above (A28) has been obtained with the assumption of absence of transpiration to the wall. If this assumption is removed the von-Karman integral equation from which all the computation has been deducted, changes as follow (passages are omitted):

$$\frac{d\theta}{dx} = \frac{1}{2}Cf - (2 + H_{12})\frac{\theta}{u_e}\frac{du_e}{dx} + \frac{V_0}{U_e} \quad \text{von Karman equation with transpiration} \quad (A29)$$

where the additional term V_0 is the wall transpiration. Another consideration is that as suggested by Stevenson [22] and Sucec [23], when transpiration is present, the overlap log-law should be modified as illustrated in (A30)

$$u_t^+ \cong \frac{1}{\kappa}\ln y^+ + B + \frac{V_0^+}{4}\left[\frac{1}{\kappa}\ln y^+ + B\right]^2 + 2\left[\frac{\Pi + V_0^+\overline{\Pi}}{\kappa}\right]\sin^2(\frac{\pi}{2}\frac{y^+}{\delta^+}) \qquad (A30)$$

where $V_0^+ = \frac{V_0}{u^*}, \overline{\Pi} = -1.95\ln(\left|\frac{V_0}{U_e}\right|) - 3.1$ and the subscript "t" for u is for *transpiration*

without repeating all the process that has guided to obtain the equation (A28) is possible to arrive to a similar formulation of the problem with the following assumption:

$$f = \frac{V_s}{U_e} = \frac{v_s}{u_\infty}\frac{u_\infty}{u_e} :$$

$$V_0^+ = \frac{v_0}{u^*} = \frac{v_0}{u_\infty}\frac{u_\infty}{u_e}\frac{u_e}{u^*} = f\,\lambda \quad ; \quad \overline{\Pi} = -1.95\ln(\left|f\right|) - 3.1 \quad ; \quad B = \begin{cases} 5 - 512 * f \text{ (if f > 0)} \\ 5 + 1375 * v_0^{+2} \text{ (if f < 0)} \end{cases}$$

$$\Gamma = \Pi + V_0^+ * \overline{\Pi}$$

$$a = \frac{V_0^+}{4\kappa^2}$$

$$\overline{b} = \frac{1}{\kappa} + \frac{V_0^+ B}{2\kappa} \qquad \Longrightarrow \qquad u^+ = a\,\ln^2 y^+ + \overline{b}\,\ln y^+ + c + d\,f_w(\frac{y}{\delta}) \qquad (A31)$$

$$c = B + \frac{V_0^+ B^2}{4}$$

$$d = \frac{\Gamma}{\kappa}$$

notes that equation (A31) gives back (A15) if transpiration is null.

In general:

$$u_e^+ = \lambda = a \ln^2 \delta^+ + \overline{b} \ln \delta^+ + c + 2d$$

$$\text{where} \quad \delta^+ = \frac{Re_\theta H_{12}}{d + b - 2a} \tag{A32}$$

It is possible, even though the major complexity of the problem, to arrive to similar formulation for integral parameters as obtained in the previous section:

$$\frac{\delta^*}{\delta} = \frac{d + b - 2a}{\lambda} \tag{A33}$$

$$\frac{\theta}{\delta} = \frac{d + b - 2a}{\lambda} - \frac{7.3611ad^2 - 2b^2 - 3.179bd - 1.5d^2 - 24a^2}{\lambda^2} \tag{A34}$$

$$H_{12} = \frac{\lambda(d + b - 2a)}{\lambda(d + b - 2a) + 7.3611ad^2 - 2b^2 - 3.179bd - 1.5d^2 - 24a^2} \tag{A35}$$

The main difference with the previous case is that for this set of equations is not possible to extrapolate one parameter as dependent of the others two, because the variables are inextricably related each others. In this case, it is more difficult to find a suitable curve-fit approximation, but iteration is necessary to compute the boundary layer parameters as the streamwise integration proceeds downstream.

In summary the two sets of equations are:

"classic" set of equations with Coles velocity profile:

$$u^+ = \frac{1}{\kappa}\ln(y^+) + B + \frac{\Pi}{\kappa}f_w\left(\frac{y}{\delta}\right)$$

$$\frac{d\theta}{dx} = \frac{1}{2}Cf - (2 + H_{12})\frac{\theta}{u_e}\frac{du_e}{dx} + \frac{V_0}{u_e} \qquad \textbf{\textit{momentum}}$$

$$cf \cong \frac{0.3e^{-1.33H_{12}}}{(\log Re_\theta)^{1.74 + 0.31H_{12}}} \qquad \textbf{\textit{skin friction}}$$

$$a(\Pi) = \frac{2 + 3.179\,\Pi + 1.5\Pi^2}{\kappa(1 + \Pi)}; \lambda = u_e^+ = \sqrt{\frac{2}{cf}}; \Pi = 0.8(\beta + .5)^{.75}, \beta = -\lambda^2 H_{12}\frac{\theta}{u_e}\frac{du_e}{dx}$$

$$H_{12} = \frac{\lambda}{\lambda - a(\Pi)}$$ *shape factor*

set of equations with Stevenson velocity profile:

$$u^+ = a \ln^2(y^+) + \overline{b} \ln(y^+) + c + d \, f_w(\frac{y}{\delta})$$

$$\frac{d\theta}{dx} = \frac{1}{2} Cf - (2 + H_{12}) \frac{\theta}{u_e} \frac{du_e}{dx} + \frac{V_0}{u_e}$$ *momentum*

$$\lambda = \sqrt{\frac{2}{cf}} \quad \text{and } \Pi = 0.8(\beta + .5)^{.75}, \beta = \frac{\delta^*}{\tau_w} \frac{dp}{dx} = -\lambda^2 H_{12} \frac{\theta}{u_e} \frac{du_e}{dx}$$

$$f = \frac{v_0}{u_e} \quad ; \quad V_0^+ = \frac{v_0}{u^*} = \frac{v_0}{u_e} \frac{u_e}{u^*} = f \lambda$$

$$\overline{\Pi} = -1.95 \ln(|f|) - 3.1 \quad ; \quad B = \begin{cases} 5 - 512\, f \ (\text{if } f > 0) \\ 5 + 1375\, v_0^{+2} \ (\text{if } f < 0) \end{cases} \quad ; \quad \Gamma = \Pi + V_0^+ \overline{\Pi}$$

$$a = \frac{V_0^+}{4\kappa^2} \quad ; \overline{b} = \frac{1}{\kappa} + \frac{V_0^+ B}{2} \quad ; c = B + \frac{V_0^+ B^2}{4} \quad ; d = \frac{\Gamma}{\kappa}$$

$$H_{12} = H_{12}(\lambda, f)$$

$$\lambda = \lambda \, (Re_\theta, H_{12}, f)$$
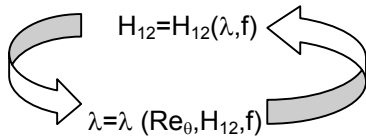
This process has to be iterated as the integration of the viscous solution proceeds downstrem.

Bibliography

[1] Eppler R., "Airfoils with boundary layer suction, design and off-design cases". Aerosp. Sci. Technol. 3 (1999) 403–415

[2] Seifert A. and Wygnanski I., , "On delay of airfoil stall by periodic excitation". Journal of aircraft, 33, No.4, 691 (1996)

[3] Seifert, A., Bachar, T., Koss, D., Shepshelovich, M., and Wygnanski, I., 1993, "Oscillatory Blowing: A Tool to Delay Boundary-Layer Separation," AIAA J., 31, No. 11,
pp. 2052-2060.

[4] Tinapp F., Nitsche W., "Separation control on high lift configuration by periodic excitation", 12DGLR-Fach-Symposium der AG STAB, November 2000

[5] Kim B. H., Williams D. R., "Large amplitude pneumatic oscillator for pulsed-blowing actuators", AIAA-2002-2704

[6] Gad-el-Hak, M., 1998, "Introduction to Flow Control". In Flow Control: Fundamentals and Practices (ed. Gad-el-Hak, M., Pollard, A., Bonnet, J. P.), pp. 1-107, Springer Lecture Notes in Physics, New Series Monographs, M53, Springer-Verlag, Berlin.

[7] Wu, J. Z., Lu, X. Y., Denny, A. G., Fan, M., Wu, J. M., 1998, "Post-stall flow control on an airfoil by local unsteady forcing", Journal of Fluid Mechanics 371, pp. 21-58.

[8] Wu, J. Z., Vakili, A. D., Wu, J. M., 1991, "Review of the Physics of Enhancing Vortex Lift by Unsteady Excitation", Prog. Aerospace Sci., Vol. 28, pp. 73-131.

[9] Miranda, S. "Active Control of Separated Flow over a Circular-Arc Airfoil", Virginia Polytechnic Institute, 2000

[10] Seifert A. and Pack L. G. "Separation Control at Flight Reynolds Numbers "Lessons Learned and Future Directions," AIAA Paper 2000-2542, 2000.

[11] Greenblatt D. and Wygnanski, I. "Parameters Affecting Dynamic Stall Control by Oscillatory Excitation," AIAA Paper 99-3121, 1999.

[12] Greenblatt, D. and Wygnanski, I., "Effect of leading-edge curvature on airfoil separation control," Journal of Aircraft, vol. 40, no. 3, pp. 473-481, May-June 2003.

[13] Rajat Mittal*, Rupesh B. Kotapati and Louis Cattafesta, "Numerical Study of Resonant Interactions and Flow Control in a Canonical Separated Flow", 43rd AIAA Aerospace Sciences Meeting and Exhibit, January 10-13, Reno, Nevada.

[14] McCullough, G. B. and Gault, D. E., "Examples of Three Representative Types of Airfoil-Section Stall at Low Speed" NACA TN 2502, 1951.

[15] Roshko, A. "On the Development of Turbulent Wakes from Vortex Streets," NACA Report 1191, 1954.

[16] Ho, C.-M. & Huerre, P. 1984 "Perturbed free shear layers". Ann. Rev. Fluid Mech. 16, 365-424.

[17] Ho, C.-M. & Nosseir, N. S. 1981 "Dynamics of an impinging jet. Part I. The feedback phenomenon". J. Fluid Mech. 105, 119-142.

[18] Coiro D.P., Dini P., " Stall and Post Stall Performance Prediction of Advanced Wind Turbine Airfoils ", XII AIDAA National Congress, Como, Italy, July 1993

[19] Coiro D. P., Dini P.,"Prediction of aerodynamic stall over wind-turbine airfoils", FTEC 97 July 21-24, Yogyakarta, Indonesia

[20] D. Coles, "A survey of data for turbulent boundary layers with mass transfer", P-4697, rand corporation report (1971)

[21] White F., "Viscous fluid flow", McGraw-Hill, 1974

[22] Stevenson T.N, "Turbulent boundary layers with transpiration", AIAA J. 2, 1500 (1964)

[23] Sucec J, Oljaca M.,"Calculation of turbulent boundary layers with transpiration and pressure gradient effect", Int. J of Heat and mass transfer vol 38 N° 15 pg. 2855-62, 1995

[24] Andersen, P. S., Kays, W. M., and Moffat, R. J.; "The turbulent boundary on a porouse plate: an experimental study of fluid mechanics for adverse free stream pressure gradient" Thermoscience Division, Department of Mechanical Engineering, Stanford University. report # HMT-15, 1972

[25] Schatz M., Thiele F., " Numerical Study of High Lift Flow with Separation Cobtrol by Periodic Excitation" , 39th AIAA Aerospace Sciences Meeting & Exhibit 8-11 January 2001 – Reno, NV

[26] Ekaterinaris, J.A.,"Prediction of active flow control performance on airfoils and wings" Aerospace Science and Technology 8 (2004) 401–410

[27] Liu Y., Sankar L. N. "Computational Evaluation of the Steady and Pulsed Jet Effects on the Performance of a Circulation Control Wing Section" Georgia Institute of Technology, Atlanta, GA 30332-0150

[28] Rung T., Thiele F., " Computational Modeling of Complex Boundary Layer Flow" , 9th Int. Symp. On Transport Phenomena in Thermal-Fluid Engineering, Singapore, 1996

[29] McCormick, D.C., "Boundary Layer Separation Control with Directed Synthetic Jets," AIAA Paper 2000-0519, Jan. 2000.

[30] Karam, J.T., and Franke, M.E., "The Frequency Response of Pneumatic Lines," J. Basic Engineering, Trans. ASME, pp. 371-378, 1967.

[31] Pope,S.B., "Turbulent Flows", Cambridge University Press, 2000

[32] Drela,M., "Two dimensional transonic aerodynamic design and analysis using the Euler equations", Thesis, GTL report n° 187, M.I.T. libraries, 1986